UNIVERSITÀ
DEGLI STUDI
DI TRIESTE

Dipartimento di Fisica

CORSO DI LAUREA MAGISTRALE
INTERATENEO IN FISICA

Curriculum Fisica della Materia

TESI DI LAUREA MAGISTRALE

Growth and characterization of YBCO heterostructures

Sintesi e caratterizzazione di eterostrutture con YBCO

Laureanda:
Costanza Lincetto

Relatore:
Prof. Daniele Fausti

Correlatori:
Dr.ssa Angela Montanaro
Dr. Sandeep Kumar Chaluvadi

ANNO ACCADEMICO 2024-2025

Trovare la via è facile se hai una corda sopra la testa:
se ce l'hai sotto i piedi, allora è un'altra cosa.

Le otto montagne
Paolo Cognetti

Contents

Riassunto **6**

Introduction **10**

1 Cavity electrodynamic **15**
1.1 Fabry-Pérot cavity . . . 16
1.2 Light-matter hybridization . . . 19
1.2.1 Weak coupling . . . 19
1.2.2 Strong coupling . . . 19
1.2.3 Real systems: role of the dissipation . . . 22
1.2.4 Strong coupling with vacuum fields . . . 23
1.3 Superconductors in cavity . . . 24
1.3.1 Theory proposals . . . 24
1.3.2 Experimental results . . . 26

2 Design of the heterostructures **29**
2.1 Optical properties of YBCO . . . 29
2.1.1 Charge-transfer hybridization . . . 31
2.2 Simulation of heterostructures . . . 32
2.2.1 Transfer matrix method . . . 32
2.2.2 Numerical simulations . . . 36
2.2.3 List of Samples . . . 38

3 Synthesis of the heterostructures **41**
3.1 Pulsed Laser Deposition technique . . . 41
3.1.1 Overview . . . 41
3.1.2 Stages of Pulsed Laser Deposition . . . 43
3.1.3 Experimental setup . . . 46
3.2 Growth of the samples . . . 46
3.2.1 Deposition of single layers . . . 46
3.2.2 Deposition of multilayers . . . 52
3.3 Deposition of silver layer on top . . . 54

4 Microwave absorption measurements **57**
4.1 Experimental setup . . . 57
4.2 Magnetic field dependence measurements . . . 59
4.2.1 Superconducting signals . . . 60
4.3 Determination of critical temperature by low field measurements . . . 62

4.3.1 Open cavity 64
4.3.2 Asymmetric closed cavity 66
4.3.3 Symmetric closed cavity 68

5 Reproducibility analysis **71**
5.1 Samples degradation 72
5.1.1 Silver-YBCO interface 72
5.1.2 CeO_2-YBCO interface 74
5.2 Transport measurement in a partially silver-capped heterostructure 75

6 Optical measurements **79**
6.1 Three-pulse spectroscopy 79
6.1.1 Experimental setup 80
6.2 Measurements 82
6.3 Temperature scan 85
6.3.1 Sample Y60C5 85
6.3.2 Sample C25Y60C25 88

Conclusions **91**

A Electron Paramagnetic Resonance Spectroscopy **93**
A.1 Paramagnetic signals 94

B Dielectric function models **97**
B.1 Drude-Lorentz model 97
B.2 Tauc-Lorentz model 97

Bibliography **99**

Acknowledgements **103**

Riassunto

Lo studio dei materiali quantistici attraverso intensi impulsi laser é una delle direzioni più promettenti nell'ambito della fisica della materia condensata contemporanea. Tali impulsi possono portare un materiale fuori dall'equilibrio, inducendo stati transienti che mostrano nuove proprietà non accessibili all'equilibrio.

Un ulteriore approccio si é sviluppato in parallelo negli ultimi anni, ispirato dai progressi della *cavity quantum electrodynamics* (QED). Tale approccio sfrutta la modifica delle proprietà all'equilibrio di un materiale ponendolo all'interno di una cavità ottica, senza l'obbligo di introdurre campi esterni.

La principale motivazione di questo lavoro é studiare se sia possibile controllare il comportamento superconduttivo del $YBa_2Cu_3O_{7-\delta}$ (YBCO) ponendolo in cavità. Il YBCO é un superconduttore ad alta temperatura critica, facente parte della famiglia dei cuprati. In tale classe di materiali, il meccanismo dietro all'accoppiamento elettronico é tuttora una questione aperta. Ciò che sembra chiaro però, é che nei cuprati transizioni elettroniche ad alta energia abbiano un ruolo fondamentale nell'instaurarsi dell'ordine superconduttivo. Di particolare importanza in questo contesto c'è l'eccitazione *charge-transfer* (CT), tra gli orbitali O $2p$ e Cu $3d$ all'interno dei piani rame-ossigeno caratteristici dei cuprati. Tale transizione ha energia di circa 2eV, e si ipotizza che contribuisca al meccanismo di *pairing*.

L'obiettivo quindi é realizzare delle strutture multistrato formate da un layer di YBCO, inserito tra due strati di dielettrico (CeO_2), a loro volta racchiusi tra due strati metallici (o argento o $LaNiO_3$) che fungono da specchio.

Per progettare tali strutture, sono stati considerati diversi parametri per ottimizzare la geometria della cavità, tra cui riflettività degli specchi e spessori dei diversi strati, in modo tale da controllare la risonanza della cavità e l'*oscillator strength* della transizione CT. Oltre alla geometria della cavità, particolare attenzione è stata dedicata al ruolo delle interfacce tra i diversi materiali. In particolare, sono state studiate eterostrutture contenenti interfacce argento-YBCO e CeO_2-YBCO, al fine di valutare come gli effetti di prossimità possano influenzare il comportamento superconduttivo del YBCO.

In questa tesi sono stati affrontati tutti i passaggi necessari allo studio del tema: progettazione, simulazione, sintesi e caratterizzazione, che sono organizzati all'interno del lavoro nel seguente modo.

- **Capitolo 1**: vengono introdotti gli aspetti teorici per comprendere la *cavity electrodynamics*, con particolare attenzione al regime di accoppiamento forte. Vengono poi discussi studi teorici e sperimentali su superconduttori inseriti in cavità.

- **Capitolo 2**: viene descritta la progettazione delle eterostrutture a base di YBCO tramite simulazioni *transfer matrix*, utilizzate per calcolare la risposta ottica di strut-

ture *multilayer* e ottimizzare la geometria della cavità per le scale energetiche di interesse.

- **Capitolo 3**: é illustrata la sintesi dei campioni tramite *Pulsed Laser Deposition* (PLD), una tecnica che consente la crescita di film epitassiali con elevata qualità. I campioni ottenuti compongono una struttura stratificata, in cui il film di YBCO è inserito tra strati isolanti di CeO_2 e chiuso da due strati metallici che fungono da specchi della cavità: il primo è $LaNiO_3$ (LNO), il secondo è uno strato d'argento cresciuto mediante *e-beam evaporation*.

- **Capitolo 4**: viene presentata la caratterizzazione mediante assorbimento a microonde (MWA), tecnica che permette di misurare indirettamente la penetrazione del campo magnetico e di rilevare l'intervallo di temperature che individua la transizione superconduttiva, nonché di osservare come questa venga modificata dalla cavità in condizioni di equilibrio.

- **Capitolo 5**: vengono affrontate le problematiche legate alla riproducibilità delle misure e alla degradazione dei campioni nel tempo, con particolare attenzione al ruolo che le interfacce Ag-YBCO e CeO_2-YBCO assumono nel determinare la stabilità delle proprietà superconduttive.

- **Capitolo 6**: sono descritte le misure ottiche, includendo una descrizione dettagliata dell'apparato sperimentale utilizzato per la spettroscopia risolta in tempo. In particolare, viene introdotta la spettroscopia a tre impulsi come efficace tecnica per investigare le dinamiche ultraveloci del condensato superconduttivo e la sua natura non lineare.

La tecnica *Pulsed Laser Deposition* (PLD) ha permesso di realizzare eterostrutture risonanti con la transizione *charge-transfer* (CT) del YBCO. Variando lo spessore di YBCO, CeO_2 e dello strato superiore d'argento, sono state ottenute diverse geometrie di cavità. Quest'ultimo spessore ha determinato il *quality factor* della cavità, ma anche influenzato fortemente il comportamento superconduttivo.

Le misure di trasporto hanno evidenziato superconduttività solo nei campioni che non comprendevano strati ulteriori al sopra del film di YBCO, mentre l'assorbimento a microonde (MWA) ha confermato che anche tali campioni sono superconduttivi, seppur con temperature critiche ridotte e transizioni più ampie in temperatura. La qualità delle interfacce (Ag–YBCO e CeO_2–YBCO) si è dimostrata cruciale per la riproducibilità e il controllo della fase superconduttiva.

Le misure ottiche risolte in tempo hanno mostrato modifiche del segnale non lineare in funzione della temperatura, con un aumento della risposta nei campioni in cui il YBCO era chiuso da uno strato di argento, la cui origine però resta da chiarire (se essa sia legata alla superconduttività o alla fase di pseudogap). É stato possibile tracciare tale transizione solo in una ristretta finestra energetica centrata a 1.3 eV, attribuita ipoteticamente alla ridistribuzione del peso spettrale ad energie inferiori a 1.8 eV, come conseguenza del livello di drogaggio del YBCO.

I risultati suggeriscono diverse direzioni per future ricerche. La degradazione e la soppressione della superconduttività sono con tutta probabilità legate alla deposizione di strati

amorfi, alla scarsa qualità delle interfacce o anche all'ossidazione dell'argento. Il lavoro futuro dovrebbe quindi concentrarsi sull'ottimizzazione della crescita degli strati di copertura, al fine di preservare la stechiometria del YBCO e migliorare la qualità strutturale delle interfacce. Un altro problema aperto riguarda la stabilità dello strato d'argento, soggetto a ossidazione: materiali alternativi, come l'oro, potrebbero essere esplorati per garantire una migliore stabilità.

Saranno inoltre necessari ulteriori studi per distinguere gli effetti intrinseci indotti dalla cavità da quelli estrinseci dovuti a processi di degradazione, così da stabilire se la cavità possa realmente modificare lo stato superconduttivo del YBCO.

Infine, indagini ottiche più estese, sia in condizioni di equilibrio sia fuori equilibrio, con variazione delle energie di sonda e con drogaggio controllato, potrebbero chiarire l'origine della stretta finestra energetica centrata a 1.3eV che permette di tracciare la transizione superconduttiva.

Introduction

The exploration of quantum materials via non-thermal pathways has emerged as one of the most promising directions in contemporary condensed matter physics, owing to the unique possibility of manipulating their intrinsic properties beyond the limits imposed by equilibrium conditions. The electromagnetic field has therefore joined the family of external parameters - alongside more conventional ones such as temperature, pressure, and chemical doping - that can be employed to tailor the physical properties of a system.

In particular, intense ultrafast laser pulses can be used to drive the material out of equilibrium, inducing transient states that may display novel electronic or magnetic properties, that are not accessible at the equilibrium. Such approaches have already demonstrated the potential to reveal hidden phases of matter, alter collective excitations, and manipulate ordering phenomena on ultrafast timescales [1, 2].

In parallel with these developments, an alternative strategy has recently gained significant attention, inspired by advances in cavity quantum electrodynamics (QED) [3]. Unlike ultrafast pump-probe schemes that rely on strong external driving fields, this approach exploits the modification of the electromagnetic environment itself to directly influence the equilibrium properties of a material. By embedding a system inside an optical cavity, the electromagnetic field is confined within a finite volume, allowing only specific photon modes to live within the cavity and thereby reshaping the spectrum of light–matter interactions

The confinement of light within the cavity can dramatically enhance the coupling between photons and electronic or vibrational degrees of freedom of the material. In regimes of strong coupling, this interaction can give rise to hybrid light–matter quasiparticles, often referred to as polaritons. Remarkably, such hybridization can occur even in the absence of an external driving field, potentially allowing to control the equilibrium properties of quantum materials through the coupling with vacuum fluctuations of the confined electromagnetic modes [6]. This new approach offers a complementary route to the conventional paradigm of non-equilibrium ultrafast control.

Within the broad class of quantum materials, high-temperature superconductors (HTS) are interesting candidates for cavity engineering. In contrast to conventional Bardeen-Cooper-Schrieffer (BCS) superconductors, where the electron pairing is well understood to be phonon-mediated, the microscopic mechanism beyond the onset of superconductivity in high-T_c superconductors is still an open and actively debated question.

In this thesis, the focus will be placed on $YBa_2Cu_3O_{7-\delta}$ (YBCO), an extensively studied unconventional high-T_c superconductor that belongs to the class of cuprates. In these materials high-energy electronic transitions play a pivotal role in the onset of the superconducting phase. While in conventional BCS materials the opening of the superconducting gap is associated with a redistribution of the spectral weight only in the nearby of the gap energy, in cuprates this redistribution extends to energies up to two orders of magnitude

of the gap energy.

Of particular importance in this context is the charge-transfer (CT) excitation between the O $2p$ orbitals and the Cu $3d$ orbitals within the Cu–O plaquettes [21]. This high-energy electronic transition - which lies around 2 eV - has been suggested as a possible contributor to the unconventional pairing mechanism in cuprates. Therefore, understanding its role could provide valuable insights into the complex interplay of electronic correlations, lattice dynamics, and superconductivity in YBCO and related materials.

The central motivation of this thesis lies in investigating if it is possible to control the superconducting behaviour of YBCO through the engineering of a heterostructure that is resonant with the CT transition. To this purpose, a variety of cavity parameters are systematically considered. These include the reflectivity and thickness of the mirrors - which determine the quality factor of the cavity - as well as the thickness of both the dielectric spacer CeO2 and the YBCO layer itself, controlling respectively the cavity resonance and the oscillator strength of the CT transition.

In addition to cavity geometry, particular attention is devoted to the role of interfacial properties. Specifically, heterostructures incorporating silver-YBCO and CeO_2-YBCO interfaces are investigated in order to assess how proximity effects may influence the superconducting behaviour of YBCO. By addressing both cavity design parameters and interfacial characteristics, this work aims to establish whether cavity engineering can provide a viable pathway for tuning superconductivity in cuprates.

In this thesis, all the steps required to study this topic are undertaken, from design and simulation, to synthesis and characterization.

The initial stage employs transfer matrix simulation to calculate the optical response of a multilayer structure and find the optimal cavity geometry to tune the heterostructures at the desired energy scale.

Following the design stage, the synthesis of the samples is carried out using Pulsed Laser Deposition (PLD), a versatile technique that permits to grow high-quality epitaxial thin films of complex oxides [33]. The thickness of the different layers is controlled by tuning the deposition conditions. The obtained samples consist of a layered structure in which the YBCO film is embedded with insulating CeO_2 layers, and closed with two metallic layers that act as mirrors for the cavity, the first one is $LaNiO_3$ (LNO), deposited directly onto the substrate, the second one is a silver layer grown with e-beam evaporation, differently to the PLD-grown layers.

The final stage of the study consists of a comprehensive characterization of the sample. Firstly, for the uncapped sample (prior to the deposition of the silver top layer) transport measurements were performed, in order to have a proof of the superconducting behaviour of the YBCO layer grown. Subsequently, for all fabricated samples, through microwave absorption (MWA) the penetration of the magnetic field was indirectly measured [39], allowing to detect the superconducting transition range and how it is modified by the cavity environment at the equilibrium. Finally, time-resolved optical spectroscopy was employed to investigate how the dynamics of electronic excitations are affected by the cavity confinement.

As a complementary analysis, the reproducibility and stability of the samples were examined, with particular attention to the time-dependent degradation of their superconducting properties and the distinct roles played by the Ag-YBCO and CeO_2-YBCO interfaces in this process.

The thesis is structured as follows:

- **Chapter 1** introduces the theoretical background of cavity electrodynamics, focusing on the strong coupling regime. Selected theoretical and experimental studies of superconductors placed in cavity are discussed to contextualize the present work.
- **Chapter 2** outlines the design of YBCO-based heterostructures using transfer matrix simulation. The results of these simulations are used to optimize the cavity geometry at the relevant energy scales.
- **Chapter 3** describes the synthesis process by Pulsed Laser Deposition (PLD). The growth technique and experimental setup are introduced in detail, and preliminary characterizations - including transport measurements - are presented to verify the superconducting properties of the fabricated films.
- **Chapter 4** presents the MWA characterization and describes how this technique can be a useful tool to study the superconducting transition in both open and closed cavities.
- **Chapter 5** addresses issues of reproducibility and sample degradation, with a particular focus on the role of critical interfaces such as Ag-YBCO and CeO_2-YBCO.
- **Chapter 6** presents the optical measurements, including a detailed description of the time-resolved spectroscopy setup. In particular, three-pulse spectroscopy is introduced as a powerful technique to investigate the ultrafast dynamics of the superconducting condensate and its non-linear nature.

Chapter 1

Cavity electrodynamic

Quantum materials are complex many-body systems consisting of multiple atomic species. Their low energy physics typically features a complex interplay of charge, spin, orbital and lattice degrees of freedom, that can give rise to intricate phase diagrams and correlated ground states that can be controlled by external parameters, such as pressure, strain, doping, or electromagnetic fields.

A powerful route to control these materials is through nonthermal pathways with ultrashort and intense laser pulses. In this case, the large number of photons created by the laser occupy a macroscopic coherent state that can alter the material's properties. The laser excitation reshapes the energy landscape, modifies coupling constants, or selectively drives lattice vibrations, giving rise to transient superconductivity or light-induced ferroelectricity. Pioneering work by Cavalleri and collaborators has established this field, demonstrating for example nonlinear phononic control of the lattice [1] or light-enhanced superconductivity in cuprates [2].

A different strategy toward modifying the properties of quantum materials is to replace intense laser light with quantum-mechanical photon modes in an optical cavity. By engineering a suitable surrounding environment, i.e. a cavity, it is possible to reduce the effective optical mode volume, thus enhancing the electromagnetic field amplitude associated with a single photon. In turn, the light–matter coupling is increased with respect to its bare value. Importantly, in the strong-coupling regime, the number of photons required to modify the properties of light-matter systems can be drastically reduced, to the point where pure quantum oscillations, thus without injected photons (dark cavity), are sufficient to achieve the desired effects [3].

The first demonstrations of this concept were carried out in molecular systems, evidenced by large Rabi splitting [4, 5].

More recently, a new frontier has emerged: embedding solid-state quantum materials within cavities to manipulate their macroscopic properties [6]. It has been shown, for example, that cavity confinement can enhance ferroelectric instabilities in quantum paraelectrics [7], or modify collective excitations relevant to superconductivity. This establishes the field of *cavity quantum materials*, where equilibrium properties are engineered through photon modes rather than through external laser driving.

In this chapter, we will first discuss the fundamental physics of cavity quantum electrodynamics, beginning with the simplest example: the Fabry-Pérot cavity. We will then examine the regimes of weak and strong coupling. Finally, we will explore how superconductivity can be modified and controlled through cavity engineering.

1.1 Fabry-Pérot cavity

The simplest model is the Fabry-Pérot cavity, which consists of two parallel mirrors with reflectivity $R_m < 1$, placed at a distance L (figure 1.1b). Let us consider a single-mode optical field with wavelength λ entering the cavity through the left mirror. As it propagates inside the cavity, each time it reaches a mirror, one part of the field is transmitted outside, while another part is confined inside, undergoing multiple reflections. At each reflection, the field acquires a phase ϕ_C, which is determined by the cavity length L and the refractive index n within the cavity. An additional phase shift due to the mirrors ϕ_M must be added, leading to a total phase of

$$\phi = 2\phi_M + 2\phi_C = 2\pi + 2\frac{2\pi n L}{\lambda}, \tag{1.1}$$

corresponding to the phase accumulated during a round trip. We set $\phi_M = \pi$, that is the case of a broadband dielectric mirrors at the designed wavelength [8]. At each round trip the light that remains into the cavity acquires a phase ϕ and interferes with itself: when the phase shift is an integer multiple of 2π there is constructive interference and the optical mode is allowed within the cavity. Therefore it is possible to tune the cavity length L in order to support a specific wavelength:

$$L = m\frac{\lambda}{2n} \qquad m \in \mathbb{N}. \tag{1.2}$$

Considering all the contributions of transmissions and interference effects, we can write the total cavity transmission as a function of the phase shift ϕ and the mirror reflectivity R_m:

$$T(\phi) = \frac{1}{1 + 4\frac{R_m}{(1-R_m)^2}\sin^2(\phi/2)}. \tag{1.3}$$

The transmission is maximum at frequencies $\omega_m = \frac{2\pi c n}{\lambda_m}$ that correspond to a total phase accumulation of $\phi = 2\pi m$, as shown in figure 1.1a. These frequencies are the ones of the modes allowed by the boundary conditions of the cavity. The spacing between two adjacent cavity modes ω_m is the Free Spectral Range (FSR), it depends on the thickness of the cavity and therefore is tunable with the distance between the mirrors.

The electric field amplitude of the cavity is enhanced by the constructive interference of light within the cavity. If we place materials with dipole-allowed transitions at the antinodes of the optical modes, we can couple the material excitations more strongly with respect to the free space.

As mentioned above, the mirrors reflectivity is less than 1, therefore the intensity of the confined mode decays with time, as photons can escape the cavity each time they impinge into the mirrors. This loss is quantified by the quality factor Q, a dimensionless parameter defined as the ratio of the energy stored in the cavity $I(t)$ to the energy dissipated per optical cycle:

$$Q = \omega_c \frac{I(t)}{-\frac{dI(t)}{dt}}, \tag{1.4}$$

where ω_c is the frequency of the cavity mode. From the latter equation, we can obtain the exponential dissipation of the electromagnetic energy stored inside the cavity:

$$I(t) = I_0 \exp^{-\gamma_c t}, \tag{1.5}$$

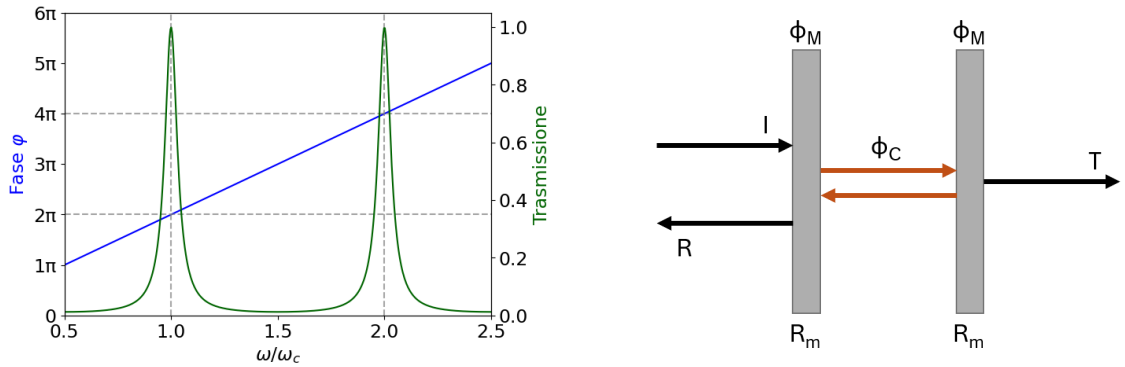

(a) (b)

Figure 1.1: **Transmission of a Fabry-Pérot cavity.** (a) A resonant mode appears when the round trip phase accumulation matches an integer multiple of 2π ($\phi = 2\pi m$, horizontal lines). (b) Schematic of a Fabry–Pérot cavity showing the phase accumulation during a round trip of light. ϕ_M indicates the mirror contribution, while ϕ_C is the phase acquired inside the cavity.

where I_0 is set to be the initial intensity and $\gamma_c = \frac{\omega_c}{Q}$ indicates the lifetime of the m-th cavity mode, that is also the linewidth of the cavity mode.

Considering that the relation between the electromagnetic energy and the amplitude of the electric field is $I(t) \propto |E(t)|^2$, the electromagnetic field can be written as:

$$E(t) = E_0 e^{-\frac{\gamma_c}{2}t} e^{-i\omega_c t}, \tag{1.6}$$

where E_0 is the initial amplitude of the field corresponding to I_0. Through the Fourier transform of the latter equation we can find an expression for the field and energy spectral distribution within the cavity:

$$I(\omega) \propto \frac{1}{(\omega - \omega_c)^2 + (\frac{\gamma_c}{2})^2}, \tag{1.7}$$

that is a Lorentzian distribution. It is characterized by the central wavelength ω_c, i.e. the cavity mode, and the Full Width Half Maximum (FWHM) γ_c.

From equation 1.5, we can write the energy dissipated:

$$\frac{dI(t)}{dt} = -\gamma_c I(t) \tag{1.8}$$

and rewrite the quality factor as:

$$Q = \omega_c \frac{I(t)}{\gamma_c I(t)} = \frac{\omega_c}{\gamma_c}, \tag{1.9}$$

showing that at a larger quality factor corresponds a smaller FWHM. This definition is the one commonly used to determine Q experimentally.

The quality factor can be also related to the design of the cavity through the mirrors reflectivity R_m and the mode order m. One round-trip consists in a light pulse moving from one mirror of the cavity to the other and back; when the light impinges on a mirror

has a probability of $1 - R_m$ to escape from the cavity, reducing the energy stored of a factor R_m. Therefore, the energy lost in one round trip can be expressed as:

$$\Delta I_{RT} = 2(1 - R_m)I_i, \tag{1.10}$$

corresponding to a time of flight:

$$\Delta t_{RT} = \frac{2L}{c} = \frac{mn\lambda}{c}. \tag{1.11}$$

The energy lost per oscillation can be written as the energy lost per round trip times the ratio of the oscillator period and the time of flight:

$$\Delta I_{cycle} = \Delta I_{RT} \frac{\Delta t_{cycle}}{\Delta t_{RT}} = \frac{2(1 - R_m)}{m} I_i. \tag{1.12}$$

Recalling equation 1.4, we can write the quality factor as a function of the mirror reflectivity and the cavity mode order m:

$$Q = \frac{m\pi}{2} \frac{1 + R_m}{1 - R_m}, \tag{1.13}$$

and therefore also the inverse photon lifetime γ_c can be rewritten:

$$\gamma_c = \frac{2\omega_m}{m\pi} \frac{1 - R_m}{1 + R_m}, \tag{1.14}$$

indicating that all the photons within the cavity have the same lifetime and the latter is fixed by the mirror quality and the cavity length.

In an ideal absorption-less cavity, the Q-factor value is controlled only by the mirror losses. As we can see in figure 1.2, a lower Q-value means a broader cavity mode, that is a consequence of the longer decay time of the cavity mode.

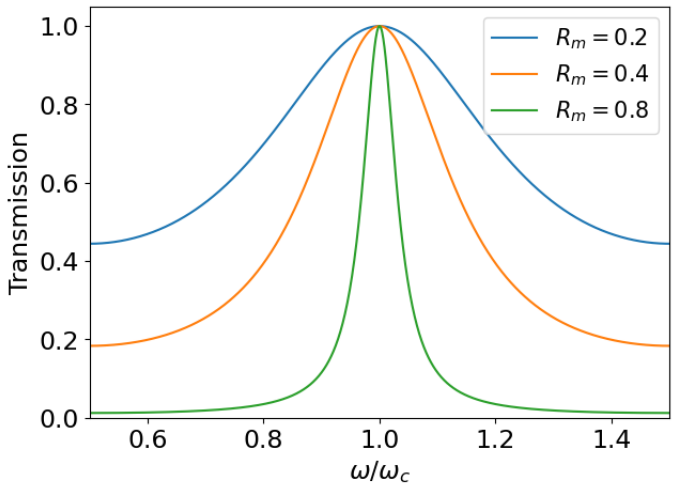

Figure 1.2: **Transmission for different values of the reflectivity R_m of the mirrors.** By increasing the reflectivity of the mirrors, the bandwidth of the transmission curve decreases.

1.2 Light-matter hybridization

Placing a material that has a dipole-allowed transition in a cavity and tuning the cavity so that the photon mode is resonant, allow us to create a coupled system: the photons trapped inside the cavity will be absorbed and re-emitted by the material continuously, inducing a coherent evolution of the trapped photons. There are two coupling regimes: *weak coupling*, in which neither the states nor the energies of the material in resonance with the cavity mode change compared to the vacuum case, only the photon emission lifetime of the material changes, and the *strong coupling*, in which both the energy and states are modified, giving rise to hybrids states that inherit features of both the constituent parts.

1.2.1 Weak coupling

Once a material has emitted a photon, there is a non-zero probability that it will be reabsorbed by the same material. This probability can be increased if the emitter is placed inside a cavity: in fact, the emitted photons remain trapped within the cavity volume due to the mirror reflections, thereby modifying the mode density of the photons within the cavity. In the weak coupling regime, however, losses dominate over the probability of reabsorption, therefore, compared to the vacuum case, only the photon emission time changes.

This control of spontaneous emission in cavities is described by the Purcell effect. If the system is in resonance, i.e. the frequency of the material transition ω_0 matches the frequency of the cavity mode ω_c, there is an enhancement of the spontaneous decay rate given by the Purcell factor[9, 10]:

$$F_P = \frac{3}{4\pi^2}\frac{\lambda_c^3}{n^3}\frac{Q}{V}, \tag{1.15}$$

where n is the refractive index inside the cavity, V is the volume of the cavity and Q is the quality factor already introduced.

By increasing the emission rate, the lifetime necessarily becomes shorter in cavity with respect to the free space. As we can see from the latter relation, the Purcell factor is bigger, i.e. the change on the spontaneous emission rate is bigger, if Q is higher and V is smaller, i.e. the lifetime of a photon inside the cavity is higher, as the confinement of the light.

1.2.2 Strong coupling

Differently from the weak coupling regime, in the strong coupling the rate of the probability of a photon to be reabsorbed from the material is comparable to the losses. In this regime the states and the energy values of the coupled system are different with respect to the ones of the uncoupled system.

To investigate the microscopic origin of coherent energy exchange between light and matter, we will use a quantum mechanical description of the coupled system. The material is modelled by an assembly of N two-level systems, while the cavity by a single quantized mode. Therefore the dimension of the Hilbert space is N+1. The Hamiltonian that describes the system can be written as the sum of three contribution:

$$H = H_0 + H_C + H_{int}, \tag{1.16}$$

that are respectively the hamiltonian of the two-level system, of the electromagnetic field and the one that describes the coupling.

Considering the simplest case in which there is only one dipole (N=1), the interaction potential with the cavity field is:

$$U = -\vec{\mu} \cdot \vec{E}, \tag{1.17}$$

where $\vec{\mu}$ is the dipole moment. From its quantization, the interaction Hamiltonian can be rewritten as:

$$H_{int} = g(\sigma + \sigma^\dagger)(a + a^\dagger), \tag{1.18}$$

where g is the coupling strength between the cavity and the dipole, $a(a^\dagger)$ is the annihilation (creation) operator for the cavity photons and $\sigma(\sigma^\dagger)$ is the lowering (raising) operator for the two-level system.

Returning now to N two-level systems, the latter equation can be generalized considering a sum over all the N systems, and the total hamiltonian 1.16 can be written as

$$H_D = \omega_c a^\dagger a + \omega_0 \sum_{i=1}^{N} \sigma_i^\dagger \sigma_i + g \sum_{i=1}^{N} (\sigma_i + \sigma_i^\dagger)(a + a^\dagger), \tag{1.19}$$

that is known as the Dicke Hamiltonian [11]. It describes the interaction between a set of N two-level system and a single-mode of the optical cavity.

In the Dicke Hamiltonian, the interaction term can be reduced using the Rotating Wave Approximation (RWA), in which the fast oscillating terms are neglected. Near the resonant regime, i.e. $\omega_0 \simeq \omega_c$, the terms corresponding to multiple excited states ($\sigma^\dagger a^\dagger$ and σa) beat at high frequencies, thus allowing us to neglect them if the coupling g is small compared to ω_c. Therefore, the Hamiltonian can be simplified as follows, known as the Tavis-Cummings model [12]:

$$H_{TC} = \omega_c a^\dagger a + \omega_0 \sum_{i=1}^{N} \sigma_i^\dagger \sigma_i + g \sum_{i=1}^{N} (\sigma_i a^\dagger + \sigma_i^\dagger a). \tag{1.20}$$

Considering that the Tavis-Cummings Hamiltonian conserves the total number of excitations[1], its eigenstates can be written as a linear superposition of states with the same total number of excitations. Therefore, if we consider only one excitation, the eigenstates must have the following form:

$$|\psi\rangle = \alpha \, |G, 1\rangle + \sum_{i=1}^{N} \beta_i \, |e_i, 0\rangle \,, \tag{1.21}$$

where $|G, 1\rangle$ denotes the state in which all the dipoles are in their ground state and there is only one photon in the cavity, and $|e_i, 0\rangle$ is the state in which the cavity is in the ground state and the i-th dipole is in its first excited state. Moreover, we will assume the coefficient β_i to be the same for all the excitations, implying that each dipole has the same probability of absorbing the photon. By diagonalizing the Hamiltonian, we obtain the eigenvalues of the light–matter system as a function of the cavity frequency ω_c and the cavity detuning

[1] This means that it commutes with the total number operator: $[n, H_{TC}] = 0$, where $n = a^\dagger a + \sum_{i=1}^{N} \sigma_i^\dagger \sigma_i$

$\Delta = \omega_c - \omega_0$:

$$\begin{aligned} \omega_{LP} &= \omega_c - \frac{\Delta}{2} - \sqrt{Ng^2 + \left(\frac{\Delta}{2}\right)^2} \\ \omega_{UP} &= \omega_c - \frac{\Delta}{2} + \sqrt{Ng^2 + \left(\frac{\Delta}{2}\right)^2}. \end{aligned} \tag{1.22}$$

They are split into an upper (UP) and lower polariton (LP) branch (as shown in figure 1.3), that have respectively an energy higher and lower with respect to the energy of the dipole transition in free space. Together with these two energy levels, there is also a set of N-1 dark states of material excitations at the energy ω_0, that are dipole-forbidden excitations, invisible to linear spectroscopy, as schematized in figure 1.4. The energy splitting between the two polariton branches is known as Rabi frequency, that in resonant condition is:

$$\Omega_R = \omega_{UP} - \omega_{LP} = 2\sqrt{N}g. \tag{1.23}$$

We underline that the Rabi frequency depends on the squared root of the number of oscillators $\sqrt{N}$. Therefore, for optically dense materials, such as solid-state materials, large splitting can be obtained by tuning their thickness within the cavity volume.

The eigenstates of the two polaritons are a linear superposition of the optical and the dipole excitations:

$$\begin{aligned} |LP\rangle &= X_0(\omega_c, \omega_0) \sum_{i=1}^{N} |e_i, 0\rangle + X_c(\omega_c, \omega_0) |G, 1\rangle , \\ |UP\rangle &= X_c(\omega_c, \omega_0) \sum_{i=1}^{N} |e_i, 0\rangle - X_0(\omega_c, \omega_0) |G, 1\rangle . \end{aligned} \tag{1.24}$$

While the $N-1$ dark states will have the following form:

$$|DS\rangle = \sum_{i=1}^{N} c_i |e_i, 0\rangle . \tag{1.25}$$

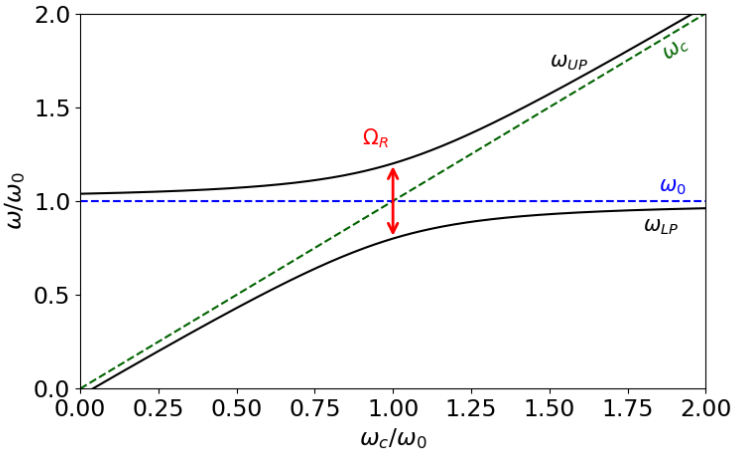

Figure 1.3: **Upper and lower polariton branches.** They are plotted as function of the cavity fundamental mode ω_c and the detuning of the cavity Δ.

The coefficients of the wave-functions can be expressed as a function of the cavity mode frequency ω_c as:

$$\begin{aligned} X_0(\omega_c,\omega_0) &= \frac{1}{\sqrt{1+\left(\frac{\omega_{LP}(\omega_c,\omega_0)-\omega_0}{g}\right)^2}}, \\ X_c(\omega_c,\omega_0) &= -\frac{1}{\sqrt{1+\left(\frac{g}{\omega_{LP}(\omega_c,\omega_0)-\omega_0}\right)^2}}. \end{aligned} \tag{1.26}$$

The coefficients $|X_0|^2$ and $|X_c|^2$ of the hybrid wave-functions represent the dipole and photon fractions of the polaritonic branches.

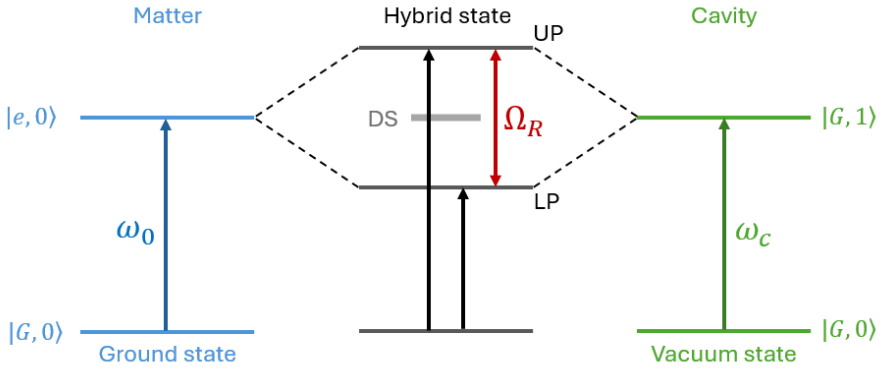

Figure 1.4: **Energy diagram of light-matter strong coupling.** Strongly coupled material and optical transitions, leading to the formation of the hybrid dipole-allowed polaritonic states UP and LP separated in energy by the Rabi splitting Ω_R, and the dipole-forbidden dark states (DS).

1.2.3 Real systems: role of the dissipation

Considering the relations for the polariton energies in equation 1.22, it seems that strong coupling regime is achievable for every value of the coupling strength $g\sqrt{N}$. This would be true only for an ideal system, by coupling an infinite crystal without incoherent scattering with an infinite coherent cavity mode. In real systems we have to take into account dissipation processes and the finite lifetime of the material and photonic excitations. We will now take into account also the decay times γ_m and γ_c, adding an imaginary term to the bare frequencies:

$$\begin{cases} \omega_0 & \rightarrow & \omega_0 - i\gamma_m \\ \omega_c & \rightarrow & \omega_c - i\gamma_c. \end{cases} \tag{1.27}$$

Therefore, the Tavis-Cummings Hamiltonian can be rewritten as:

$$H_{diss} = (\omega_c - i\gamma_c)a^\dagger a + (\omega_0 - i\gamma_m)\sum_{i=1}^{N}\sigma_i^\dagger\sigma_i + g\sum_{i=1}^{N}(\sigma_i a^\dagger + \sigma_i^\dagger a). \tag{1.28}$$

By diagonalizing this Hamiltonian, we can obtain a new relation for the Rabi splitting, that takes into account also of the decaying rates:

$$\tilde{\Omega}_R = \sqrt{4Ng^2 - (\gamma_c - \gamma_m)^2}\,. \tag{1.29}$$

This condition allows us to clearly distinguish between the weak and strong coupling regimes: strong coupling is reached only when $4Ng^2 > (\gamma_c - \gamma_m)^2$, that is, when $\tilde{\Omega}_R$ takes a real value. Conversely, for $4Ng^2 < (\gamma_c - \gamma_m)^2$, the system is in the weak coupling regime and no energy splitting occurs. Being in the weak coupling regime means that the loss rates dominate over coherent coupling ($g \ll \gamma_c, \gamma_m$) and the dynamics is incoherent, meaning that each emitter interacts independently with the cavity. If the coupling is comparable to the loss ($g \gtrsim \gamma_c, \gamma_m$), the strong coupling regime takes place and the emitters feel the presence of other emitters, forming the collective states that we called polaritons. When the coupling becomes stronger, comparable to the bare cavity frequency, the ultrastrong coupling regime is attained, in which also the ground state of the coupled light-matter is affected [3].

It can be shown that the emission of the coupled cavity field, considering also the dissipation, can be written as [13]:

$$I_{\text{cav}}(t) = \frac{4\sigma(0)^2 N g^2}{|\tilde{\Omega}_R|^2}\, e^{-(\gamma_c+\gamma_m)t} \sin\left(\frac{\tilde{\Omega}_R}{2}\, t\right) \sin\left(\frac{\tilde{\Omega}_R^*}{2}\, t\right). \tag{1.30}$$

Therefore, the dissipations cause an exponential decay of the Rabi splitting. While in a lossless cavity the temporal extension of the coherent energy exchange would be infinite, in the real case it is instead exponentially suppressed. This suppression can drive the hybrid system into the weak coupling regime.

1.2.4 Strong coupling with vacuum fields

As we have seen, the interaction between photons tightly confined in an optical cavity and matter excitations can give rise to hybrid light-matter states, which inherit properties from both of their constituents. Importantly, the formation of these states does not necessarily require an external light source: they can also emerge in the dark, thanks to the interaction with the zero-point energy of the optical mode. The mere presence of such hybrid states can affect the intrinsic properties of the material [14].

This can be seen by rewriting the Rabi splitting, introduced in equation 1.23, from a microscopic perspective. It becomes [8]:

$$\Omega_R = 2|\vec{\mu}|\sqrt{\frac{N\omega_c}{2\epsilon_0 V}}\sqrt{\langle n_\gamma \rangle + 1}, \tag{1.31}$$

where $\langle n_\gamma \rangle$ is the average number of photons involved in the coupling mechanism and V is the volume of the electromagnetic cavity mode. It follows that strong coupling can occur even when $\langle n_\gamma \rangle = 0$, i.e. without any photon driving.

The basic idea is to replace the classical laser field, that can be used to control quantum materials through nonthermal pathways, with quantum mechanical photon modes in a cavity. Using a laser, the many photons created can occupy a macroscopic coherent state that can change the material's properties. Instead, using quantized modes, their effective optical volume can be reduced through a suitable surrounding, i.e. a cavity. Thus, the

light-matter coupling can be increased, making the number of photons required to change the properties of the material to be reduced, even to the point where no photons are necessary [3]. We refer to this as a *dark cavity*.

Through cavity engineering, it becomes possible to control the strength of the photon vacuum field by carefully designing the optical cavity. These vacuum fluctuations couple to the electronic or vibrational states of the material, leading to modifications of its ground state. An important distinction between the effects of strong light-matter coupling in cavity-engineered and laser-driven systems, lies indeed in the possibility of creating hybrid states at the equilibrium, where both quantum and thermal fluctuations play a significant role. This opens the way to the formation of new types of quasi-particles and phases that would not be achievable with conventional laser-based techniques [15].

This can be rationalized by hypothesizing different mechanisms. For example, cavity photons can hybridize with phonons to form phonon-polaritons, thereby enhancing the electron-phonon coupling and modifying the phonon frequencies. Another approach to explain the modification of the electron-phonon interaction involves the direct coupling of electrons to cavity photons. This interaction can alter the electronic density, indirectly affecting both phonon frequencies and the electron-phonon coupling [15].

1.3 Superconductors in cavity

As we have seen in the previous section, cavity engineering enables the control of the equilibrium properties of a material by coupling it to the quantized electromagnetic field. Recently, such approaches have been increasingly applied to superconductors, investigating how superconductivity can be modified or even enhanced through light-matter interactions at equilibrium. In this regards, there are two principal strategies. The first one is to use direct coupling of electrons and photons: the cavity photons can act as mediators of an attractive force between electrons that gives rise to a Cooper pairing and thus superconductivity. The second one is to couple the photons of the cavity to other degrees of freedom, for example phonons.

1.3.1 Theory proposals

Electron-photon direct coupling

The idea of the direct coupling is to provide a pairing force via the exchange of a virtual-photon between electrons, in analogy to the phonon-mediated pairing in BCS superconductors. Considering a paramagnetic coupling, the interaction mediated is current-current type, different from the conventional ones, suggesting that cavity-mediated pairing can give rise to superconductivity from a different pairing mechanism.

In particular, recent theoretical work has demonstrated that the superconducting behaviour of MgB_2 can be tuned through strong coupling to cavity modes, leading to an enhancement of the critical temperature T_c of up to 10% [16]. The mechanism that can describe how the vacuum fluctuations can affect electrons and photons is based indeed in this direct coupling. Thanks to the interaction of the electrons in the crystal with virtual photons from the quantum cavity, the electron density undergoes a redistribution in the Boron planes, concentrating around the potential local minima, such as σ bonds in MgB_2. This accumulation screens the Coulomb repulsion between Boron ions, thereby

reducing the restoring force of the E_{2g} Raman mode, that is the mode that drives the pairing in MgB_2. The result is a phonon softening that enhances electron-phonon coupling and increases T_c of up to 10%.

This study established that cavity-induced strong coupling is a non-perturbative mechanism that can modify both the electronic structure and the phonon dispersion, opening the path towards light-controlled equilibrium superconductivity.

The theoretical description of complex light-matter coupling within cavities is challenging due to the many degrees of freedom involved. A powerful approach to address this problem is quantum electrodynamical density functional theory (QEDFT), as presented in the article [16], which extends density functional theory (DFT) to include quantized electromagnetic fields. Using QEDFT, the Pauli-Fierz (PF) Hamiltonian describes light-matter coupled systems in the nonrelativistic regime. In the long-wavelength approximation and velocity gauge, it reads:

$$H_{\mathrm{PF}} = \frac{1}{2}\sum_{l=1}^{N_e}\left(-i\nabla_l + \frac{1}{c}\hat{A}\right)^2 + \frac{1}{2}\sum_{l\neq k} w(\mathbf{r}_l,\mathbf{r}_k) + \sum_{l=1}^{N_e} v_{\mathrm{ext}}(\mathbf{r}_l) + \sum_{\alpha=1}^{M_p}\omega_\alpha\left(\hat{a}_\alpha^\dagger\hat{a}_\alpha + \frac{1}{2}\right), \quad (1.32)$$

where N_e and M_p denote the number of electrons and photon modes, respectively. The Coulomb interaction between electrons is represented by $w(\mathbf{r}_l,\mathbf{r}_k)$, and $v_{\mathrm{ext}}(\mathbf{r}_l)$ is the external nuclear potential. $\hat{a}_\alpha$ ($\hat{a}_\alpha^\dagger$) is the photon annihilation (creation) operator, and the vector potential is given by

$$\hat{A} = c\sum_\alpha \lambda_\alpha \boldsymbol{\epsilon}_\alpha \frac{1}{\sqrt{2\omega_\alpha}}(\hat{a}_\alpha + \hat{a}_\alpha^\dagger), \quad (1.33)$$

where $\boldsymbol{\epsilon}_\alpha$ is the polarization vector of the α-th photon mode and λ_α its effective coupling strength.

Within QEDFT, the PF Hamiltonian can be mapped onto a Kohn-Sham system of electrons with an additional photon exchange-correlation potential:

$$H_{\mathrm{KS}} = -\frac{1}{2}\nabla^2 + v_{\mathrm{ext}}(\mathbf{r}) + v_{\mathrm{Hxc}}(\mathbf{r}) + v_{\mathrm{pxc}}(\mathbf{r}), \quad (1.34)$$

where v_{Hxc} is the standard Hartree-exchange-correlation potential and v_{pxc} accounts for electron–photon exchange-correlation effects. Approximations for v_{pxc} can be constructed in analogy to LDA by solving a Poisson-like equation for the effective photon-induced contribution.

The light-matter interaction strength in a cavity is parametrized by the ratio $\lambda_\alpha/\omega_\alpha$, controlled by cavity geometry and photon polarization. Large effective couplings can be achieved by reducing the mode volume or lowering the photon frequency.

Indirect coupling via phonons

An alternative approach is to couple the cavity photons to other degrees of freedom, potentially affecting the pairing mechanism responsible for superconductivity. Coupling with phonons could be advantageous, as they not only are responsible for the pairing mechanism in phonon-mediated superconductors, but also they have a role in high temperature superconductivity. The idea is to use phonon polariton formation to modify the effective electron-phonon coupling in superconductors.

Recent theoretical work [17] investigated the effect of embedding in a cavity system like monolayer FeSe on $SrTiO_3$ (STO). Together with forward-scattering electron-phonon interaction to the quasi two-dimensional conduction electrons in FeSe, they also considered the coupling of the cavity modes to the out-of-plane phonon mode in the STO substrate involving O and Ti vibrations near the interface with FeSe. The result is an indirect electron-photon coupling via phonon polaritons, that can be modelled with a forward-scattering vertex

$$g(q) = g_0 e^{-|q|/q_0}, \tag{1.35}$$

that is peaked at $q = 0$ with a coupling of g_0. Cavity photon-phonon coupling leads to the formation of phonon polaritons, characterized by a splitting between upper and lower polariton branches. The formation of these polaritons redistributes the electron-phonon coupling across the polariton modes. The redistribution is stronger for smaller q_0/k_F ratios and for larger ω_P, where k_F is the Fermi momentum and ω_P is the plasmonic frequency.

The effective electron-phonon coupling λ is enhanced in the cavity at all temperatures, with a pronounced peak near T_c. However, the polariton formation also softens the effective phonon frequency Ω. Since in the forward-scattering regime the critical temperature scales approximately as

$$T_c \sim \frac{\lambda\Omega}{2 + 3\lambda}, \tag{1.36}$$

the two effects, that are the enhancement of λ and the reduction of Ω, compensate, resulting, in the best scenario, in a little or no increase of the critical temperature, and in some cases even in a slight suppression.

Only in regimes of extremely sharp forward scattering ($q_0/k_F \ll 0.1$), the cavity can produce larger T_c shifts ($\sim$10K), though these conditions are not easily realized experimentally.

1.3.2 Experimental results

The theoretical works discussed above represent just two examples of a growing number of theoretical works and proposals that continue to emerge, reflecting the strong interest in this field. Nevertheless, while the theoretical landscape is rapidly expanding, experimental progress has been comparatively limited. Only a few demonstrations exist that provide evidence of changes in superconductivity [18, 19] or other material functionalities within cavities [20].

Cavity-controlled changes in the superconducting behaviour were recently announced in ref. [18]. In this work, the authors studied the molecular superconductor k-(BEDT-TTF)$_2$Cu[N(CN)$_2$]Br (k-ET), that is an organic salt with a superconducting critical temperature T_c=11.5K. In order to create an electromagnetic environment to control the properties of the material, it was interfaced with hexagonal boron nitride (hBN), a van der Waals hyperbolic material. Hyperbolic modes of hBN, characterised by a highly enhanced photonic density of states, overlap with the frequency of the carbon-carbon (C=C) stretching mode of k-ET, that is implicated in its superconductivity.

They also performed two control experiments: the first one replacing hBN with the insulator $RuCl_3$, that has optical phonons at lower frequencies, and therefore it does not resonate with the C=C stretching mode of k-ET; the second measurements was performed

with BSCCO, a different high-temperature superconductor, that does not display any resonance with the hyperbolic mode of hBN.

In order to study the ground state properties of the samples, the authors studied the superfluid density, that is a characteristic property of the superconducting phase at equilibrium. A strong suppression of superfluid density was observed only at the hBN/k-ET interface, while in the other heterostructures ($RuCl_3$/k-ET and hBN/BSCCO), no superfluid suppression was measured. This suggests that suppression of the superfluid density strongly related to the resonant nature of hBN/k-ET, thus it creates a ground state that is altered by the cavity.

An other experimental study was published in Ref [19], in which the molecular superconductor Rb_3C_{60} was studied under vibrational strong coupling to surface plasmon polariton. Rb_3C_{60} is a strongly correlated material in which superconductivity is phonon mediated and emerges below the critical temperature of 30K.

The coupling to phonons was achieved by embedding the system in a vibrational environment composed of polystyrene (PS). The polymer provides auxiliary vibrational modes that are resonant with the phonon mode of the sample and can strongly couple to the cavity photons. This polymer film was deposited on a gold layer, in such a way that the metal-dielectric interface generates surface plasmon polaritons. The polymer is strongly coupled to the surface plasmons and induces a *cooperative strong coupling* in the superconductor. In this manner, the weak phonon modes of Rb_3C_{60} were dressed through the vacuum field.

Through SQUID measurement, the authors characterized the Meissner effect of the sample, finding an enhancement of the critical temperature of 15K, that it is not present when the polymer layer is detached from the gold surface. The same study was conducted also for a PS+YBCO system, where on the contrary, a reduction of T_c was measured.

This result suggests that, while in BCS-like superconductors the electron pairing is mostly affected by low-energy vibrational modes, in cuprates the onset of the superconductivity is also controlled by high-energy electronic transitions. Therefore, a control of the superconducting transition could be achieved through the coupling with electronic degrees of freedom.

Building on this evidence, our aim is to design cavities that can hybridize high-energy electronic degrees of freedom, such as the charge-transfer excitations in cuprates. By targeting these modes, it might become possible to explore novel pathways for manipulating the superconducting state beyond phonon-mediated mechanisms. As will be discussed in the next chapter, this strategy opens the door to cavity engineering tailored for enhancing and controlling superconductivity through light–matter interaction at electronic energy scales.

Chapter 2

Design of the heterostructures

As discussed in the previous chapter, we are interested in understanding how high-energy electronic excitations can influence the superconducting properties of cuprates. Among these excitations, a particularly important role is played by the charge-transfer (CT) transition, a characteristic feature of the cuprate family.

In this chapter, we focus on $YBa_2Cu_3O_{7-\delta}$ (YBCO), a high-temperature cuprate superconductor that will serve as the reference material for our study. After introducing the optical properties of YBCO, we will highlight the CT transition and discuss how it can be hybridized with an optical cavity. The possibility of coupling the CT transition with a resonant cavity provides a powerful route to engineer light-matter interactions in the high-energy sector, potentially opening new perspectives for controlling superconductivity.

To design such cavities, it is crucial to determine the correct geometry that ensures resonance at the CT energy. For this purpose, we employ numerical simulations based on the *transfer matrix method*, a well-established formalism to model electromagnetic propagation in stratified media. This approach allows us to predict the spectral response of multilayer heterostructures and to optimize their parameters in order to achieve the desired resonance.

Finally, we present the results of these simulations, together with the complete set of heterostructures that have been designed and fabricated for experimental investigation.

2.1 Optical properties of YBCO

The structure of YBCO, as that of all cuprates, is layered, as schematically shown in figure 2.1. The optical properties are related to the copper-oxygen planes. In particular, the equilibrium properties are determined by the Cu $3d$ and O $2p$ orbitals.

Many properties of the parent compound, which is an insulator, are described within the three-band Hubbard model. These are an upper Hubbard band (UHB) and a lower Hubbard band (LHB), derived from the splitting of the Cu $3d$ band by a strong on-site Coulomb repulsion ($U \sim 8$–$10\,\mathrm{eV}$). In the between of these two bands, there is the O $2p$ band, which is fully occupied and lies $\sim 2eV$ below the UHB, as schematized in figure 2.2.

The transition from the O $2p$ band to the UHB represents the charge-transfer (CT) of a Cu $3d_{x^2-y^2}$ hole to its neighbouring O $2p_{x,y}$ orbitals in the CuO_2 planes [21]. The electronic energy bands are therefore distributed according to two energy scales U and Δ_{CT}.

We can identify two limiting cases:

- The first, *Mott–Hubbard insulator*, when $U \ll \Delta_{CT}$. In this case the fundamental absorption gap occurs between the upper and lower Hubbard bands, and therefore the gap is set by U;

- The second case is when $U \gg \Delta_{CT}$. The fundamental absorption gap occurs between the filled O $2p$ CT band and the empty UHB, so the gap is $E_g \sim \Delta_{CT}$. This second case is called *charge transfer insulator*.

High-energy spectroscopy studies suggest that cuprates belong to this second case: indeed, the lowest unoccupied band is mainly formed by Cu $3d$ states, while the highest occupied band derives from O $2p$ states [22].

By doping YBCO, the system evolves from insulator to metal: as doping increases, free carriers appear and one observes a loss of spectral weight above the CT gap, the development of a plasma edge, and a decrease of reflectivity intensity in the 1.5-5 eV range. From conductivity it is seen that below 1.5 eV the conductivity increases with doping much faster than the doping concentration, suggesting that the spectral weight lost above the CT absorption band is transferred to low energies with doping. This behaviour is different from that observed in simple semiconductors, where the low-frequency weight increases with the dopant concentration, while the spectral weight associated with the fundamental absorption band remains unchanged. Instead, the transfer of oscillator strength between different electronic levels with doping is a common feature of cuprates, as it has been observed also in other materials of the cuprate family [22].

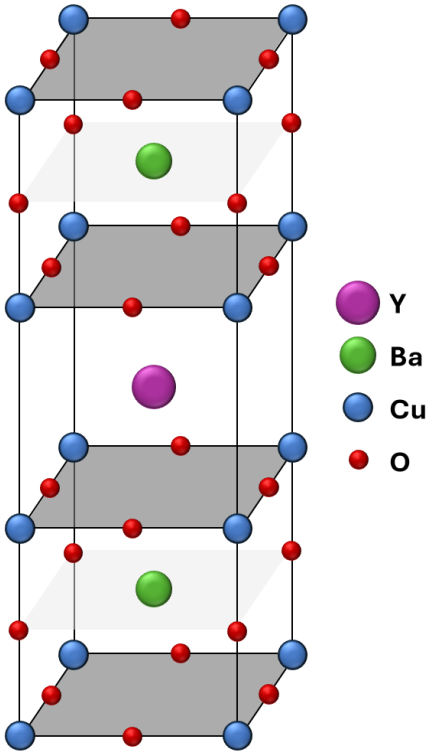

Figure 2.1: **Crystal structure of YBCO.** Yttrium and Barium atoms are alternated with Copper-Oxygen planes.

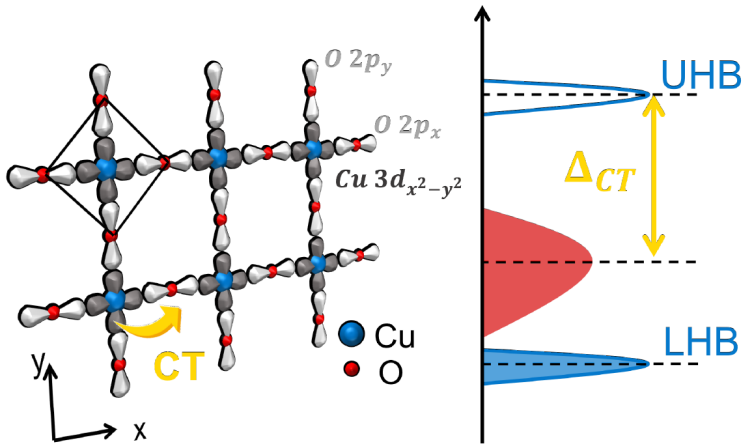

Figure 2.2: **Electronic charge transfer excitation in cuprates.** The electronic configuration of the CuO_2 planes in cuprates is sketched. The charge-transfer (CT), i.e. the lowest electronic transition, is highlighted in yellow. It is the transition from the O $2p$ orbitals to the upper Hubbard band (UHB). [8]

2.1.1 Charge-transfer hybridization

As seen in section 1.3.2, in BCS-type superconductors electron pairing is mostly affected by low-energy vibrational modes. On the other hand, in cuprates it is realistic to consider that high-energy electronic transitions contribute significantly to the onset of superconductivity. Such an involvement of high-frequency electrodynamics in the superconducting mechanisms is also suggested by the fact that several studies show that the CT transition is strongly modified upon entering the superconducting phase, and therefore could play a role in the pairing mechanism. For this reason, we focus on designing cavities resonant with the charge-transfer transition.

From the Fabry-Pérot analysis presented in the previous chapter, we find that in order to achieve resonance in the CT energy range 1.5-2 eV, the cavity length must be in the order of a few hundred nanometres (see eq. 1.2).

The simplest method to construct a resonant cavity consists in placing the sample between two parallel mirrors and tuning their separation, as demonstrated in [23]. This approach is well suited for cavities resonating in the THz regime, where the required cavity length is on the order of micrometers. Such a method is unfeasible because of the cavity length required by our sample. Therefore, our solution is to employ the use of heterostructures, which consists in a material system composed of layers of different materials.

By placing the superconducting layer between two metal layers (which serve as mirrors), buffered by two dielectric layers, we are able to construct a heterostructure which is a cavity (as schematized in figure 2.3), that can be made resonant with the energy of interest by changing the thickness of the different layers.

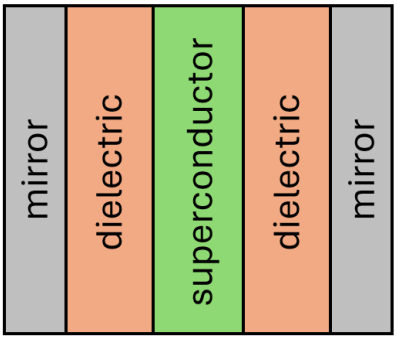

Figure 2.3: **Scheme of the cavity heterostructure.**

2.2 Simulation of heterostructures

As stated before, our goal is to realize heterostructure-based cavities with an appropriate geometry. To this end, we first design and simulate the structures in order to identify the optimal configurations for the various layers. The simulations are carried out using the transfer matrix method, which provides a reliable framework for modelling the optical response of multilayer systems.

2.2.1 Transfer matrix method

Transfer matrix is a formalism used to solve Maxwell equations and to study the electromagnetic wave propagation through a medium made of layers of different materials with their own refractive properties [24, 8]

We start by considering only one interface between two different media with refractive indexes n_0 and n_1. The light propagates from the medium with n_0 refractive index with an angle θ_0 to the medium with n_1 with an angle θ_1. The incident and transmitted light at the interface are linked through the Snell law $n_0 \sin(\theta_0) = n_1 \sin(\theta_1)$. The complex amplitude of the electric field at a position z can be written as:

$$E(z) = E^+(z) + E^-(z), \tag{2.1}$$

where E^+ and E^- are the electromagnetic waves travelling along the $+z$ and $-z$ direction. Considering the electric field oscillating perpendicular to the plane of incidence, the relation between the incident E_0 and transmitted field E_1 is $E_0^+ + E_0^- = E_1^+$. The reflection and transmission coefficients can be written as:

$$\begin{aligned} r_{01}^{\perp} &= \left(\frac{E_0^-}{E_0^+}\right)_{\perp} = \frac{n_0 \cos\theta_0 - n_1 \cos\theta_1}{n_0 \cos\theta_0 + n_1 \cos\theta_1} \\ t_{01}^{\perp} &= \left(\frac{E_1^+}{E_0^+}\right)_{\perp} = \frac{2n_0 \cos\theta_0}{n_0 \cos\theta_0 + n_1 \cos\theta_1}. \end{aligned} \tag{2.2}$$

For the case in which the electric field is parallel to the interface, in a similar way, we can

obtain the coefficients:

$$\begin{aligned} r_{01}^{\parallel} &= \left(\frac{E_0^-}{E_0^+}\right)_{\parallel} = \frac{n_1\cos\theta_0 - n_0\cos\theta_1}{n_0\cos\theta_1 + n_1\cos\theta_0} \\ t_{01}^{\parallel} &= \left(\frac{E_1^+}{E_0^+}\right)_{\parallel} = \frac{2n_0\cos\theta_0}{n_0\cos\theta_1 + n_1\cos\theta_0}. \end{aligned} \tag{2.3}$$

The previous two sets of equations are known as Fresnel's equation.

In order to obtain a full interference pattern, we must consider also the backwards propagating wave, that is the field propagating from medium n_1 into the medium n_0 at the same interface. The reflection and transmission coefficients for this configuration are linked to the previous one by the relations:

$$\begin{aligned} r_{10} &= \frac{E_1^+}{E_1^-} = -r_{01}, \\ t_{10} &= \frac{E_0^-}{E_1^-} = \frac{1 - r_{01}^2}{t_{01}}, \end{aligned} \tag{2.4}$$

which imply:

$$r_{10}r_{01} + t_{10}t_{01} = 1. \tag{2.5}$$

From the expressions of the reflectivity and transmittivity coefficients, considering both forwards and backwards propagation, we can write the electric field in the medium n_0 as a function of the electric field in medium n_1 through the *interface Transfer-matrix* equation:

$$\begin{pmatrix} E_0^+ \\ E_0^- \end{pmatrix} = \frac{1}{t_{01}} \begin{pmatrix} 1 & r_{01} \\ r_{01} & 1 \end{pmatrix} \begin{pmatrix} E_1^+ \\ E_1^- \end{pmatrix}. \tag{2.6}$$

By defying a two-dimensional vector Φ:

$$\Phi(z) = \begin{pmatrix} E^+(z) \\ E^-(z) \end{pmatrix}, \tag{2.7}$$

equation 2.10 becomes:

$$\Phi_0 = I_{01}\Phi_1, \tag{2.8}$$

where

$$\begin{aligned} \Phi_0 &= \begin{pmatrix} E_0^+ \\ E_0^- \end{pmatrix}, \\ \Phi_1 &= \begin{pmatrix} E_1^+ \\ E_1^- \end{pmatrix}, \\ I_{01} &= \frac{1}{t_{01}} \begin{pmatrix} 1 & r_{01} \\ r_{01} & 1 \end{pmatrix}. \end{aligned} \tag{2.9}$$

I_{01} is the Transfer-matrix at the interface of a single layer.

Before writing the Transfer-matrix for a multi-layer structure, we have to derive the matrix expression describing the free field propagation between adjacent interfaces. We can consider the electric field E_1 propagating in medium n_1 within a distance d. After the free propagation we label the field E_d. Therefore we will have the propagation equation:

$$\begin{pmatrix} E_1^+ \\ E_1^- \end{pmatrix} = \begin{pmatrix} \exp^{-in_1kd\cos\theta_1} & 0 \\ 0 & \exp^{-in_1kd\cos\theta_1} \end{pmatrix} \begin{pmatrix} E_d^+ \\ E_d^- \end{pmatrix}, \tag{2.10}$$

where k is the vacuum wave vector. The latter equation can be written, using the Φ-vector form 2.7, as:

$$\Phi_1 = L_{1d}\Phi_d, \tag{2.11}$$

where L_{1d} is the Transfer-matrix of free field propagation for a distance d within a medium with refractive index n_1.

Now we can combine the two propagation equations obtained for the interface and free field to obtain:

$$\Phi_0 = I_{01}L_{1d}\Phi_d = M_{01d}\Phi_d, \tag{2.12}$$

where M_{01d} is the Transfer-matrix describing the single layer structure in figure 2.4.

Equation 2.12 is the basic element to construct the optical response of a multilayer system, that can be constructed by stacking a number of individual single-layer units. The system has N layers, characterized by a thickness d_j and a refractive index n_j, and it is surrounded by two semi-infinite mediums on the left and on the right, with refractive index n_0 and n_{N+1} respectively.

Let us call Φ_0 the Φ-vector at the left boundary and Φ_S the vector at the right boundary of the N-layer system. The interference within the entire multilayer structure can be described by:

$$\Phi_0 = S\Phi_S, \tag{2.13}$$

where S is the total Transfer matrix of the multilayer system that considers all the interferences at each boundary:

$$S = \left(\prod_{j=1}^{N} M_{j-1,j,d_j}\right) I_{N,N+1} = \left(\prod_{j=1}^{N} I_{j-1,j}\, L_{j,d_j}\right) I_{N,N+1}. \tag{2.14}$$

To be explicit, equation 2.13 can be written as:

$$\begin{pmatrix} E_0^+ \\ E_0^- \end{pmatrix} = \begin{pmatrix} S_{11} & S_{12} \\ S_{21} & S_{22} \end{pmatrix} \begin{pmatrix} E_S^+ \\ E_S^- \end{pmatrix}, \tag{2.15}$$

where S_{ij} are the four matrix elements of the Transfer-matrix S. They depend on the thickness and on the refractive index of each layer.

In order to obtain the linear response of the full structure, we will consider an electric field oscillating perpendicular to the plane of incidence that enters the system from the left boundary and leaves from the right boundary. In this case there is no back-travelling light after the right boundary, therefore $E_S^- = 0$. The reflection and transmission coefficients are:

$$\begin{aligned} r_\perp &= \frac{E_0^-}{E_0^+} = \frac{S_{21}}{S_{11}}, \\ t_\perp &= \frac{E_S^+}{E_0^+} = \frac{1}{S_{11}}. \end{aligned} \tag{2.16}$$

$r_\perp$ and $t_\perp$ contain both the real and imaginary parts of the ratios, therefore they characterize both the amplitude and the phase response of the layered structure. The full spectral

transmission $T(\omega)$ and reflection $R(\omega)$ can be calculated as:

$$\begin{aligned} T(\omega) &= |t_s(\omega)|^2 = \left|\frac{1}{S_{11}(\omega)}\right|^2, \\ R(\omega) &= |r_s(\omega)|^2 = \left|\frac{S_{21}(\omega)}{S_{11}(\omega)}\right|^2, \end{aligned} \tag{2.17}$$

where the ω dependence is due to the frequency-dependent refractive indexes of the single layers ($n_j(\omega)$).

Therefore, in our specific case the transfer-matrix formalism allows to predict the full optical response of a multilayer cavity we want to study. In this regard we only need the cavity geometry and the complex refractive index of the different layers, that can be computed through the dielectric function, remembering the relation:

$$\tilde{n} = \sqrt{\varepsilon(\omega)} = n + ik, \tag{2.18}$$

that allows to write the complex refractive index $\tilde{n}$. The real part n is linked to dispersion effects, the imaginary part k to the absorption coefficients.

We will use two models to compute the dielectric function of the different layers: the Lorentz-Drude model and the Tauc-Lorentz model.

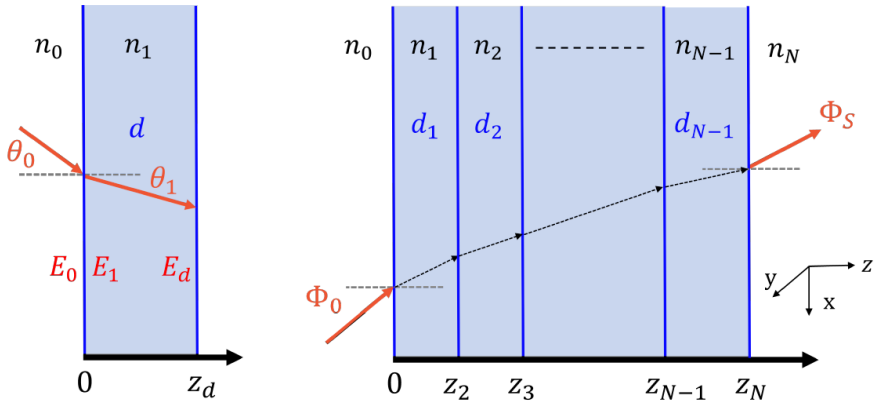

Figure 2.4: **Transmission through a layered structure in Transfer-matrix simulations.** Transmission through a two-media system (left) and a multilayer system (right). d_j and n_j are the thickness and the complex refractive index of the j-th layer.[8]

2.2.2 Numerical simulations

To investigate how strong electronic coupling can affect superconductivity, we designed YBCO heterostructures resonant with the charge-transfer (CT) transition of YBCO. The cavity structure is illustrated in Fig. 2.5: it consists of a reflective $LaNiO_3$ (LNO) layer grown on a thick $LaAlO_3$ (LAO) substrate, an insulating CeO_2 layer to decouple YBCO from the metallic layer, the YBCO film itself, and a second metallic mirror (Ag). In one sample, an additional CeO_2 capping layer was inserted on top of YBCO.

The thickness of the silver layer determines the cavity quality factor. A thicker silver layer traps photons inside the cavity for a longer time, leading to stronger coupling to the CT transition.

The dielectric functions of the layers were taken from literature [25, 22, 26, 27, 28] and modelled using the Drude-Lorentz and the Tauc-Lorentz models (see appendix B). Figure 2.6 shows the refractive index of YBCO, which exhibits an absorption peak at 1.8 eV, interpreted as the energy of the CT transition. For this reason, we designed heterostructures tuned to be resonant with this energy.

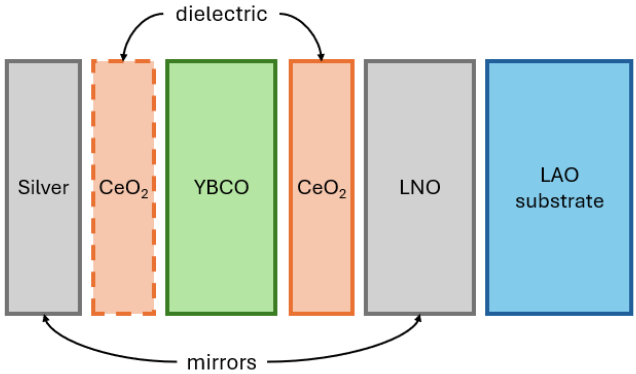

Figure 2.5: **Scheme of the multilayer cavity structure used in the simulations.** The dashed CeO_2 layer indicates that it is not present in all heterostructures.

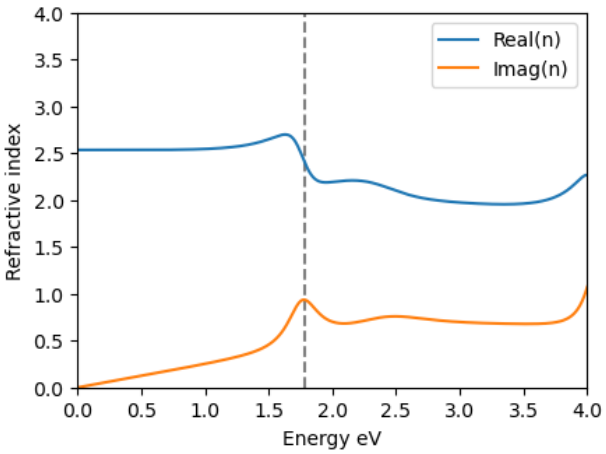

Figure 2.6: **Real and imaginary parts of the refractive index of YBCO.** An absorption peak is visible at 1.8 eV.

The simulation results[1] are reported in figure 2.7. Each panel shows the transmission spectra without (orange curves) and with (blue curves) the absorption of the YBCO layer. Neglecting absorption allows us to identify the cavity geometry required to achieve optical resonances at the desired energy. When the absorption of YBCO is included, the transmission peak around the CT resonance is suppressed and slightly shifted to lower energies.

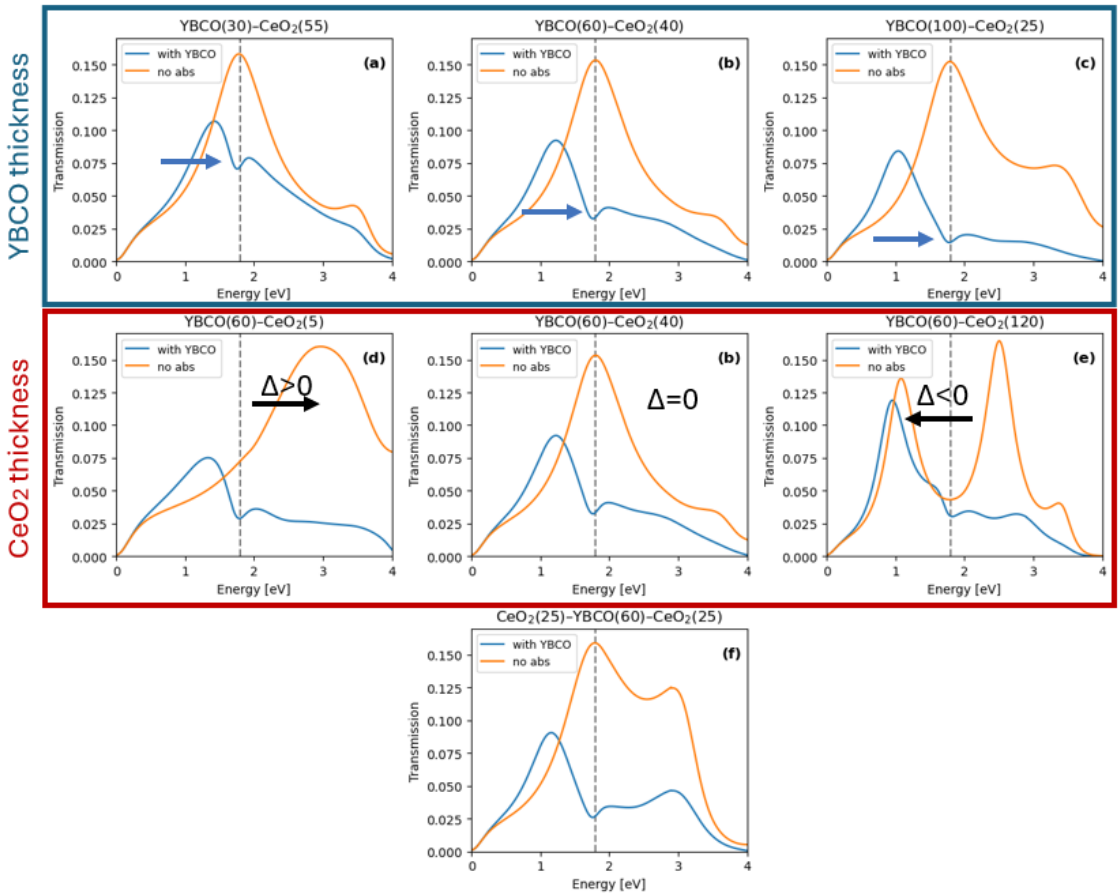

Figure 2.7: **Transfer-matrix simulations of transmission spectra.** Transmission of heterostructures with different YBCO and CeO_2 thicknesses. Orange curves: simulations neglecting YBCO absorption. Blue curves: full calculation including YBCO absorption. Panels (a), (b), (c), and (f) correspond to resonant cavities tuned to the CT transition at 1.8 eV, while panels (d) and (e) represent detuned cavities with positive and negative detuning, respectively.

The simulated structures, which correspond to the six final samples that were fabricated, are arranged in the figure as follows:

- **First row (a–b–c):** three different YBCO thicknesses were considered, namely 30, 60, and 100 nm. The CeO_2 thickness was chosen in each case so that the cavity resonance matches the CT transition at 1.8 eV, as indicated by the peak in the orange

[1] In all simulations, a silver thickness of 10 nm was considered.

curves. In the spectra including YBCO absorption, a minimum in the transmission is observed at 1.8 eV, corresponding to a maximum in absorption, as expected considering YBCO. Moreover, the depth of this minimum increases with YBCO thickness, showing that absorption grows with the thickness of the superconducting layer.

- **Second row (d–b–e):** here the YBCO thickness is kept fixed, while the CeO_2 thickness is varied to tune the cavity. In particular, samples (d) and (e) correspond to positive and negative detuning with respect to the CT transition, while sample (b) is shown again for comparison at exact resonance.

- **Third row (f):** this structure includes an additional CeO_2 layer deposited on top of YBCO. The geometry was optimized so that the cavity remains resonant with the CT transition.

In summary, samples (a), (b), (c), and (f) are resonant with the YBCO CT transition, while (d) and (e) are detuned by design.

2.2.3 List of Samples

In the following chapters, the samples under study will be classified based on the thickness, in nanometres, of the YBCO and CeO_2 layers. A list of these samples is presented below.

The three samples used to study the dependence on the YBCO layer thickness are:

- **Y30C55**: YBCO(30)/CeO_2(55)/LNO(100)/LAO;

- **Y60C40**: YBCO(60)/CeO_2(40)/LNO(100)/LAO;

- **Y100C25**: YBCO(100)/CeO_2(25)/LNO(100)/LAO.

The three samples used to study the dependence on the CeO_2 bottom layer are:

- **Y60C5**: YBCO(60)/CeO_2(5)/LNO(100)/LAO;

- **Y60C40**: YBCO(60)/CeO_2(40)/LNO(100)/LAO;

- **Y60C120**: YBCO(60)/CeO_2(120)/LNO(100)/LAO.

Note: The sample labelled as Y60C40 was used for both sets of measurements.

The final sample has a different structure, which includes an additional layer of amorphous[2] CeO_2 on top of the YBCO:

- **C25Y60C25**: CeO_2(25)/YBCO(60)/CeO_2(25)/LNO(100)/LAO.

All samples were divided into four quadrants: three of which were coated with silver layers of different thicknesses to form a closed cavity with a metallic top layer. These samples will be labelled by appending "AgX", where X represents the silver thickness in nanometres (0 for the open cavity, and 5, 10 or 15 for the closed cavity).

[2]The reason why only this sample is capped with CeO_2, and why this layer is amorphous, will be explained in the next chapter.

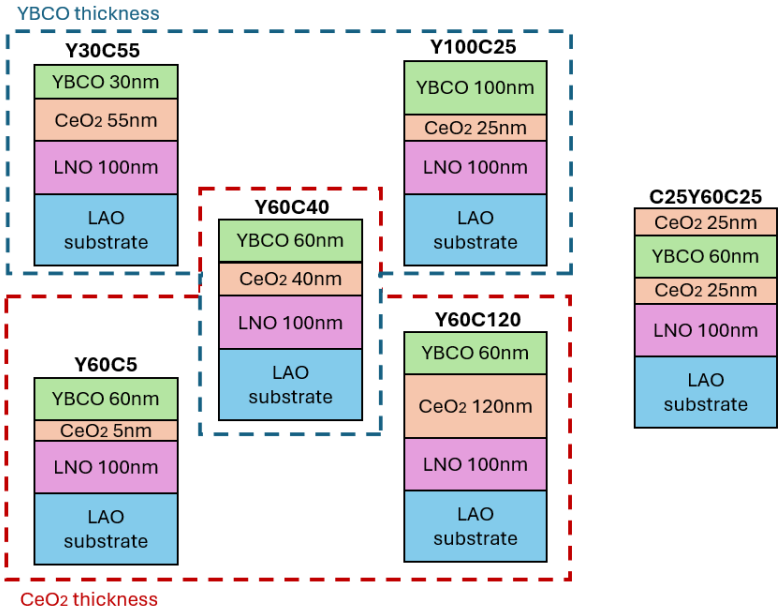

Figure 2.8: **List of Samples**: The blue box highlights the samples used to study the dependence on YBCO layer thickness. The red box shows the samples used to study the dependence on CeO_2 layer thickness. On the right is the sample capped with 25 nm of amorphous CeO_2.

Chapter 3

Synthesis of the heterostructures

In this chapter we will focus on the growth of the samples presented in the previous section, starting with a description of the technique used: Pulsed Laser Deposition (PLD), a popular and straightforward technique that can be used to grow a wide variety of materials, in particular multicomponent high-quality single crystals.

Pulsed laser light was used as energy source to evaporate thin films since the discovery of lasers in 1960s, but it was significantly developed starting from the 1980s, coinciding with the discovery of high-temperature superconductors, a class of oxides that presents different challenges in thin-film growth; this difficulty derives mostly from the fact that a correct stoichiometry and a oxidizing ambient is required in order to realize a epitaxial superconducting film.[29]

Then, we will present the characterization measurements that are needed to ensure epitaxial layers and the transport measurements performed to verify the superconducting behaviour of the samples. Finally, we will briefly describe the method used to deposit the silver layers.

PLD was performed at APE Beamline, Trieste, Italy[1].
The silver deposition was performed at CNR-IOM, Trieste, Italy[2].

3.1 Pulsed Laser Deposition technique

3.1.1 Overview

Pulsed Laser Deposition (PLD) is a physical vapour deposition technique in which a pulsed laser is focused onto a target of the desired material. When the laser fluence is sufficiently high, each pulse ablates a small amount of material, generating a plasma plume that expands away from the target and provides the flux for film growth. The film is then formed as the ablated species impinge on the substrate. The process is illustrated in Fig. 3.1.

This technique is widely used to grow complex material film thanks to different features. In the following, we briefly summarize these features, together with the main critical aspects

[1] CNR-IOM, Area Science Park - Ed.MM Basovizza, under the supervision of Prof. Giorgio Rossi, Dr. Sandeep Kumar Chaluvadi and Dr. Shyni Punathum Chalil.

[2] Area Science Park - Ed.MM Basovizza, Trieste, Italy, under the supervision of Dr. Luca Sbuelz and Dr. Simone Dal Zilio.

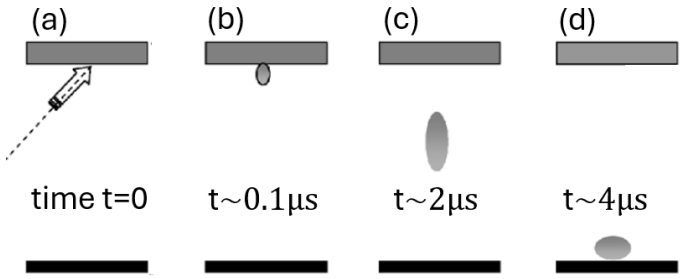

Figure 3.1: **PLD schematic process**: (a) A pulsed laser beam is focused onto the target (b) from which a small amount of material is ablated creating a plasma plume (c) that is highly directed to the substrate (d) where it impinges depositing the desired material on its surface. Adapted from [29].

that must be carefully considered during the deposition process.

Stoichiometric transfer

The first feature is the possibility to make stoichiometric transfer, during which the ablated material is deposited on the substrate with the same composition of the target[3]. This is possible thanks to the absorption of high laser energy density by a small amount of the material. If the laser fluence or the absorption is low at the laser wavelength, the laser pulse would only heat the target and the material would evaporize based on the vapour pressures of the different constituents of the target. In this way the ejected flux would not have the same composition of the target. Increasing the laser fluence, the ablation threshold is reached when laser energy absorption is higher than the one needed for evaporation, thus it depends on the laser wavelength and the absorption coefficient of the material. With an appropriate choice of these two parameters it is possible to make a small volume of material to absorb high energy densities, making the ablation process uniform, not dependent on the vapour pressures. For this reason is important that the target material has a high optical absorption coefficient at laser wavelength used.

Background pressure

The second reason for the broad applicability of this technique is the compatibility to do deposition process with background pressure up to hundreds of Pascals. The presence of a background gas is important because it can be a reactive species in the flux, necessary for the deposition of several multication thin-film materials, e.g. the presence of molecular oxygen for growing oxides. The chemical interaction between the ablated species and the background gas can produces molecular species in the plume making easier the formation of the multication phase. During the ablation process energetic species are generated, although this is a good behaviour in order to support this chemical interaction, these high kinetic energies (up to hundreds of electron volts) might introduce compressive stress in the growth film. The collisions of energetic atoms onto the surface can induce implantation

[3]For the growth of complex materials, it is possible either to employ separate targets for each element or to use a single stoichiometric target of the desired compound. In this work, we focus on the latter approach.

in the sub-surface to interstitial sites, creating a compressive stress that can cause bowing of the structure. The presence of a background gas can help to reduce or even eliminate this issue: in fact it can thermalize the plume, reducing the kinetic energy of the ablated material to less then 1eV.

Micron-size particles

A potential issue, in particular for the case of multilayer structures, is the ejection of micron-size particles during the ablation process. If these particles are deposited onto the substrate they can cause inhomogeneities in the structures compromising the growth of the different layers. This is often caused by a large penetration depth of the laser pulse into the target. This problem is easily solved using highly dense targets and, again, a wavelength that is strongly absorbed by the target material.

Lattice mismatch

During the growth of multilayer structures, it is also fundamental to have a good match between the lattice parameters of the different layers, in order to avoid stress that can induce deformation on the lattice structure. A mismatch between the substrate and the epitaxially grown layer could induce either a compression or an expansion of the lattice spacing. This deformation is quantified by the Poisson ratio, defined as $\nu = -\frac{\text{Radial strain}}{\text{Axial strain}}$. For instance, if the deposited material has a bigger lattice parameter than the substrate (figure 3.2), the lattice of the grown film will tend to have a in-plane compressive strain, while in the out-of-plane direction there will be a compensatory expansion.

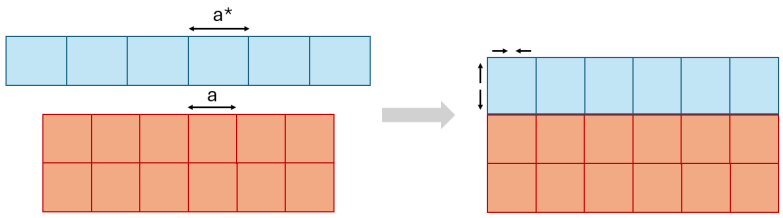

Figure 3.2: **Strain induced by a lattice parameter mismatch**: in-plane compressive strain and out-of-plane expansion in the case in which the lattice parameter of the grown film is bigger that the one of the substrate (a*>a).

3.1.2 Stages of Pulsed Laser Deposition

Now that we have introduced the principal aspects of the technique, we will now briefly focus to the principal stages of the Pulsed Laser Deposition, that can be divided into four steps:

1. laser light absorption and ablation of the target;
2. plasma formation and interaction with the laser;
3. plume expansion through the background gas (or in vacuum);
4. slowing down of the plume and deposition onto the substrate.

1. Light absorption in the target

During the first step, the laser light is absorbed by the solid target and atoms, ions and electrons are ejected from the target. The absorption mechanism varies according to the material's electron band-structure. Photons excite plasmons and free electrons, or excitons in the case of insulators. The response is described by the dielectric function $\epsilon(\omega, K)$. The electric field amplitude of the electromagnetic wave is

$$E = \sqrt{\frac{2\Phi}{cn\epsilon_0}}, \tag{3.1}$$

where Φ is the power density, ϵ_0 is the permittivity in free space, c is the speed of light and n is the refractive index. The threshold electric field for dielectric breakdown scales with the square root of the power density Φ, that is proportional to the laser fluence and inversely proportional to the laser pulse duration τ.

Reflection of the laser light also occurs, and even if it varies strongly during the pulse due to transient surface modifications, the effect is similar for all components in the target, and can therefore be neglected.

The energy absorbed by the solid will be dissipated in a large volume because of heat conduction. The excited electrons transfer their energy within few picoseconds, initiating heating within the optical absorption depth $1/\alpha$ (where α is the optical absorption coefficient).

In ablation of multi-compounds targets, congruent evaporation can occur only if the thermal diffusion length

$$l_T = 2\sqrt{D\tau}, \tag{3.2}$$

where D is the thermal diffusion constant, is smaller than $1/\alpha$. In this case the bulk will be heated down to $1/\alpha$ [30], ensuring that all species are heated within the absorption depth.

The intensity of the ablation is mostly determinated by the cohesive energy, that is the energy required to release an atom from a solid. Typical values range from 0.1×10^{15}atoms/pulse to 10×10^{15}atoms/pulse depending on the material [31].

During a typical PLD process, both evaporation and plasma formation processes are present. Many atoms can evaporate before the plasma plume is created, but the material ejected will have the same chemical composition of the target. If the laser intensity is not uniform, ablation will occur mostly in high intensity areas.

2. Plasma generation

Within the time duration of the laser pulse, a partly ionized plasma plume starts to form above the surface of the target. Initially the laser light interacts with both the ablating plume and the target behind. Electrons in the plume, as it continues to absorb light, will produce a plasma with ions from all the components of the target in a ratio that is similar to the original one. Therefore the target material under the plasma is screened from the remaining laser pulse, which is absorbed by the plasma that becomes more and more ionized. This process is known as *laser supported absorption* [30]: it can produce a plasma plume with high kinetic energies, ranging from a few to hundreds of electron volts. The degree of ionization after a nanosecond pulse can be almost unity. Moreover, the plume pressure can reach several bars, providing the driving force for the expansion of the plume.

3. Plume expansion

When the laser pulse ends, the plume front has propagated approximately 30–100 µm from the target surface. In the early stage, the expansion is quasi one-dimensional, subsequently evolving into a forward-directed three-dimensional adiabatic expansion. This process is driven by a pressure of 5–10 bar, sustained by the high temperature of the ablation plume. At distances of 200–500 µm, the kinetic energy of the expanding species surpasses the plume's thermal energy, marking the transition to a kinetically dominated regime [31].

If the plume expands in vacuum, the plume particles undergo free motion. In the presence of a background gas, the same applies until the plume pressure decreases. Theoretically, the velocity of the ablated species should be inversely proportional to the square root of the atomic mass. However, this behavior is typically not observed. Looking at the spatial distribution, it is found that the concentration of lighter elements is higher near the centre of the deposited material. This deviation from stoichiometry can be significantly reduced if the plasma temperature is increased up to 4000–20000 K. For YBCO, in particular, the velocity of the ablated atoms follows a scaling law of $m^{-0.37}$, and the lighter elements are more concentrated at the centre of the film [32].

The migration of the plume into the background gas follows a standard diffusion law, where the current in the x-direction is

$$J_x = -D\frac{dn_A}{dx} = -\frac{1}{3}v_A\lambda_A\frac{dn_A}{dx} \tag{3.3}$$

where n_A is the concentration of the A-component, D is the diffusion constant, and v_A and λ_A are the instantaneous velocity and the mean free path between collisions of the A-atoms with the background gas atoms. The velocity in a thermalized confined plume scales as $v_A \sim m_A^{-1/2}$. The mean free path is $\lambda_A = (\sqrt{2}\sigma n_g)^{-1}$, where σ is the scattering cross-section of the background gas atoms and n_g is their number density [31].

It can be observed that the cross section increases with the mass of the plume atom, and this dependence can be approximated by

$$\sigma \propto m_A^{0.9}, \tag{3.4}$$

which leads to the following scaling for the diffusion constant:

$$D \sim m_A^{-1.4}. \tag{3.5}$$

This relation shows that lighter atoms diffuse faster than heavier ones. As a consequence, non-stoichiometry may arise when the plume is at rest, since in this regime the distribution of atoms in the background gas is governed by diffusion.

4. Film growth

Finally, atoms arrive to the substrate surface. As they come from a laser ablation plume, they have sufficient kinetic energy to diffuse on the surface until they form stable and energetically favourable bonds with the substrate or other layer atoms. For a stoichiometry growth of the film it is necessary that all atomic species arrive at the substrate with the correct ratio and with adequate surface mobility.

The amount of film growth per laser pulse depends on the distance between target and substrate, the already mentioned background gas pressure, the laser spot size and the

energy density; usually the ablated material corresponding to one laser shot is sufficient for a sub-monolayer growth of the film (from 0.001 to 1Å). Thank to this reason, with PLD shot-to-shot growth control is possible, making this technique ideal for multilayer structures and interface formation.

3.1.3 Experimental setup

In our setup we have substituted the traditional KrF excimer laser with a solid-state $Nd:Y_3Al_5O_{12}$ laser. Using its fundamental frequency at 1064nm, high-quality complex oxide perovskite thin film deposition, such as YBCO, is possible [33]. The laser is placed in front of the entry-window, that is the optical access to the vacuum chamber, as shown in figure 3.3.

The laser has an output energy of 700mJ, with an extremely high stability of the laser pulse energy, minor than 0.7%, allowing an ablation rate stable over time. The maximum repetition rate can be achieved is 10Hz, smaller rates can be obtained by regulating the opening of the optical cavity. The beam diameter is 6mm.

Differently from the KrF excimer lasers, in Nd:YAG laser the laser output energy is not tunable. In order to resolve this problem, the fluence of the laser pulse can be reduced by putting an alumina ceramic piece with a variable diameter hole as laser mask. Finally a focus lens is placed after this mask to focus the laser pulses into the target with a incident angle of 45°.

As we need to deposit layers of different materials, it is possible to put different targets inside the main chamber, that can be selected rotating their holder. From picture 3.3 we can see that a mask with a hole is covering the targets, the selected one will be put in correspondence of the hole, in this way during the deposition process all the rest of the targets will be protected from contamination due to the plasma plum ablated from the selected target. Right down to the target, the sample holder is placed, its height can be regulated and it can be heated up to 700°C.

Inside the main chamber the vacuum can reach values of $\sim 10^{-8}$mbar. Since oxide growth requires an oxygen ambient, the pressure of the chamber is generally elevated. The exact value will depend on the specific layer we are growing.

Finally, the loading of samples is not done directly through the main chamber, to avoid air exposure. A smaller chamber, called load lock, is connected to the main one through a tube that stays always in vacuum. To load and take off the sample, only the load lock reaches ambient pressure, avoiding contamination inside the main chamber.

3.2 Growth of the samples

Here we will describe the growth process for the different heterostructures presented in section 2.2.3. We will start from the growth of the single layer in order to characterize them, to understand the right values of pressure, time deposition, distance between the target and the substrate. Then we will describe the process for fabricating the entire sample.

3.2.1 Deposition of single layers

For the characterization of YBCO layer and the heterostructures, we used $LaAlO_3$ (LAO) [001] substrate, with a lattice parameter of 0.379 nm. For the characterization of the

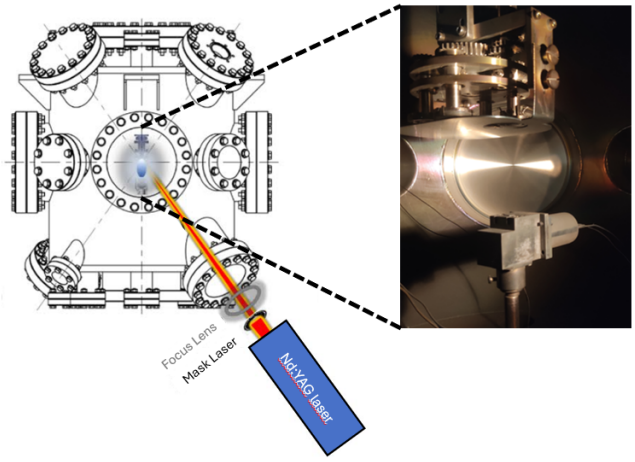

Figure 3.3: **PLD setup**: To the left a schematic representation of the setup, the Nd:YAG laser is just in front of the window, requiring only a laser mask and a focus lens.[33] To the right, a picture of the inside of the chamber; up we can see the targets that can be selected, in the center the sample holder that can be heated up to the desired temperature.

metallic and insulating bottom layers, we employed $SrTiO_3$ (STO) substrate, which has a lattice parameter of 0.3905 nm, that is close to that of LAO.

YBCO has an orthorhombic crystal structure with lattice parameter a=0.382nm, b= 0.389 nm (in-plane) and c= 1.168 nm (out-of-plane)[34, 35].

The metallic $LaNiO_3$ (LNO), the bottom layer that plays the role of first mirror in our cavity, has a nearly cubic perovskite structure in the [012] direction with a lattice parameter of 0.383nm.

The structure of CeO_2 is a cubic fluorite type with a=0.54097nm. If it is grown on LAO or on STO the in-plane lattice parameter is 0.38252nm, with the lattice cell rotated of 45°[33].

Thus, all these materials have lattice parameters comparable to the in-plane one of YBCO, making them suitable for the growth of our heterostructures, as the strain induced by the substrate or the bottom layers will be minimized.

As we already underlined, an important parameter during the growth of a thin layer is the pressure of the background gas. As we are growing oxides, in the chamber there will be an oxygen ambient, with the pressure adjusted according to the specific layer being deposited. In the case of the YBCO higher oxygen pressure will be required, as the superconducting behaviour is strongly dependent on the oxygen content. Additionally, a post-annealing at very high pressure will be performed for the YBCO, in order to compensate any possible oxygen deficiencies.

In order to estimate the crystal quality and the thickness of the layer we performed X-Ray Diffraction (XRD) and X-Ray Reflection (XRR), whose results are shown in figures 3.4 and 3.6 and explained below.

XRD

In order to investigate the crystal structure and to calculate the lattice parameter and strains in the layers grown, we have used X-Ray Diffraction. This technique is based on the elastic scattering of X-rays by the periodic planes of the crystal. The known Bragg's law

$$n\lambda = 2d\sin(\theta) \tag{3.6}$$

describes the condition for constructive interference of the scattered waves. In the equation n is the diffraction order, λ is the X-ray wavelength, d is the distance between the atomic planes and θ is the incident angle. By measuring the diffraction peaks and their angular position (as plotted in figure 3.4), the out-of-plane lattice parameter can be determined, revealing also possible distortions in the crystal structure.

The setup to perform XRD consists in three main components: (1) a X-ray source that generates radiation with a wavelength of $\lambda = 0.154056nm$, followed by a monochromator to ensure a well defined beam, (2) a goniometer on which the sample is mounted and (3) the detector that records the intensity of the diffracted beam as function of the angle. The goniometer and the detector can do precise angular movements, in the $\theta - 2\theta$ geometry, where the sample is rotated by θ through the goniometer and synchronously the detector rotates by 2θ.

The analysis of diffraction peaks of single layers yielded the following values for the out-of-plane lattice parameters:

- $c_{LNO} = (0.382 \pm 0.001)nm$,
- $c_{CeO_2} = (0.541 \pm 0.001)nm$,
- $c_{YBCO} = (1.175 \pm 0.004)nm$.

The lattice parameters are consistent with the expected values for the first two layers, unlike YBCO, which exhibits dilation in the out-of-plane direction compared to the expected value. This result agrees with the observations discussed above regarding strain due to lattice mismatch. In fact, YBCO has an in-plane lattice parameter larger than that of the substrate, leading to dilation along the out-of-plane direction. Evaluating the Poisson ratio considering the strain induced by the LAO substrate, we obtained $\nu \sim 0.3$; for YBCO $\nu = 0.314$ [35], confirming that the observed dilation is due to the strain induced by the substrate.

Moreover, by observing the diffraction peak graphs, we can notice that only (00l) peaks are present for all three materials. This indicates that the grown layers are monocrystalline.

XRR

X-Ray Reflection is a technique that can be used for plenty of purpose, such as the estimation of the thickness of the film or the roughness of the interface, also informations about the density of the film can be extrapolated. In this section we will focus on the study of the thickness of the layer grown.

Let's consider a single layer with thickness Δ grown over a substrate, as in figure 3.5. In contrast with an infinite slab in which only one reflection is possible at the interface, in the case of a film with finite thickness there are infinite possible series of reflections:

1. reflection at interface 0-1 with amplitude r_{01};

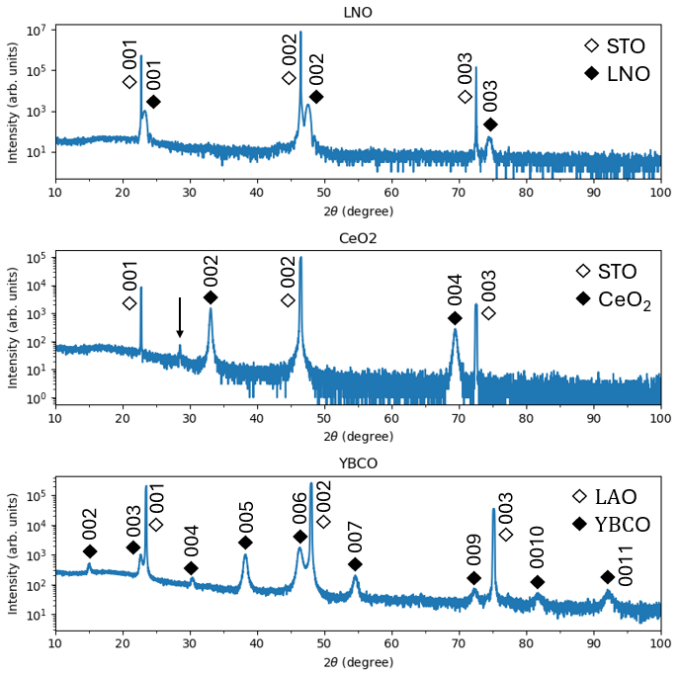

Figure 3.4: **XRD data for single layer.** $\theta-2\theta$ out-of-plane X-ray diffraction for the LNO and CeO_2 film grown on STO (001) and for the YBCO film grown on LAO (001); except for the small peak (marked by the arrow) in the CeO_2 graph, most likely due to a small contamination of CeO_2 (111) or some instrument issue, there are only (00l) diffraction peaks.

2. transmission at interface 0-1 (t_{01}), reflection 1-2 (r_{12}), transmission 1-0 (t_{10}). The amplitude of the reflective wave will be given from all these contributes including the phase factor $t_{01}r_{12}t_{10}e^{iq\Delta}$;

3. same as before with an other reflection step more, so transmission t_{01}, reflection r_{12}, reflection r_{10}, again reflection r_{12} and finally transmission t_{10}. The total phase factor will be $e^{2iq\Delta}$;

4. following with same scheme.

Therefore total amplitude reflectivity is:

$$r = r_{01} + t_{01}r_{12}t_{10}e^{iq\Delta} + t_{01}r_{12}^2r_{10}t_{10}e^{2iq\Delta} + ... \tag{3.7}$$

which is a geometric series, and using Fresnel equations the expression for the reflectivity can be written as:

$$r = \frac{r_{01} + r_{12}e^{iq\Delta}}{1 + r_{01}r_{12}e^{iq\Delta}}, \tag{3.8}$$

that gave the expression for the so-called Kiessig fringes [36], due to the interference of waves reflected from the two interfaces. The peaks in the oscillations, that we can observe also in our data in figure 3.6, correspond to the waves scattering in phase, whereas the dips to the out of phase scattering. The oscillations have a period of $2\pi/\Delta$, letting us estimate the thickness Δ of the layer grown.

The thicknesses found for the three single layer are:

- $\Delta_{LNO} \simeq 16nm$,
- $\Delta_{CeO_2} \simeq 28nm$,
- $\Delta_{YBCO} \simeq 28nm$.

Considering the condition under which we have grown these layers, in particular the laser rate and deposition time, we can estimate how many laser shots are needed to grow a layer of 1nm. The results are summarized in table 3.1.

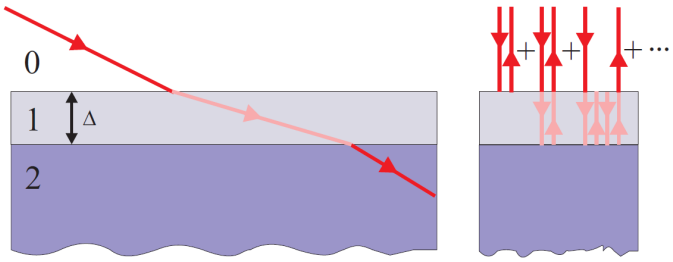

Figure 3.5: **Reflection and transmission scheme from a finite thickness layer.** The layer with thickness of Δ (1) is grown above the substrate (2), the total reflectivity is the sum of the infinite reflections, as shown in the right picture. [36]

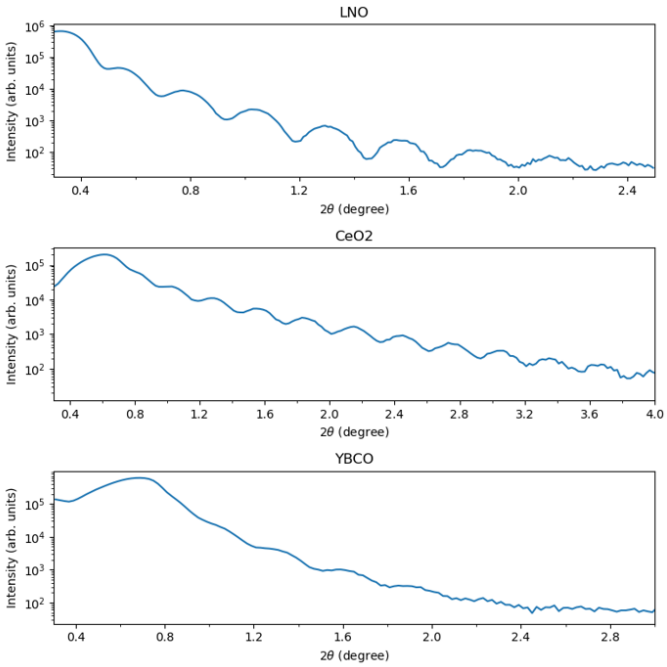

Figure 3.6: **XRR data for single layer.** Low-angle x-ray reflectivity curves that show oscillations up to 2θ of $\sim 2°$, $4°$ and $2°$ for LNO, CeO_2 and YBCO film respectively.

Transport

Transport measurements are generally performed in a standard 4-probe configuration, in which two electrical contacts are used to apply the current and the other two to measure the voltage drop. This method eliminates the contribution of the contact resistance, allowing for an accurate determination of the intrinsic resistivity of the material. In some cases, however, we will also employ the 2-probe configuration. In this setup, only two contacts are used, serving simultaneously for current injection and voltage measurement. In this configuration the measured resistance includes not only the sample resistance but also the contribution of the contacts. Both configurations are schematically shown in figure 3.7.

After verifying the crystal structure and thickness of the deposited layers, we characterized the YBCO film to confirm its superconducting properties. Transport measurements were performed in the 4-probe configuration, and the results confirmed the superconducting behaviour of the grown layer, with an onset critical temperature of 70 K, as shown in figure 3.8.

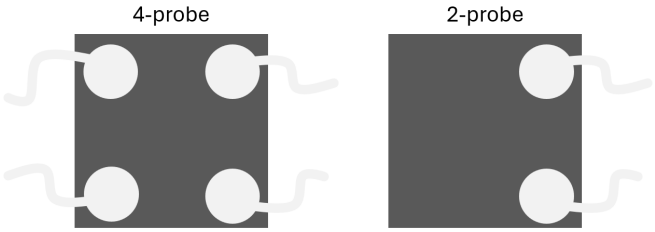

Figure 3.7: **Schematics of 4-probe and 2-probe electrical contacts for transport measurements.** In the 4-probe configuration, two contacts are used for current injection and two for voltage measurement. In the 2-probe configuration, both current and voltage are applied and measured through the same pair of contacts.

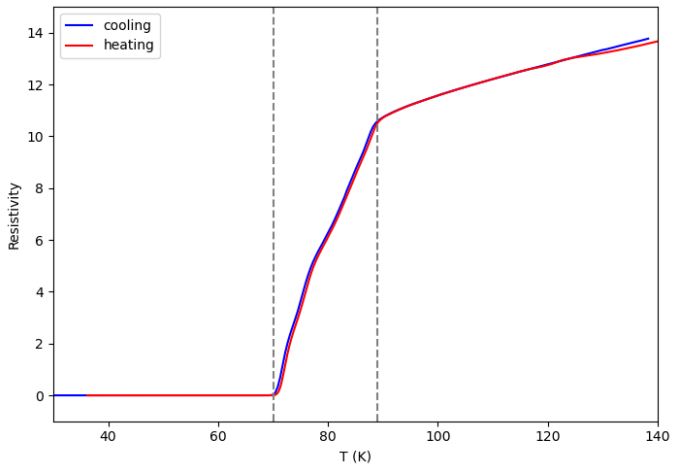

Figure 3.8: **Transport data for YBCO single layer**: Resistance vs temperature measurement performed with a typical 4-probe configuration for the YBCO grown on LAO substrate. It shows $T_c^{zero} \simeq 70K$.

Table 3.1: **Parameters estimated by single layer growth**, used for the deposition of the entire heterostructures.

	LNO	CeO_2	YBCO
Temperature	700°C	700°C	700°C
Substrate-target distance	6.3cm	7cm	6.3cm
Oxygen pressure	1×10^{-1} mbar	5×10^{-4} mbar	1×10^{-1} mbar
n° shots/1nm	150	65	144
Post-annealing	-	-	500°C, 100mbar, 75min

3.2.2 Deposition of multilayers

The growth of each layer was carried out consequently using the parameters found during the deposition of single layers. In order to oxygenate the YBCO layer, the entire samples were post-annealed for about 75min, at 500°C in oxygen atmosphere at 100mbar. As presented in section 2.2.3 we grew samples with different combinations of thicknesses of YBCO and CeO_2, all of them with free YBCO on top. Only one sample was capped with amorphous CeO_2, in order to have a dielectric buffer layer both below and above the YBCO. In order to obtain an epitaxial layer above YBCO, the deposition of top CeO_2 layer would need to be carried out at 700 °C and 5×10^{-4} mbar, i.e., at a higher temperature and lower pressure compared to the conditions used for the post-annealing of the YBCO layer. Such conditions would lead to oxygen loss from YBCO, thereby compromising its superconducting properties. To avoid this issue, we attempted to grow a CeO_2 layer at room temperature: due to the lack of thermal energy of the species after reaching the substrate (because of room temperature), the film grows amorphous.

In figure 3.9 the XRD data for sample Y100C25 are plotted. The high structural quality of the heterostructure is confirmed, as expected from the XRD data of the single layers: only (00l) oriented peaks of YBCO (+), CeO_2 (⧫) and LNO (•) are visible, confirming the preferential orientation along this crystallographic direction for all of the layers. Furthermore, the presence of spurious phases can be neglected, as no additional diffraction peaks are observed beyond those already cited.

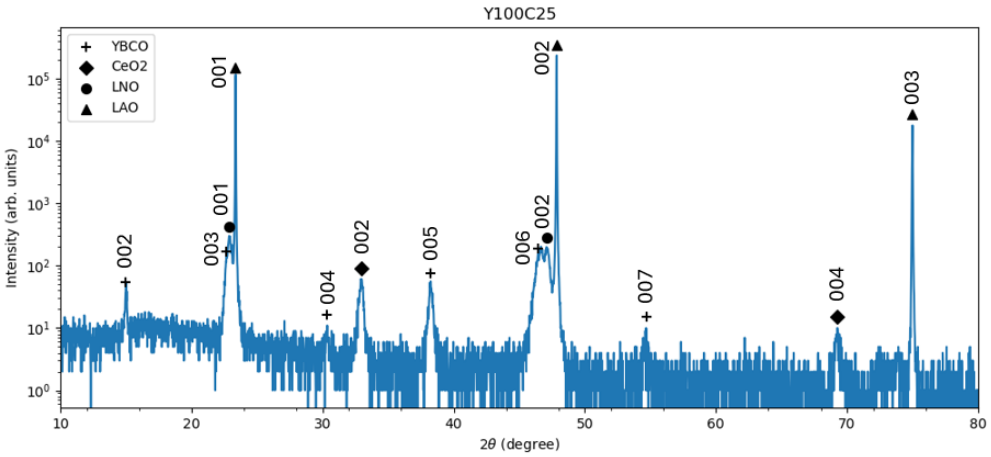

Figure 3.9: **XRD data for sample Y100C25**: $\theta - 2\theta$ out-of-plane X-ray diffraction for the heterostructures with 100nm of YBCO, 25nm of CeO_2 and 100nm of LNO layer.

Transport measurements were carried out for all samples except C25A60C25. In this case, the presence of an insulating layer sealing the cavity made it impossible to apply electrical contacts to perform the measurement.

In figure 3.10 the transport measurement performed for the sample Y100C25[4] shows the possibility to have a rough estimation of the critical temperature also using a 2-probe configuration. The need to use a 2-probe configuration, instead of the more common and accurate 4-probe, arises from the fact that contaminations of indium occurs by making electrical contacts for transport measurements in the four corners of the sample. Having unknown contaminants in the samples is not optimal, considering the subsequent measurements that were planned. Therefore, a 2-probe configuration was chosen, which still allows the estimation of the central transition temperature, while having the advantage of contaminating only two corners of the sample. These corners will be cut off later, thus leaving a "clean" sample, even if smaller.

For sample Y100C25, the estimated central critical temperature is $T_c \simeq 67K$, for sample with the thinnest YBCO layer (30nm) is $T_c \simeq 57K$, suggesting an higher critical temperature if the thickness of YBCO is higher. In fact for the intermediate level of YBCO (60nm) we recorded critical temperature between $63K$ and $66K$. For the latter thickness of YBCO we have three different sample with different thicknesses of CeO_2 layer (120-40-5nm): the critical temperatures are $64K$, $66K$ and $63K$ respectively. This difference in the values may be due to small differences in the YBCO layer (thickness or oxygen content). The main difference is in the transition width, which is getting wider with the thickness of the dielectric layer, as shown in figure 3.11.

All the critical temperatures are summarized in table 3.2.

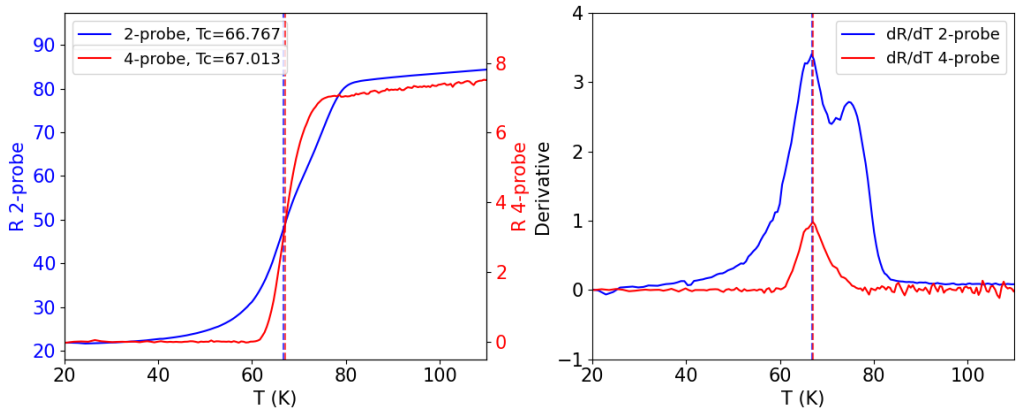

Figure 3.10: **Transport data for sample Y100C25**: To the left, in red transport measurement performed with the typical 4-probe configuration, in blue with only 2-probe. To the right, the derivative of the resistance. The transition is wider for the 2-probe measurement, but the point with the higher derivative is at the same temperature, letting us to estimate the critical also in this configuration.

[4]It is important to underline that the sample used for this measurement is not exactly the same of the one used for the XRD data and for the following measurements. The procedure used during the deposition process is the same, but due to small difference in, for example, the background pressure or the time of deposition, small difference in the layers are possible. Furthermore, the XRD data taken for the sample we will use in the next measurements, shows that the quality of the heterostructures is good, then it is reasonable to think that the critical temperature found with the other sample is at least comparable to the one we will use (this will be confirmed in the next chapter).

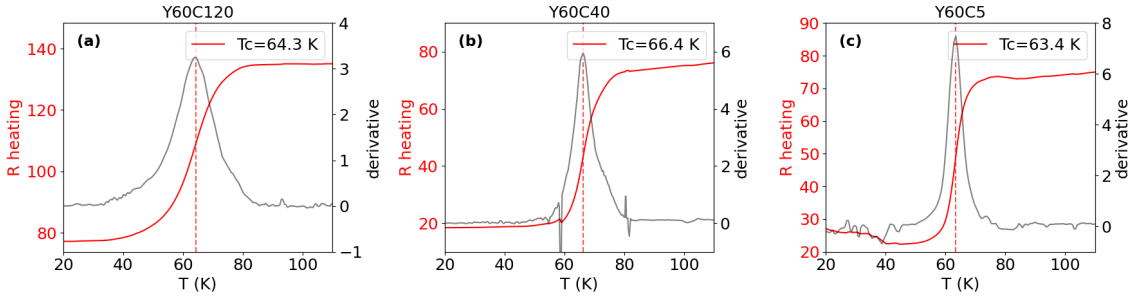

Figure 3.11: **Dependence of transport measurements on the thickness of the CeO_2 layer**: The samples under studies are the sample with 60nm of YBCO and different thicknesses of CeO_2: (a) 120nm, (b) 40nm and (c) 5nm of CeO_2. The transition is getting wider with the thickness of the dielectric layer.

Table 3.2: **Critical temperature T_c from transport measurements.** The values are estimated from transport measurements as the point with maximum derivative.

Sample	T_c (K)
Y100C25	67
Y60C120	64
Y60C40	66
Y60C5	63
Y30C55	57

3.3 Deposition of silver layer on top

We finally closed the heterostructures with three different thicknesses of silver, 5, 10 and 15nm. In order to avoid artefacts, the different layers of silver were deposited on the same heterostructures, dividing the sample into four quadrants, as shown in figure 3.12. One portion was left free of silver, to use it as reference for the future measurements. In order to obtain this different quadrants, we performed two successive depositions: the first one consisted in a deposition of 5nm of silver, while half of the sample was masked, the second one was performed depositing 10nm of silver after rotating the mask by 90°.

Silver was deposited by electron-beam evaporation, a Physical Vapor Deposition (PVD) technique in which an high power electron beam is used to heat a silver target, causing it to evaporate. The evaporated silver particles fly upwards in the vacuum chamber and are deposited onto the sample, that is placed above the source material. The film thickness is monitored using a rotating quartz crystal placed at the same distance: the evaporated silver also accumulates on the quartz, altering its oscillation frequency, which can be correlated to the thickness of the deposited film.

We want to emphasize that during the e-beam evaporation process the heating is limited to the target by means of the electron beam. Neither the entire chamber nor the sample holder is heated. This aspect is crucial to ensure that the properties of the previously grown layers are not altered. By contrast, as we already seen, in PLD the substrate must be heated, which would modify the underlying layers.

Moreover, for future considerations, it is important to underline that the silver deposited

with e-beam evaporation is polycrystalline, in contrast to the other layers grown by PLD (with the only exception of the amorphous CeO_2 layer on top of the YBCO).

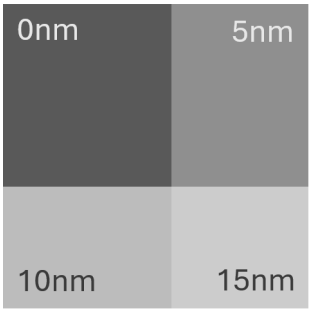

Figure 3.12: **Scheme of deposition of silver layer**: in order to obtain three distinct silver thicknesses, two successive depositions were performed. The first deposition consisted of 5nm, applied while masking half of the sample. The second deposition of 10nm, was carried out after rotating the mask by 90°. With this procedure four quadrants with different thicknesses, including one without any silver, were obtained.

Chapter 4

Microwave absorption measurements

We have observed that transport measurements can only be performed on uncapped samples, those terminating with the YBCO layer. In samples where the YBCO is covered either with CeO_2 or silver, it is not possible to make electrical contacts to measure the resistivity of the superconducting layer. Therefore, in order to estimate the critical temperature of such samples, it is necessary to employ alternative techniques, such as microwave absorption (MWA), which allows one to probe the superconducting behaviour of the sample through its magnetic properties, as was already investigated in previous works such as [37, 38, 39].

In this chapter, we present the experimental setup employed for the MWA measurements on all samples. We describe how this technique has been adapted to investigate the superconducting state of our samples, by exploiting the Meissner effect, that is the expulsion of the magnetic field from the sample when the temperature falls below the critical temperature T_c and the applied field is below the critical field H_c.

We will present the results obtained for the open cavities, i.e. samples without silver, and for the closed cavities, those samples in which the YBCO layer is covered with silver that plays the role of second mirror. We will see how the critical temperature and the transition shape changes depending on if the YBCO layer is free or not, and whether or not there is the amorphous CeO_2 buffer layer between the YBCO and the silver.

MWA was performed at Leibniz Institute for Solid State and Materials Research of Dresden, Germany[1].

4.1 Experimental setup

The experimental setup used in this work is a Bruker EMX EPR Spectrometer. This instrument is conventionally based on electron paramagnetic resonance (EPR), where microwave radiation is used to induce spin transitions of unpaired electrons in the presence of an external magnetic field (for more details see appendix A). However, in the case of superconductors below the critical temperature T_c, since the electrons are bound into Cooper pairs, there are no free paramagnetic spins available. What can be measured with microwaves is the magnetic response of the superconducting state, in particular the screening of the external magnetic field, i.e. the Meissner effect.

[1] Under the supervision of Dr. Alexey Alfonsov and Dr. Vladislav Kataev.

Therefore we are interested in measuring the microwave absorption (MWA) of our samples. The use of microwaves is particularly suitable for this purpose because the corresponding photon energy lies well below the superconducting energy gap. As a result, the radiation does not break Cooper pairs, unlike higher-frequency excitations. Microwaves interact with the collective electromagnetic response of the condensate, allowing us to monitor absorption changes associated with the superconducting phase of the sample. This makes MWA a powerful and non-destructive probe of the critical temperature and the magnetic properties of superconductors.

The setup consists of three main components: the microwave bridge, that contains the radiation source and the detector, the cavity, where the sample is placed, and the magnet, that allows to apply a magnetic field. The main parts of the microwave bridge are displayed in figure 4.1.

Starting from the microwave source (A), whose output power is fixed, subsequently there is an attenuator (B) that allows to precisely control the power of the microwave radiation reaching the sample. The circulator (C) is a device needed to separate incoming and outgoing radiation. Microwaves coming from port 1 can go to the cavity only through port 2 and cannot go directly to the detector. Only microwaves reflected by the cavity can pass through port 3 to the detector, that, therefore, will measure the changes in the amount of this reflected radiation.

The cavity (D) is used to amplify weak signals through resonance with microwaves. At the resonance frequency, ν_{res}, the microwaves are stored within the cavity, as no radiation escapes at this frequency. The efficiency of energy storage is quantified by the quality factor,

$$Q = \frac{\nu_{\text{res}}}{\Delta\nu}, \tag{4.1}$$

where $\Delta\nu$ is the full width at half maximum of the resonance curve. Inside the cavity, a standing wave is formed, with the electric and magnetic field components spatially separated. Since the unpaired electrons of the sample interact primarily with the magnetic field, the highest sensitivity and signal intensity are obtained when the sample is positioned at the magnetic field maximum. The cavity is designed to ensure optimal sample placement. The microwaves are coupled into the cavity through the *iris*, an opening whose size can be varied, controlling the fraction of microwaves that are either reflected back or injected into the cavity.

To have a detectable EPR signal, some microwaves must leave the cavity. When the sample absorbs the microwave energy, the coupling changes and the Q-factor is lowered because of the increased losses. The cavity is no longer coupled and the microwave can be reflected back to detector.

The detector (E) consists of a diode that converts the microwave power to an electrical current. Usually measurements are performed in a power range in which the diode current is proportional to the square root of the microwave power, that means the current is proportional to the voltage. To enhance the sensitivity of the spectrometer a lock-in amplifier scheme is used, by modulating the magnetic field at a known frequency. The output signal has an amplitude that is proportional to the slope of the EPR signal. Therefore the final spectrum is the first derivative of the absorption curve.

To perform temperature-dependent measurements, the sample was cooled using a helium gas flow cryostat, allowing temperatures as low as approximately 4K.

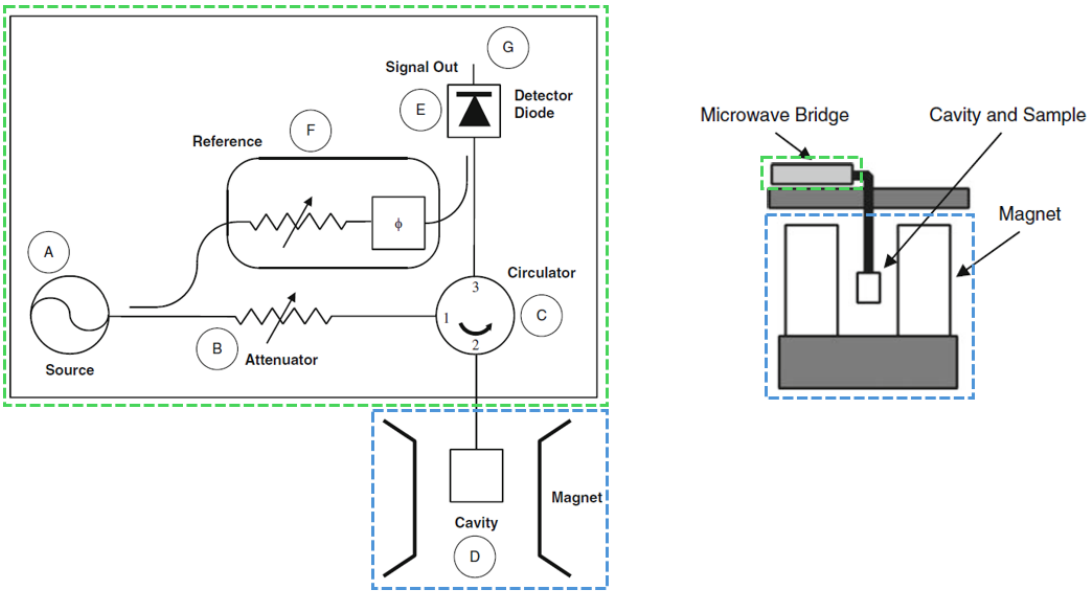

Figure 4.1: **EPR spectrometer scheme.** It is composed of three main parts: the microwave bridge, that contains the radiation source and the detection, the cavity with the sample, and the magnet, to apply a magnetic field to tune the electronic energy levels. [40]

4.2 Magnetic field dependence measurements

In superconductors, below the critical temperature T_C and below a critical magnetic field, the Meissner effect is present, that is the expulsion of the magnetic field.

In type-II superconductors, such as YBCO, the penetration depth is greater than the coherence length ($\lambda/\xi >> 1$)[41], for this reason the magnetic field can penetrate also below the critical temperature. High-temperature superconductors exhibit two critical magnetic field values: a larger one H_{C2} that breaks the superconducting order, allowing full penetration of the magnetic field, and a weaker one H_{C1}. The magnetic field can penetrate the sample in two main ways: (1) if the temperature is below T_C and the applied field is below the first critical field H_{C1}, the system is in the Meissner state, and the magnetic field can penetrate only to a small depth below the surface (penetration depth λ), which can vary considerably depending on the oxygen content of the YBCO sample, from a few hundred nanometres to a few micrometres; (2) at higher applied fields, but still below the second critical field H_{C2}, the system enters the mixed state, in which the magnetic field penetrates via quantized vortices [42].

The structure of these vortices is strongly influenced by the fact that YBCO belongs to the family of oxide superconductors, which are layered compounds in which the CuO planes, where the superconducting order resides, are separated by buffer layers acting as charge reservoirs. Their properties are anisotropic between the c axis and the ab planes; if the anisotropy is large, it is more appropriate to describe them in terms of weakly coupled superconducting layers, with the relevant criterion being the ratio between the coherence length along the c axis and the separation between the layers ξ_c/d [41]. YBCO is a good candidate for this discrete-layer description. In such layered superconductors, the structure of vortices and of the vortex lattice can be very different from the one in isotropic materials:

a "vortex line" along the c axis is not a straight object but is composed of multiple "pancake" vortices in the individual planes, connected to each other by Josephson vortices.

Not only can these vortices arrange themselves into a lattice, they can also interact with each other. In thick samples, where the size of the sample d is bigger than the penetration depth ($d >> \lambda$), the field associated with a vortex decays exponentially inside the superconductor, while in thin films ($d << \lambda$), it decays as $1/r^3$, where r is the the distance from the core vortex. Therefore, as the film thickness decreases, the vortex field distribution broadens, favouring field leakage outside the superconducting film [43].

In particular, in our setup, the superconductor sample is exposed to two different magnetic fields: a DC field and the microwave field. The static field produces vortices whose redistribution involves motion throughout the entire sample. The microwave field penetrates only within the skin layer near the surface and induces vortex oscillations around their equilibrium positions at pinning centers [44].

4.2.1 Superconducting signals

The initial measurements involved a magnetic field scans of the sample at fixed temperatures. The purpose of these preliminary measurements was to determine the appropriate value of the static magnetic field to be applied during the experiments described in the next section. This value will be set to 20 G, as we will demonstrate that is below the first critical field.

The measurements presented in this section, as well as in the following, are performed at a microwave frequency of about 9.56GHz, and an applied magnetic field that can run from ∼0G to 9000G. The applied field is oriented out-of-plane with respect to the sample.

At low temperatures, by varying the magnetic field, a peak in the signal can be observed corresponding to a specific magnetic field value, which we will identify as the first critical magnetic field H_{C1}, as shown in figure 4.2, in which we can see the intensity of the signal as function of the applied magnetic field. This signal is due to the penetration of magnetic field flux lines into the sample. In figure 4.2, it can be observed how the response differs depending on the initial conditions. In fact, if the sample is cooled in a zero magnetic field (ZFC) and then a magnetic field sweep is performed, we observe a critical field of approximately 450G. If the measurement is repeated immediately afterward, remaining at low temperature, the value of the critical field decreases to ∼40G. This is most likely due to the fact that the flux lines remain trapped, making them visible also at lower fields [39].

The peak visible at low magnetic fields decreases in amplitude as the temperature increases, until it vanishes, as shown in figure 4.3. We assume the sample to be in the normal phase at temperatures where the signal remains flat while sweeping the magnetic field. One might suppose that the presented measurements are very noisy; realistically, this is not the case. The noisy appearance is attributed to the presence of magnetic field vortices within the sample, which may arrange themselves in a lattice but can also move and interact with each other, altering the state of the sample that is probed by the microwaves.

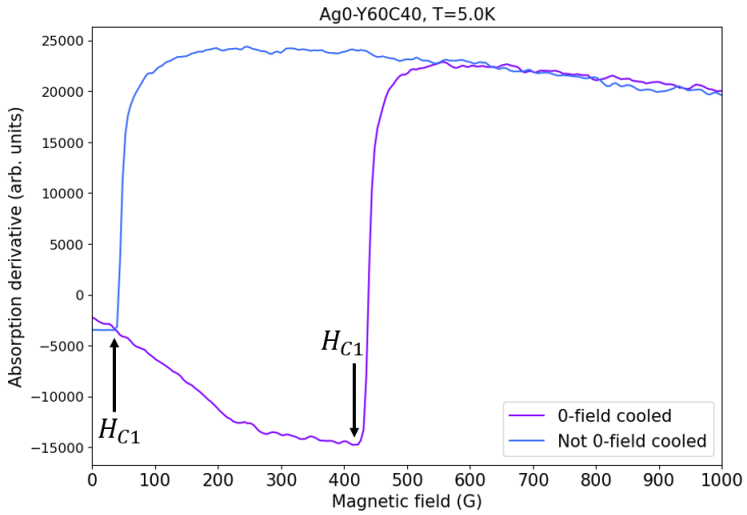

Figure 4.2: **Absorption derivative at low field of the sample Y60C40.** In both cases a significant change in the signal is observed at a certain value of the applied field. In violet the full magnetic sweep performed after zero field cooling (ZFC), in blue the full sweep done right after the first one. In the second case the change of signal happens at lower field with respect to ZFC. This is most likely due to the fact that vortexes can be trapped into the sample after the application of high magnetic field.

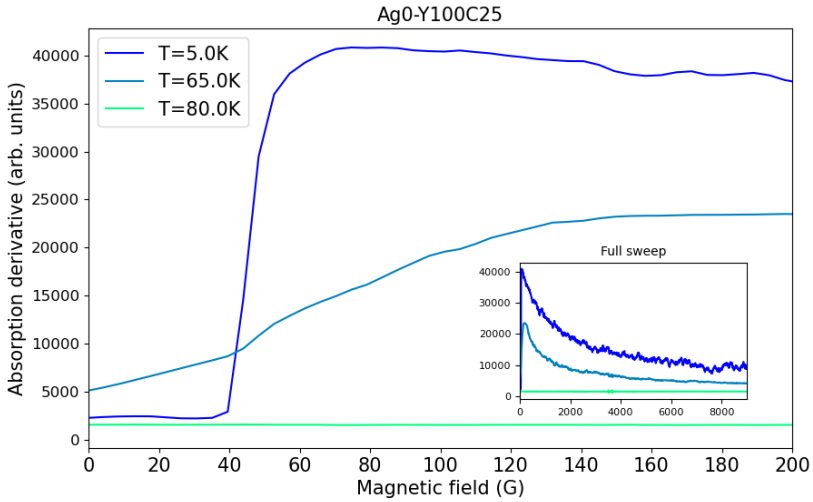

Figure 4.3: **Zoom of the microwave absorption derivative of the sample Y100C25.** In the inset the full magnetic sweep. A significant change in the signal can be seen at ∼40G, it is interpreted as a superconducting behaviour due to formation of vortexes. The maximum value of the signal is decreasing with temperature, suggesting that at 80K (green) the sample is not in the superconducting phase any more.

4.3 Determination of critical temperature by low field measurements

From the previous section, we have already observed that the absorption signal changes above and below a certain temperature. Our goal now is to perform a temperature scan in order to determine more precisely the critical temperature. To this end, we fixed the applied magnetic field at 20G, since this value is well below the first critical field, and recorded the sample response while the temperature was varied. Based on the previous observations, the temperature range was set between 5K and 80K.

As already observed, the superconducting signal changes depending on whether the measurement is performed before or after a full magnetic sweep. The reason is that after a complete sweep, vortices penetrate the sample and can be trapped in. For this reason, we performed the temperature scan in three different configurations, as shown in figure 4.4: (1) cooling in zero field (ZFC) and scan performed at 20G, (2) ZFC and scan at 0G, (3) one full sweep before the temperature scan performed at 20G.

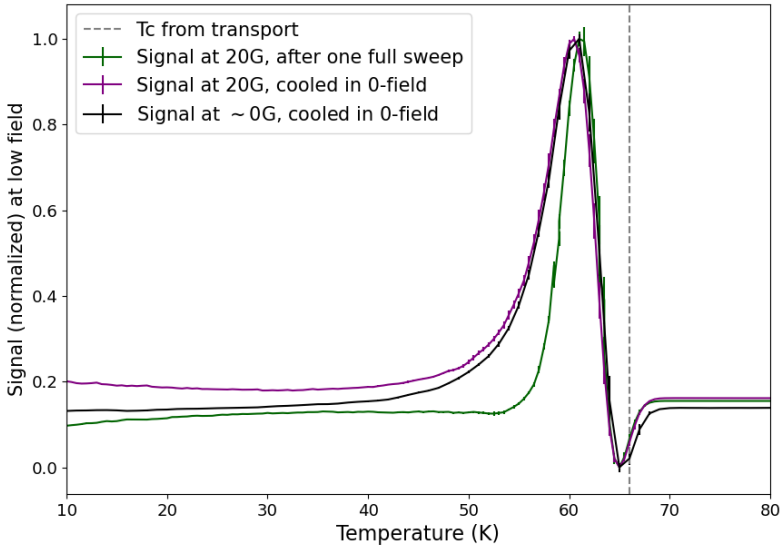

Figure 4.4: **Temperature scan at low field of the sample Ag0-Y60C40.** Microwave absorption derivative at low field, showing a significant change on the signal in a temperature range comparable to the critical temperature found with the transport measurement (dashed grey line). The scan was performed in three different configuration: at 20G after one full sweep of the magnetic field at 5K (green), at 20G cooling the sample in 0-field and without doing the full sweep (purple), at 0G cooling also in 0-field (black).

(1) The sample was first cooled in zero magnetic field[2]. Once 5K was reached, a magnetic field of 20G was applied, and a temperature scan was performed up to 80K. After the scan, the sample was heated up to room temperature in order to eliminate possible trapped magnetic flux vortices. (2) The sample was then cooled again in zero field, and once 5K was reached again, another temperature scan was performed, this time with the

[2]We must underline that in this experimental setup a true 0 field is not achievable.

applied magnetic field set to 0G. (3) Finally, the sample was cooled once more, and before starting the temperature scan (again with an applied magnetic field of 20G), a magnetic field sweep up to 9000G was performed, in order to intentionally introduce vortices into the sample.

There are no significant differences in the results of all these measurements: all of them reproduce a transition region peaked at 61K, consistent with the results of the transport measurement performed during the growth (figure 3.11). The first two configurations exhibit a similar transition region, indicating that the presence or absence of a small magnetic field does not significantly affect the results. The third configuration shows a narrower transition, suggesting an unexpectedly better estimation of the critical temperature range when vortices have penetrated the sample. This can be explained by assuming that vortices are most likely formed at defect sites, effectively 'isolating' them from the rest of the sample and allowing us to observe only the regions of the sample that have better quality.

The critical temperature can be set to 61K, that corresponds to the maximum of the microwave absorption signal, i.e. the temperature at which the microwave absorption undergoes the strongest variation, marking the transition of the sample from the superconducting to the normal state.

The same kind of characterization was performed also for the sample that is capped with a layer of amorphous CeO_2 (see figure 4.5). In general, the measurements appear to be noisier, possibly due to the presence of the amorphous layer, which may produce spurious magnetic signals. The shape of the transition in this sample is different from that of the previous one, making it more difficult to clearly identify a transition region. For this reason, a direct comparison between the two signals (with and without ZFC) can be helpful in locating the onset and extent of the transition. In the second configuration, the one after the full sweep, magnetic vortices may have penetrated the sample, resulting in a microwave absorption response that is distinct from the zero-field cooled case, where vortex formation is suppressed. As a result, the microwaves probe different internal states of the sample in the two conditions. The onset of the transition can be set at 51K, the temperature at which the two signals begin to overlap. This convergence suggests that the sample starts to behave similarly in both cases, pointing to the loss of superconducting order. The transition is considered complete when the signal stabilizes at higher temperatures, around 67K.

Considering these results, the temperature scans presented below will be always preceded by a full magnetic field sweep. This approach allows us to verify whether the sample is in the superconducting state before performing the temperature-dependent measurement, avoiding unnecessary heating and cooling cycles.

We will present the results in the following three sections: the first one regarding the open cavities, referring to samples that are not capped with silver. The second and third sections focus on closed cavities, distinguishing between heterostructures that terminate with CeO_2-Ag (symmetric cavities) and those capped only with silver (asymmetric cavities), where the second dielectric layer between YBCO and silver is missing.

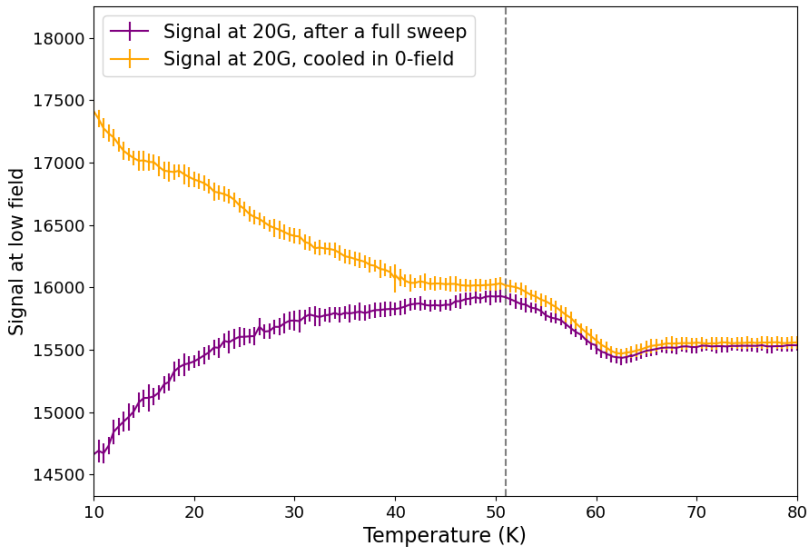

Figure 4.5: **Temperature scan at low field of the sample Ag0-C25Y60C25.** MWA derivative at low magnetic field, taken in two different conditions: after a full magnetic field sweep at 5 K (purple), and after zero-field cooling (orange). The grey dashed line at 51K marks the temperature where the two signals start to match, identifying the onset of the transition region.

4.3.1 Open cavity

We start presenting a temperature scan for all the samples not capped with silver, then focusing on the difference in the transition shape changing the thicknesses of the YBCO and CeO_2 layers, as presented in section 2.2.3.

In figure 4.6 all the measurements are presented. In order they are:

- the red curve represents the temperature scan of sample Y100C25, which shows a well-defined transition between 60K and 65K, consistent with what was found in transport measurements. In the case of sample Y100C25, a noisier signal is observed at low temperatures, unlike the other samples, which exhibit a flat response;

- the green (Y60C40) and the purple (Y60C5) curves display a well-defined transitions within a similar temperature range, remaining in good agreement with transport data. For sample Y60C5, the critical temperature appears slightly lower; this is likely due to the YBCO layer, that, because of possible small variations in growth parameters, might have a slightly different thickness than reported or a different oxygen content. The small bump seen in the purple curve is to attribute to a minor silver contamination on one edge of the sample. It can be ignored for the purposes of the current analysis;

- the yellow curve (Y60C120) shows a broader transition. In this case, the increased noise at low temperatures is likely due to the higher amount of CeO_2. This difference in the transition width can be also better seen in figure 4.7b, which provides a zoomed-

in view of the transition region. The signals have been shifted along the temperature axis to align their peaks, allowing for a clearer comparison of their shapes;

- the black curve (Y30C55) shows a similar transition, flatter than the other and noiser at lower temperatures. This behaviour could suggest that the ratio between the thickness of YBCO and CeO_2 layers is important to well define the range in which the heterostructures presents a superconducting behaviour. In fact, in these two last samples the ratio YBCO/CeO_2 is very similar, equal to 1/2. In all other sample this ratio is bigger than 1, probably suggesting that the layer of YBCO has to be thicker with respect of the CeO_2 layer;

- the blue curve (C25Y60C25) represents the only sample in which the YBCO layer is capped. The shape of the transition is significantly different in this case, and is strongly dependent on the magnetic field history, as we have already seen.

The critical temperature found for the uncapped samples is defined as the temperature at which the MWA signal is maximum or at which the ZFC and non-ZFC signal starts to match, as explain above. They are summarized in table 4.1.

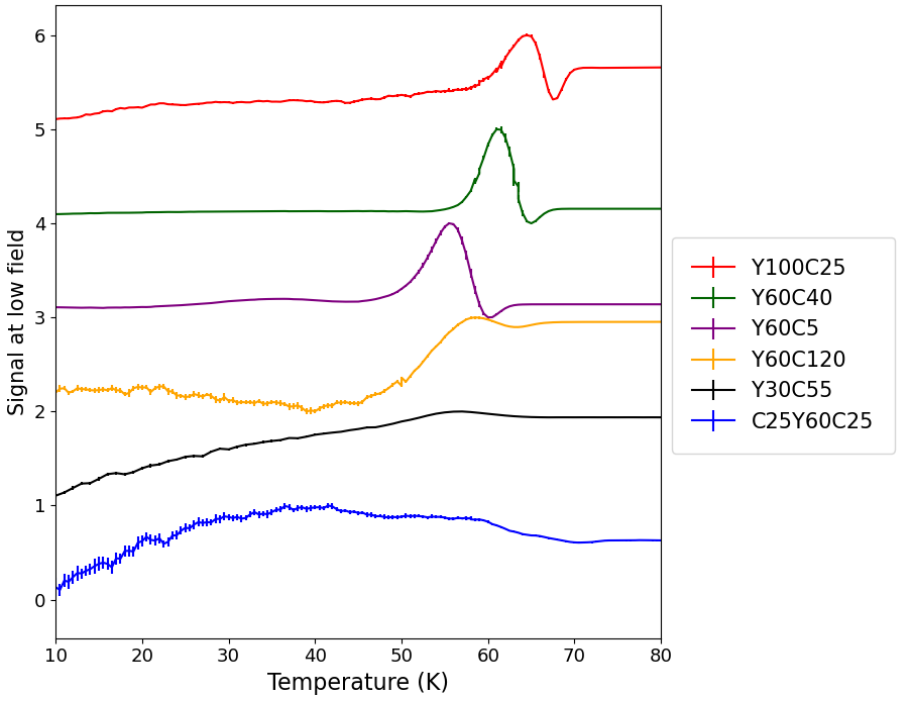

Figure 4.6: **Temperature scan at low field for all samples without silver layer on top.** In order, sample Y100C25 (red), Y60C40 (green), Y60C5 (purple), Y60C120 (yellow), Y30C55 (black) and C25YY60C25 (blue).

Table 4.1: **Critical temperature T_c from MWA measurements.** Only samples without the silver top layer. T_c is estimated as the temperature at which the MWA signal is maximum, except for C25Y60C25, where it is estimated by comparing the ZFC non-ZFC cases.

Sample	T_c (K)
Y100C25	64.5
Y60C120	59.0
Y60C40	61.0
Y60C5	55.5
Y30C55	58.0
C25Y60C25	51.0

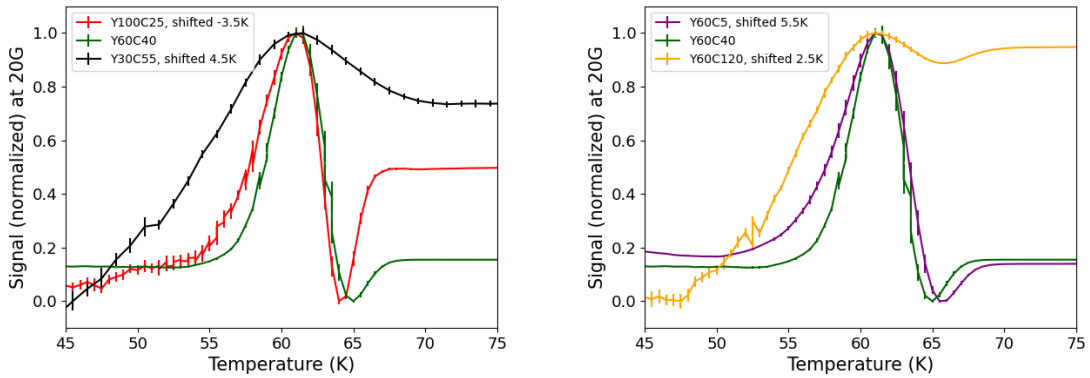

(a) (b)

Figure 4.7: **Zoomed temperature scan normalized in the transition range 45-75K.** Data are shifted to make the peaks of the signal match, this difference between samples is most likely due to the different YBCO thickness. **(a) YBCO thickness dependence:** the shape of the transition is similar if we compare 100nm and 60nm of YBCO, if we look at 30nm the transition becomes wider. **(b) CeO_2 dependence:** changing the thickness of CeO_2 layer between 40nm and 5nm does not affect the shape of the transition, with 120nm it becomes wider.

4.3.2 Asymmetric closed cavity

Now that we have demonstrated that the technique is consistent with transport measurement for identifying the superconducting transition in the uncapped samples, we can proceed with the analysis of the samples in which the YBCO layer was capped with 5, 10, or 15 nm of silver, which works as the second and final mirror for the heterostructures. Because the silver is in direct contact with the YBCO, these samples are referred to as asymmetric cavities. All samples with the different silver thicknesses were analysed following the same protocol described above: the magnetic field was fixed at 20G and a temperature scan was performed from 5K to 80K. Below we present results for two representative sample sets that summarize the general trends observed across the whole series.

In figure 4.8a the set regarding sample Y100C25 is presented. We can observe that the

scan for the sample without silver exhibits a transition at higher temperatures, within a range consistent with the critical temperature determined from transport measurements (indicated in the graph by a vertical dashed line). Upon adding the silver layer, the entire transition shifts progressively towards lower temperatures as the silver thickness increases. The transition maintains the same shape, characterized by a more intense "positive" peak followed by a less pronounced "negative" one; even in the case of the sample with only 5 nm of silver, this second peak is still present, as can be seen in 4.8b.

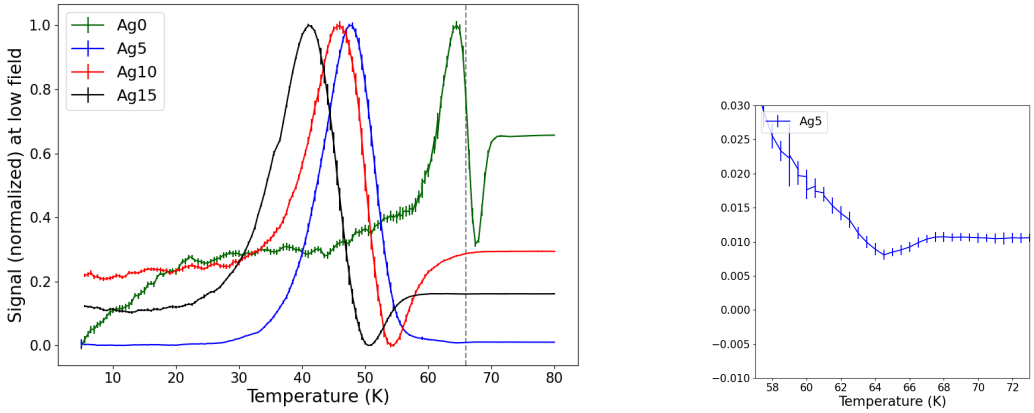

(a) (b)

Figure 4.8: **Temperature scan of the sample Y100C25**: (a) Temperature scan for the uncapped sample (green) and samples capped with silver (blue, red, black in order of thickness of silver). We can see that there is a shift to lower temperatures as we increased the thickness of the silver layer. (b) A zoom-in view if the "negative" peak of the sample Ag5-Y100C25.

A more interesting result was observed for the Y60C5 sample (figure 4.9a), where a non-monotonic trend of the transition shift with silver thickness is evident. In particular, the sample with the largest silver thickness (15 nm) shows a smaller shift compared to the other two cases. Also the shape of the transition is changing, becoming wider and less defined. The small negative peak is still present for the sample capped with 5nm of silver (figure 4.9b). A possible explanation for this peak, which in this case also appears at higher temperatures compared to the main peak, could lie in a structural inhomogeneity of the sample, resulting in domains characterized by higher critical temperatures and others with lower ones. It is possible that a region with a higher T_C, even if spatially limited compared to the rest of the sample, has "persisted", leading to an anomaly in the microwave absorption at higher temperatures.

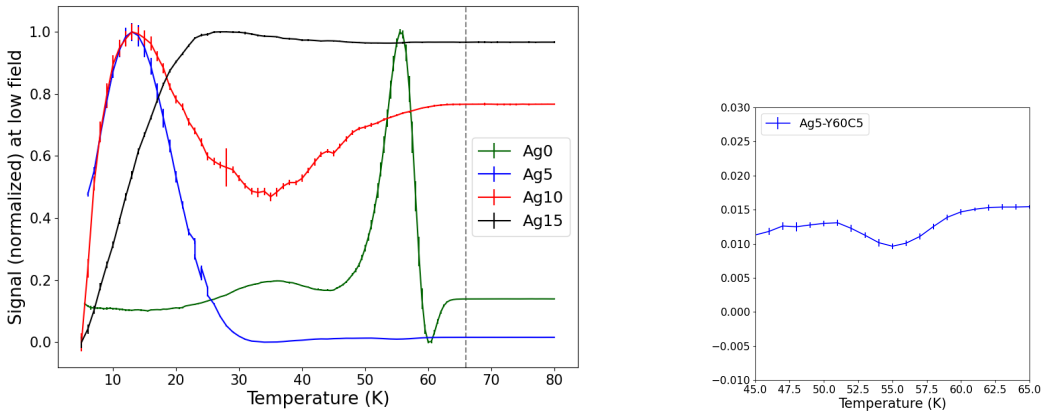

(a) (b)

Figure 4.9: **Temperature scan of the sample Y60C5**: (a) Temperature scan for the uncapped sample (green) and samples capped with silver (blue, red, black in order of thickness of silver). This is the only set of samples that presents a non-monotonic behaviour in the temperature shift as the silver layer thickness increases. (b) A zoom-in view if the "negative" peak of the sample Ag5-Y60C5.

4.3.3 Symmetric closed cavity

While the results from the previous section might initially suggest that the reduction of the critical temperature could be attributed to proximity effects at the metal–superconductor interface formed when YBCO is directly capped with silver, this interpretation must be reconsidered examining the data obtained from samples containing also the amorphous CeO_2 layer, where no direct silver–YBCO interface is present. In particular, these structures realize a *symmetric cavity*, meaning that the YBCO layer is placed between two CeO_2 layers, which are enclosed by two metallic layers (LNO and silver). Not only the shift of the transition toward lower temperatures is still observed after the deposition of silver, but the superconducting behaviour is also suppressed when the silver thickness is bigger than 5nm.

As shown in figure 4.10, the only sample exhibiting superconducting behaviour, is the one with 5nm of silver. For the other two silver thicknesses, the peaked signal at small magnetic field is not present, suggesting no superconducting order for these samples. Furthermore, the recorded signal is similar to the one measured at room temperature, suggesting no change of state varying temperature. Therefore, the temperature scan was performed only for the first sample (figure 4.11). Again the shape of the transition is similar to the uncapped sample, but shifted to lower temperatures. This would suggest that this change in the superconducting behaviour of all these sample is due to cavity itself, similarly to what observed in ref. [18].

However, we have observed some degradation processes for all the capped samples, this suggest that covering the YBCO layer with something non-monocrystalline, such as both silver and CeO_2, might be an issue. For further analysis in this regard, see chapter 5.

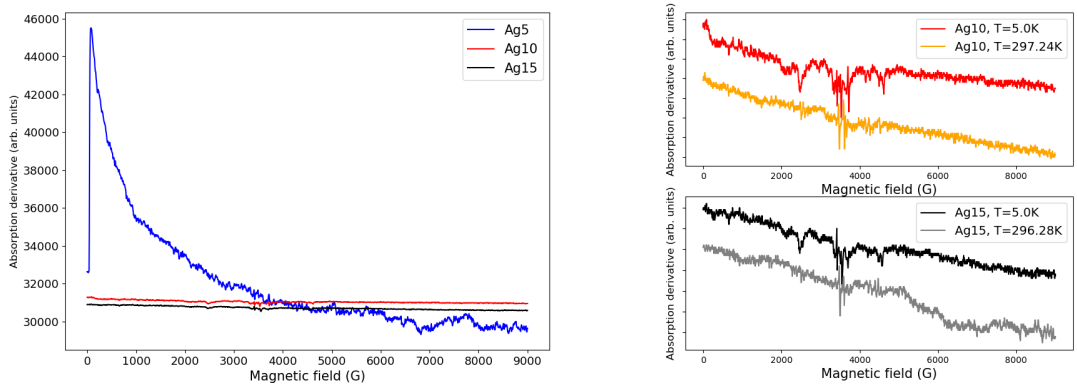

(a) (b)

Figure 4.10: **Full sweep of the C25Y60C25 sample**. (a) At 5K only the one capped with 5nm of silver (blue) presents a superconducting signal. (b) A comparison between the magnetic sweep at 5K and room temperature for sample with 10 and 15nm of silver, showing a very similar signal, confirming the absence of superconducting order for those two sample at low temperature.

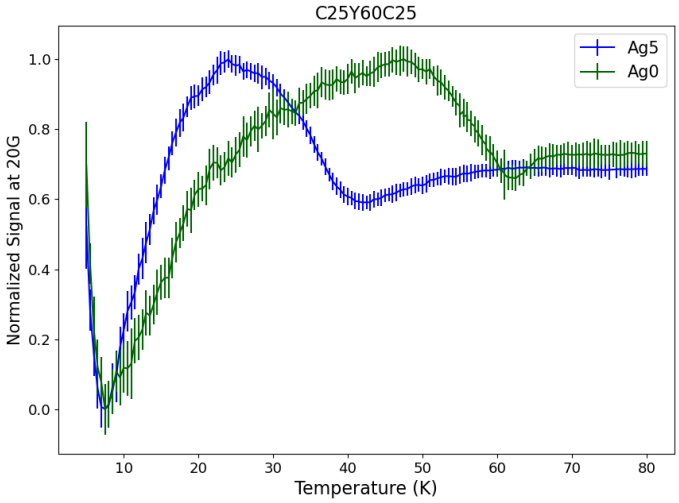

Figure 4.11: **Temperature scan of the sample without silver and with 5nm**: We can see there is a shift of the signal towards lower temperatures even if the silver is not touching directly the YBCO layer.

Chapter 5

Reproducibility analysis

As already mentioned in the previous chapter, a degradation process was observed during the MWA measurements. This effect was evident in all capped samples, both with silver and with CeO_2. While for those samples that end with YBCO layer, no such degradation was observed, as can be seen in figure 5.1, in which the temperature scan for sample Ag0-Y60C5 was repeated after about three weeks under the same magnetic field configuration. Furthermore, measurements shown in figure 4.4 were taken in different periods, and also results from optical measurements confirm that uncapped samples are not degrading. This suggests that the degradation problem is entirely due to the layer on top of the YBCO, and not to the bottom layers.

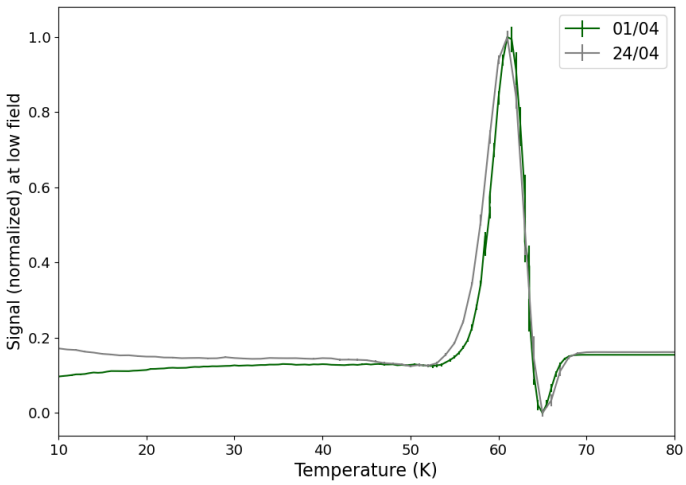

Figure 5.1: **Temperature scans of sample Ag0-Y60C40 taken three weeks apart:** the two signals match almost perfectly, with a maximum shift of about 0.5K, which can be attributed to experimental errors.

Different explanations for this degradation process are possible: from oxidation of silver to oxygen content exchange between the silver and the YBCO layers. Another possible explanation could be that the presence of an amorphous layer in direct contact with the YBCO layer affects the structure of the superconducting layer, leading to micro-fractures that compromise the superconducting properties of the entire heterostructure. In the

following, we will investigate this degradation process, differentiating the analysis for the two interfaces.

We underline also the fact that MWA measurements were performed starting about ten days after the deposition of the silver layers. Being aware of this, we must suppose that all the "first" MWA measurements were already affected by the degradation process. In order to understand if this behaviour is a direct consequence of the silver deposition or it is only visible after some times, we performed another study. We capped one sample that terminates with YBCO layer, with only one small strip of silver, in order to be able to do transport measurement by making the electrical contact in the free space. The results will be presented in the final section of this chapter.

5.1 Samples degradation

In order to analyse the degradation process, two sets of samples will be considered: the first will consist of samples with 15nm of silver directly on top of the YBCO layer, Y100C25 and Y60C5, and the second will consist of samples C25Y60C25 with and without the silver layer, in order to study also the effect of the interface amorphous CeO_2-YBCO.

5.1.1 Silver-YBCO interface

Starting from sample Ag15-Y100C25, we observed an overall shift towards lower temperatures of about 13K over a period of nearly three weeks. As shown in figure 5.2, repeating the measurement reveals that the transition region shifts to lower temperatures. Between the first and second measurement, we observed a shift of 5K at the maximum and 3K at the onset; between the second and third measurement, the shift was 8K at the maximum and 6K at the onset. This suggests that, in addition to a shift, a broadening of the transition is also present.

This observed broadening is more visible in sample Ag15-Y60C5, figure 5.3, in which there is a shift of 10K if we look at the maximum, but only 1K considering the onset. In the other samples analysed, the broadening was more limited, similar to the previous sample. This is the only sample in which the phenomenon appears so pronounced, possibly suggesting greater "resistance" to the onset of superconducting behaviour.

There are several possible explanations of this degradation process. In the following we will try to delve into each of them to understand which one is more likely: (1) silver is oxidizing, (2) there is an oxygen content exchange between the silver and YBCO layer, (3) oxygen is diffusing into the YBCO or (4) sample is cracking due to non-monocrystalline layer touching the epitaxial YBCO layer.

(1) If silver is oxidizing, as most likely it is happening, we would expect that only the surface of the silver layer is affected, not modifying the interface silver-YBCO. For this reason it is reasonable to hypothesize that thicker silver layer would be better for our heterostructures, as the oxide layer would be more distance from the YBCO. This would be supported from the results for Y60C5 sample shown in figure 4.9a, in which the sample with 15nm of silver shows a higher critical temperature. However, this is visible only in that sample, not in others, suggesting that most likely the oxidation of the silver is not the main issue, at least.

(2) The oxygen exchange between silver and YBCO could well explain why the critical temperature changed, as the superconducting behaviour of YBCO is strongly dependent

on the oxygen content. However it is not clear why this would be time-dependent, so at a first analysis also this hypothesis has to be disregarded.

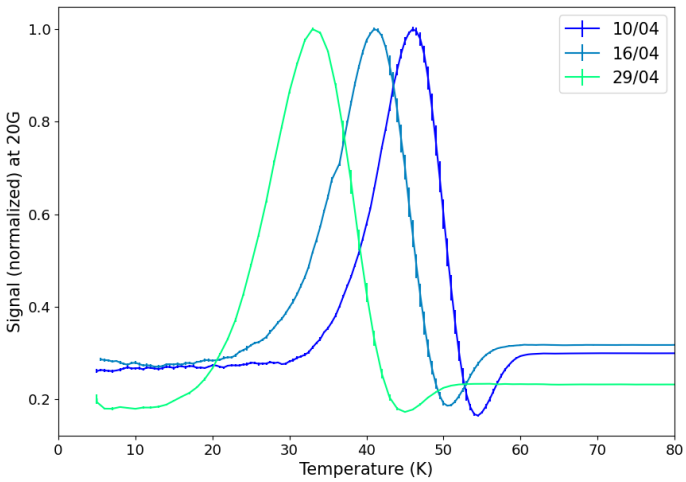

Figure 5.2: **Degradation process of sample Ag15-Y100C25**: we can see a shift to lower temperature of the signal repeating the measurement.

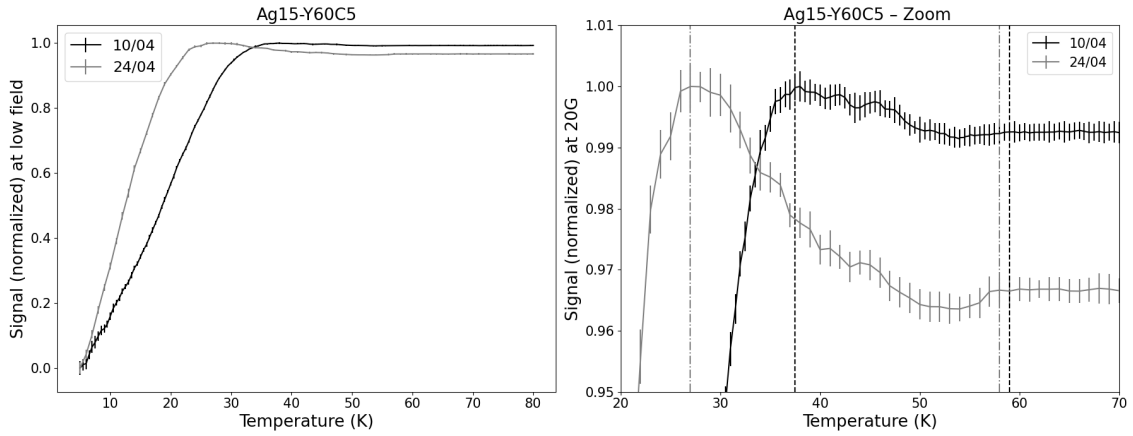

Figure 5.3: **Degradation process of sample Ag15-Y60C5**: In this sample, we can see that the maximum peak is shifted towards lower temperatures, different is for the minimum or for the point in which the signal becomes constant, these points seems to not shift, resulting not in a rigid shift, but in a broadening of the transition.

(3) Since during the silver deposition adhesion layers such as chromium or titanium were not used to minimize contaminations, a silver diffusion could be proposed. Silver diffusion into YBCO has been observed at hundreds of Celsius, like in ref. [45], but it seems unlikely that in our case silver can diffuse into the YBCO considering that heterostructures were never heated up above the room temperature.

(4) Below the YBCO layer, as described in chapter 3, all the layers starting from the substrate have similar lattice parameters to minimize deformations and strains due to

lattice mismatches. Silver layer, as well as the CeO_2 top layer, is amorphous, and it most likely leads to strain between the multi-crystalline layer and the YBCO layer. During heating and cooling cycles, expansions and contractions of the different layers are possible, and if the lattice match is not optimal cracks could occur. This would appear as the most likely explanation, nevertheless also this interpretation of the problem has some criticalities. We performed two temperature analysis on sample Ag15-Y30C55 (figure 5.4), separated by one day and did two different temperature cycles. The resulting scan match, showing no significant differences. If the degradation were caused by cracks due to thermal cycling, we would expect to observe the shift of the transition towards lower temperatures even after very short time intervals, if a temperature cycle had occurred in between.

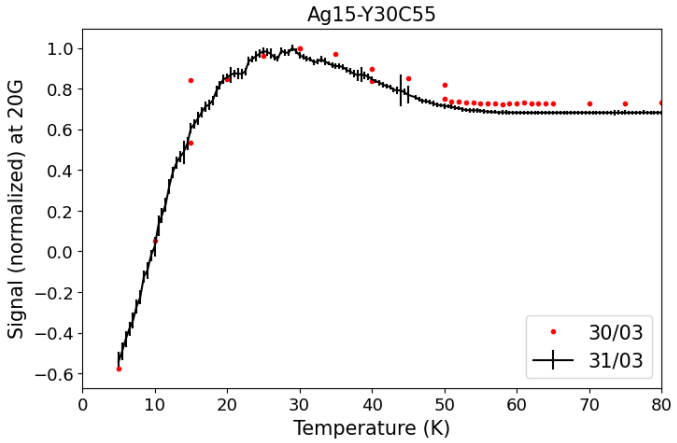

Figure 5.4: **Reproducibility analysis of sample Ag15-Y30C55.** The black curve shows a temperature scan at a fixed magnetic field of 20 G, while the red curve represents the low-field signal extrapolated from a series of full sweeps performed at different temperatures. The two measurements were carried out one day apart.

As we have seen, we have plenty of hypotheses, but none is completely satisfactory. In order to further deepen our comprehension regarding this topic, in the next future some more characterizations are possible: such as trying to change the metal top layer with, for example, aluminium or gold to understand if the oxidation is actually an issue. Or also perform transmission electron microscopy (TEM) characterization to study the possible silver diffusion.

5.1.2 CeO_2-YBCO interface

Regarding sample C25Y60C25, we will present the degradation process for both samples with and without the silver layer.

Starting from Ag0-sample, in figure 5.5 it is visible that the signal is changing repeating the measurement. However, the shift towards lower temperatures is less pronounced with respect to the sample previously presented. Between the first and second temperature scan, the onset critical temperature is shifted by about 3K, while after the third measurement it seems to be the same as the previous one. For this sample, the shape of the transition is changing a lot after each measurement. As we can see from the plot, the third (darker) scan shows multiple peaks, each of which could correspond to the critical temperature of a different part of the sample. This can be rationalized by assuming the

presence of different YBCO domains, some with higher critical temperatures, others with poorer superconducting properties, some more spatially extended than others. With MWA measurements, we probe the entire sample, so the obtained response reflects contributions from all these different regions. Therefore, the arising of multiple peaks suggests that the sample is becoming increasingly inhomogeneous.

Considering now the sample with 5nm of silver on top of the CeO_2 layers, we observed an increase in the noise after the second measurement (figure 5.6a, light blue). The reduction of the signal intensity is also visible in the full sweep data in figure 5.6b, in which the peak at low magnetic field is weaker by a factor of ten with respect to the data taken ten days before.

For this sample as well, considerations similar to those already made for the one with silver directly on top of the YBCO can be done, such as a possible oxygen exchange between the layers or cracking due to temperature cycles. As before, it is difficult to disregard some factors over others and to identify a single cause as more plausible than the others.

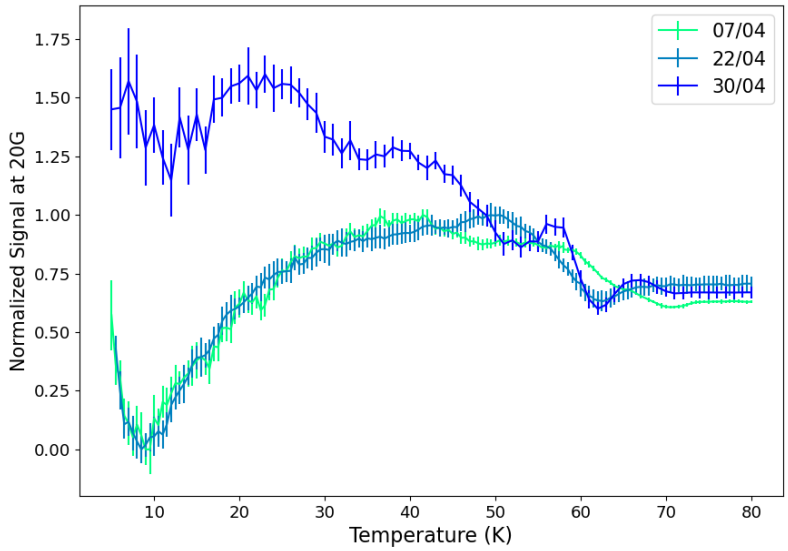

Figure 5.5: **Degradation process of sample Ag0-C25Y60C25**: After the first measurement, also in this case a shift of the transition is visible. After other 8 days, the shape is different with plenty of peaks, each of them could represent a "different critical temperature", suggesting that the sample is becoming more and more inhomogeneous. (Data are vertically shifted to make the onsets match.)

5.2 Transport measurement in a partially silver-capped heterostructure

Since in capped samples it is not possible to perform transport measurements, and the MWA measurements were not carried out immediately after the deposition of the silver layer, it is not clear whether the deposition of silver has an immediate effect on the superconducting critical temperature of the heterostructures, or whether the observed decrease

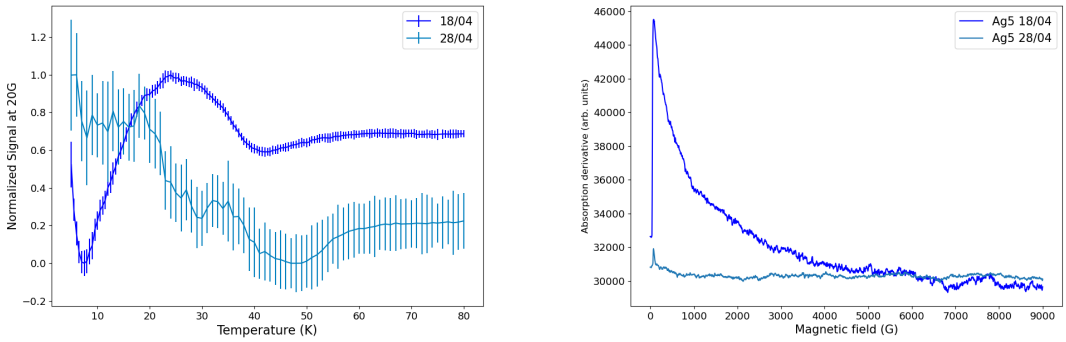

(a) (b)

Figure 5.6: **Degradation process of sample Ag5-C25Y60C25.** (a) Looking at the temperature scan, after about 10 days, the main difference is that the signal became less intense. (b) Also from the magnetic full sweep it is clear that the magnitude of the peak at low field is reduced.

in T_c is solely due to structural degradation over time. To address this question, we partially covered one sample with silver, leaving an uncovered region where electrical contacts could be made with indium, as schematized in figure 5.7. In this way, transport measurements could be repeated immediately after silver deposition, allowing us to investigate whether T_c decreases as soon as the silver layer is deposited.

In the test sample, consisting of a 100 nm YBCO layer, a silver strip covering approximately 1/10 of the YBCO surface was deposited. The remaining exposed area was used to place the four indium contacts for transport measurements. In the transport measurement, two of the four probes are used to apply current, the other two for reading the voltage. For this sample two possible configurations to perform the measurements can be chosen: the current and the voltage can be applied and read perpendicular to the silver strip (A-C and B-D) or parallel to the silver strip (A-B and C-D). In order to be sure that the measurement is not configuration-dependent, we performed the transport in both configuration, not observing significant differences. Instead, the main issue of this kind of measurement is the good quality of the electric and thermal contacts, which in some cases made the results not reliable.

The sample used for this study is the same one employed for the characterization of the heterostructures during the deposition process (Y100C25, transport measurement already shown in figure 3.10). Before depositing the silver strip, we repeated the transport measurement, observing a shift of about 8K towards lower temperatures (as shown in figure 5.8, blue and orange curves). Moreover, the shape is also different, displaying a double peak, which is reminiscent of a two-probe measurement, thus suggesting not optimal contact quality. In any case, this shift is most likely due to scratches introduced while making the indium contacts, rather than to a proper degradation process, as we have already shown that such behaviour is characteristic only of the capped sample.

We repeated the transport measurement immediately after the deposition of the silver strip, as well as one week and three weeks later. In figure 5.8, we plotted only the data taken three weeks later, since the other two sets are not entirely reliable, most likely due to contact issues. Considering the green curve (three weeks later), we observe that

the transition is not shifted, as indicated by the derivative that is peaked at the same temperature. This suggests that, at least at this level of YBCO surface coverage, the silver is not sufficient to degrade the sample. On the other hand, the transition appears broader, in agreement with the MWA observations, confirming that one effect of silver capping is to cause a broadening of the transition.

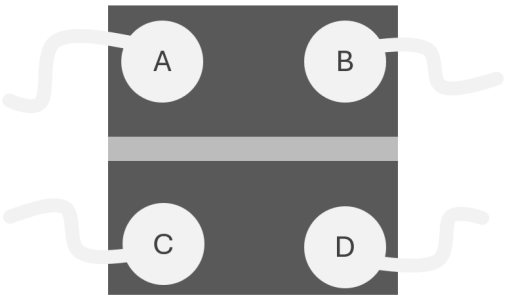

Figure 5.7: **Scheme of the sample preparation for transport measurement performed in the 4-probe configuration.** The contacts were positioned above and below the silver strip. The transport was carried out in two possible cases: with the current applied vertically (e.g. A-C) as the reading of the voltage (B-D) and horizontally (A-B for the current, C-D for the voltage).

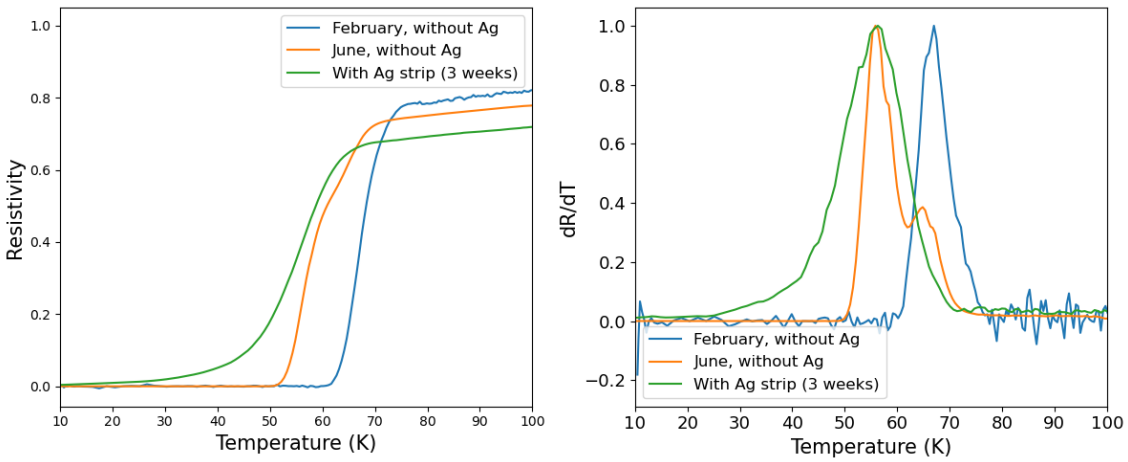

Figure 5.8: **Transport measurement and its derivative for the sample with and without the silver strip.** A shift of about 10 K is visible between the measurement performed right after the growth of the heterostructure (blue) and before the deposition of the silver strip (orange). Three weeks after the deposition of the silver strip the transition becomes broadened (green), as can be seen in the derivative plot on the right. (Data are normalized)

Chapter 6

Optical measurements

Through the measurements presented in the previous chapters, we were able to characterize the structure of our samples and how their superconducting behaviour is modified by the cavity environment at the equilibrium.

In this chapter we will present a preliminary study on the dynamical properties of the samples. In particular, our focus is on the relaxation dynamics of the YBCO layer in the visible range when it is driven out of equilibrium by intense ultrashort laser pulses. The aim of these measurements is to probe the charge-transfer transition of YBCO, which plays a central role in the physics of high-temperature superconductivity and is closely connected to the evolution of the superconducting gap.

The superconducting gap is directly related to the density of excitations in the system. The photo-injection of free quasi-particles by means of femtosecond laser pulses introduces a time-dependent non-linear perturbation of the gap. By monitoring how this perturbation relaxes back to equilibrium, valuable information on the underlying electronic and superconducting properties can be obtained. In particular, studying the transient reflectivity in the visible range provides a direct optical probe of the superconducting state of the sample.

This will be achieved using time-resolved optical techniques. Unlike a standard pump-probe experiment, in which the sample is excited by a single intense pulse (pump), in our case the sample will be excited by two pump pulses (one in the visible range and the other in the mid-infrared range). The subsequent dynamical response will be measured by a weaker pulse (probe) in the visible range.

In the following, we will describe the technique and the experimental setup, and then focus on the obtained results. In particular, we will highlight how the heterostructures can be resonantly driven through the charge-transfer excitation, thereby providing insights into the interplay between optical excitation and superconductivity.

6.1 Three-pulse spectroscopy

In conventional Bardeen–Cooper–Schrieffer (BCS) superconductors, the opening of the superconducting gap causes a rearrangement of the quasiparticle excitation spectrum only within an energy range comparable to $2\Delta_{SC}$. In cuprate high-T_C superconductors, by contrast, this spectral weight redistribution extends to energies up to two orders of magnitude larger than $2\Delta_{SC}$ [21, 46]. This remarkable behaviour implies a direct involvement of high-energy electronic excitations in the pairing mechanism responsible for high-temperature superconductivity.

In BCS systems, the superconducting gap has an isotropic s-wave symmetry, naturally arising from phonon-mediated pairing. In cuprates the gap exhibits a d-wave symmetry, characterized by nodal directions (where the gap amplitude vanishes) and antinodal directions (where the gap is maximal). When cuprates are photoexcited by ultrafast laser pulses, quasiparticles are injected into the system, perturbing the initial equilibrium distribution and leading to a non-linear perturbation of the gap.

Three-pulse spectroscopy has proven to be a powerful tool for investigating the superconducting phase in other cuprates, such as Y-Bi2212 [21]. In this scheme, the system is driven out of equilibrium by two pump pulses, and its relaxation is measured by probe pulses. The first pump pulse changes the quasiparticle distribution across the Brillouin zone, while the second pump measures the broadband transient response of the photoinduced nonthermal state.

A crucial feature of this approach is that the differential signal, defined as the difference between the double pump response and the sum of the two single-pump responses, vanishes above T_C. This makes the non-linear optical response a fingerprint of superconductivity: it directly relies on the presence of the condensate and disappears when the superconducting gap closes. The temperature dependence of the transient spectral weight in the visible range shows a sharp discontinuity at T_C, supporting the reliability of this technique to probe the superconducting transition.

Moreover, as shown in Fig. S12 of Ref. [47], when the delay between the two pumps is increased, the differential signal decays exponentially and disappears. If the delay is too long, the second pump arrives after the system has already relaxed back to equilibrium. For this reason, in our analysis we will focus only on the configuration in which the two pump pulses are synchronous.

6.1.1 Experimental setup

The setup is schematically shown in figure 6.1, in the following we will briefly describe the three optical paths of the three different pulses involved in the measurement: the MIR pump, the blue pump and the white probe. All systems are driven by a Pharos Laser, which provides 400µJ pulses with a photon energy of 1.2 eV, a pulse duration of 290fs and a repetition rate up to 50kHz. 40µJ/pp are used to pump the Non-Collinear Optical Parametric Amplifier (NOPA), the remaining 360µJ to pump the Twin Optical Parametric Amplifier (OPA).

Focusing on the NOPA, its output is tunable in the range 650-900nm and delivers pulses shorter than 25fs. It is then split by a 70/30 beam splitter (BS); most of the power is used to pump the sample, the remaining part is used to generate the white light probe. To pump the system, the NOPA beam is focused on a type I β-Barium Borate (BBO) crystal, enabling higher photon energies to be achieved through Second Harmonic Generation (SHG). In our case, the NOPA is tuned at 800nm, meaning that after SHG we obtained a blue beam at 400nm. After collimation, a bandpass filter (F2, 350-700nm) filters out the remaining near-IR radiation; then the blue beam is focused on the sample. In order to obtain the supercontinuum white light probe (500-800nm), the NOPA beam is focused on sapphire (Al_2O_3) crystal. A shortpass filter (F1, edge at 800nm) is placed after the generation to filter out the near-IR light. Then, a beam splitter splits the white light: the reflected beam goes to the reference channel, while the transmitted beam is focused on the sample using an achromatic doublet to avoid chromatic aberrations. The MIR pump is obtained through Difference Frequency Generation (DFG) in GaSe crystal

by mixing the outputs of the Twin OPAs, it is tunable from 5µm to 20µm, we will tune it at 11µm. Then, the beam is focused on the sample through a silver spherical mirror. These three pulses arrive on the sample with a non-collinear geometry: the probe beam impinges almost normally, the blue pump arrives with an angle of ∼10° with the probe, and the mid-IR pump with an angle of ∼20°.

The time delay between the three beams is controlled through two translation stages: the first one (TS1) is placed between the NOPA output and the first beam splitter, so it tunes the delay between the pumps without modifying the delay between the blue pump and the white light probe; the second translation stage (TS2) is placed after the generation of the white light, therefore it modifies only the path of the probe. For each given position of TS1, a full scan of TS2 is performed, i.e. for each pump-pump delay a full probe scan is measured.

Along the optical paths of the two pumps, two choppers are positioned: the first one (Ch1) runs at 90Hz and it blocks the visible pump beam, the second one (Ch2) runs at 45Hz and it blocks the MIR pump beam. Their rotations are synchronized as they are controlled by the same square wave generator. Thus, there are four different configurations for each probe beams, as shown in figure 6.2: the probe beam could arrive with both pumps, with only one or without pumps. In order to distinguish these configurations, two single-photodiode detectors are placed to intercept a back-reflection or a residual transmission of the pump beams. Their signals are digitized and they provide a tool to assign a proper label to each probe pulse.

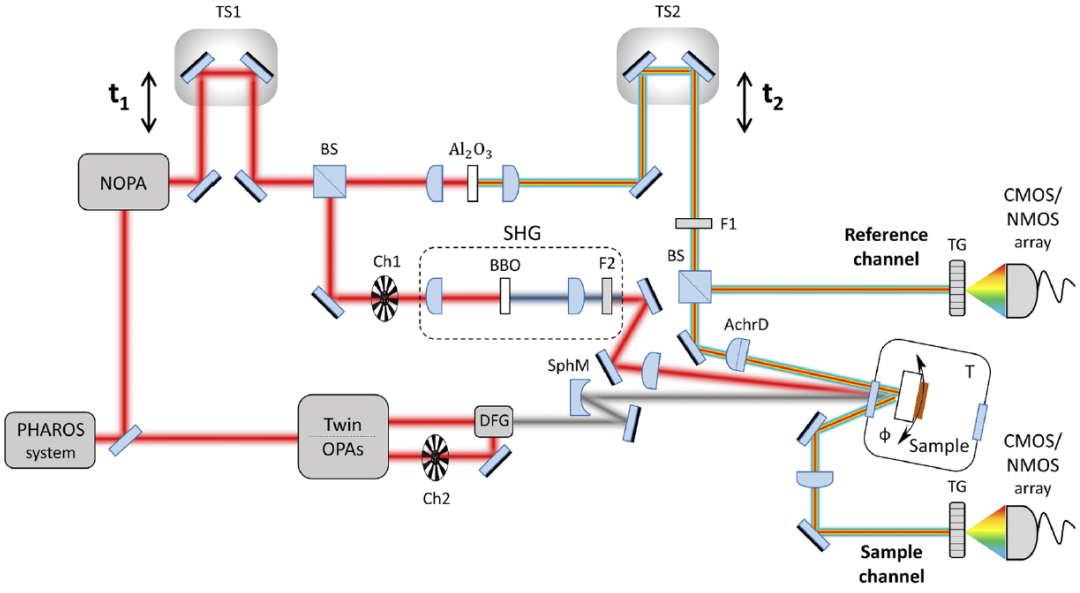

Figure 6.1: **Experimental setup scheme.** [48]

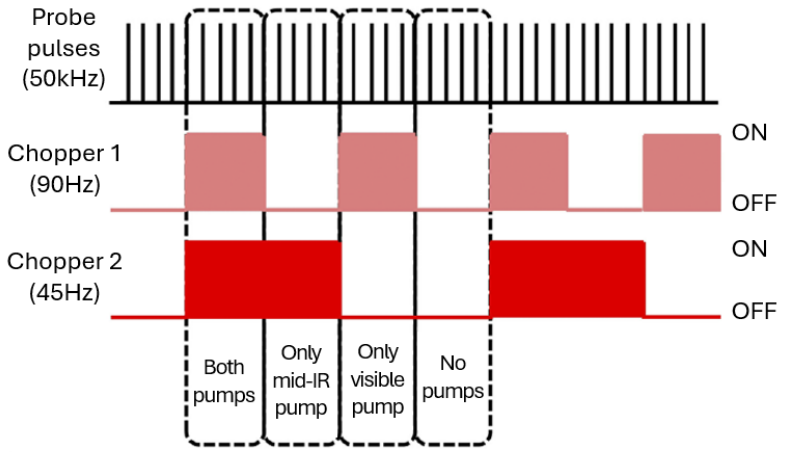

Figure 6.2: **Chopper functioning scheme.** Adapted from[48]

The sample is mounted on a closed cycle liquid helium cryostat. The sample holder is a copper plate directly connected to the cold head of the cryostat. The temperature of the sample is measured through a diode sensor placed on the copper plate, in the proximity of the sample. It is possible to achieve temperatures as low as 10K, since the sample is placed directly on the copper plate, very close to the cold head. The sample is enclosed in a vacuum chamber, that presents a polycrystalline diamond window in each chamber's face, in order to allow optical access both for transmissivity and reflectivity measurements. The vacuum system allows to reach pressure as low as 10^{-7}mbar at room temperature, 10^{-8}mbar at cryogenic temperature.

The reflected probe beam is collimated by a lens and routed to the acquisition system, which consists of a transmission blazed grating (TG), after which the beam is focused on the detector, a negative channel metal oxide semiconductor (NMOS) linear image sensor, with 128 pixels. The detector can run up to 5kHz, and it is synchronized with the repetition rate of the laser. A wavelength calibration of the arrays is performed every time there is an adjustment of the optical path, to do so, we have used a coloured filter that has distinctive transmittivity features across the white light bandwidth.

6.2 Measurements

We did not investigate all the samples listed in the previous chapters, we selected only two sets: Y60C5 with all silver thicknesses, representing the *asymmetric* closed cavities, that is the only sample that exhibited a non-monotonic behaviour varying the thickness of the top metal layer, and C25Y60C25, to further study the only *symmetric* cavity, both without silver and with 5nm. The other two thicknesses were disregarded, as they were found to be non-superconducting according to the MWA measurements (figure 4.10). The samples were studied in reflection geometry, since in transmission the signal intensity was too weak. The blue pump was tuned to 400nm (3.1eV), while the mid-infrared pump was tuned to 11µm (113meV). Furthermore, we will focus only on a probe energy of ∼1.31eV, that is an energy at we have seen a change in the differential signal in correspondence of the transition. Considering the MWA measurements described in the previous chapter, we

focused on a temperature range from 10K to 100K.

The measured quantity is the intensity of the i-th frequency component of the reflected probe beam $R_i^s(\lambda, t_1, t_2, T)$, in parallel, we also acquired the reference probe beam $R_i^r(\lambda, t_1, t_2, T)$, where t_1 is the time delay between the two pumps, t_2 is the delay between the white-light probe and the blue pump, T is the sample temperature. Thus the observable is the referenced average differential reflectivity change, defined as

$$\frac{\Delta R}{R}(\lambda, t_1, t_2, T) = \frac{\sum_{i=1}^{N} R_i^{s,P}(\lambda, t_1, t_2, T)}{\sum_{i=1}^{N} R_i^{r,P}(\lambda, t_1, t_2, T)} - \frac{\sum_{i=1}^{N} R_i^{s,U}(\lambda, t_1, t_2, T)}{\sum_{i=1}^{N} R_i^{r,U}(\lambda, t_1, t_2, T)}, \tag{6.1}$$

where N is the number of pulses over which the integration is performed, the superscripts P and U refer to "pumped" and "unpumped" probe pulses. Unpumped pulses are those that are reflected by the sample when both pumps are blocked by the choppers. With pumped pulses we refer to all the three possible configurations shown in figure 6.2: both pumps (PP-map), only mid-IR pump (MIR-map) and only blue pump (Blue-map). For each of these four dimensional maps, we calculated and subtracted an average time-independent signal over the negative t_2 times. Each curve is corrected subtracting a background spectrum that is acquired by blocking only the probe beam, while the two pumps are left open.

In the parameter space, different combinations can be obtained by fixing two parameters at a time and leaving the others free. In our case, we will focus on two specific configurations, bearing in mind that, as already discussed, we will consider only the case in which the pumps are synchronous (i.e. $t_1 = 0$). The first configuration is obtained by leaving the delay between the pumps and the probe (t_2) and the probe wavelengths free, while fixing the temperature, $\Delta R/R(t_2, \lambda)$. The second configuration is obtained by fixing the probe wavelength and varying the temperature, $\Delta R/R(t_2, T)$.

To study the possible modification in the dynamics due to the combined pumps actions, we subtract from the PP-map the MIR-map and the Blue-map (figure 6.3):

$$\frac{\Delta\Delta R}{R} = \frac{\Delta R^{PP}}{R} - \frac{\Delta R^{Blue}}{R} - \frac{\Delta R^{MIR}}{R}, \tag{6.2}$$

we will refer to this new map as "differential map".

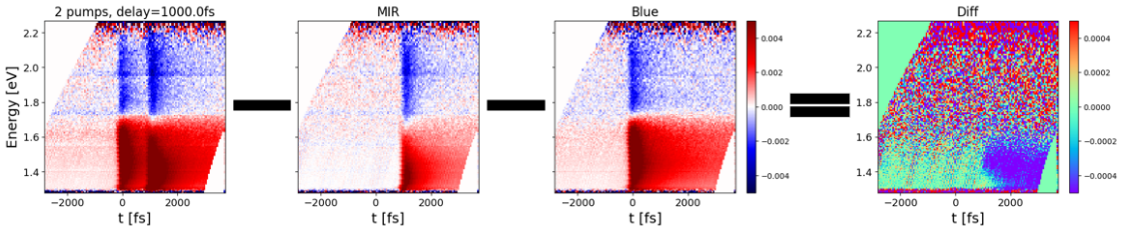

Figure 6.3: **Optical map for sample Ag0-Y60C5 at 12K.** The first map represents the optical response of the two combined pumps delayed of t_1=1000fs. By subtracting the second and third maps (only MIR and Blue pump respectively), we obtain the "differential map", that therefore represents the non linear response of the sample.

All these possible maps are shown in figure 6.4. The first row displays the maps in which the temperature is fixed at 12K, below the critical temperature of 55K: in order, the map showing the transient reflectivity of the broadband probe after the action of the

MIR pump only, the effect of the Blue pump only and the non-linear response given by the "differential map". The second row is analogous, but taken above T_C, at a temperature of about 80K. We can observe that in the differential map a short positive signal is present below T_C, which is no longer visible above T_C. In the third row, the probe energy was fixed at 1.31eV, that is the energy at which the positive signal is present, and a temperature scan was performed. We observe that a temperature-dependent transition is visible only in the differential map, while no superconducting-features are visible in those maps referring to the excitation of single pump pulses. Thus confirming that the superconducting behaviour of the signal is indeed non-linear.

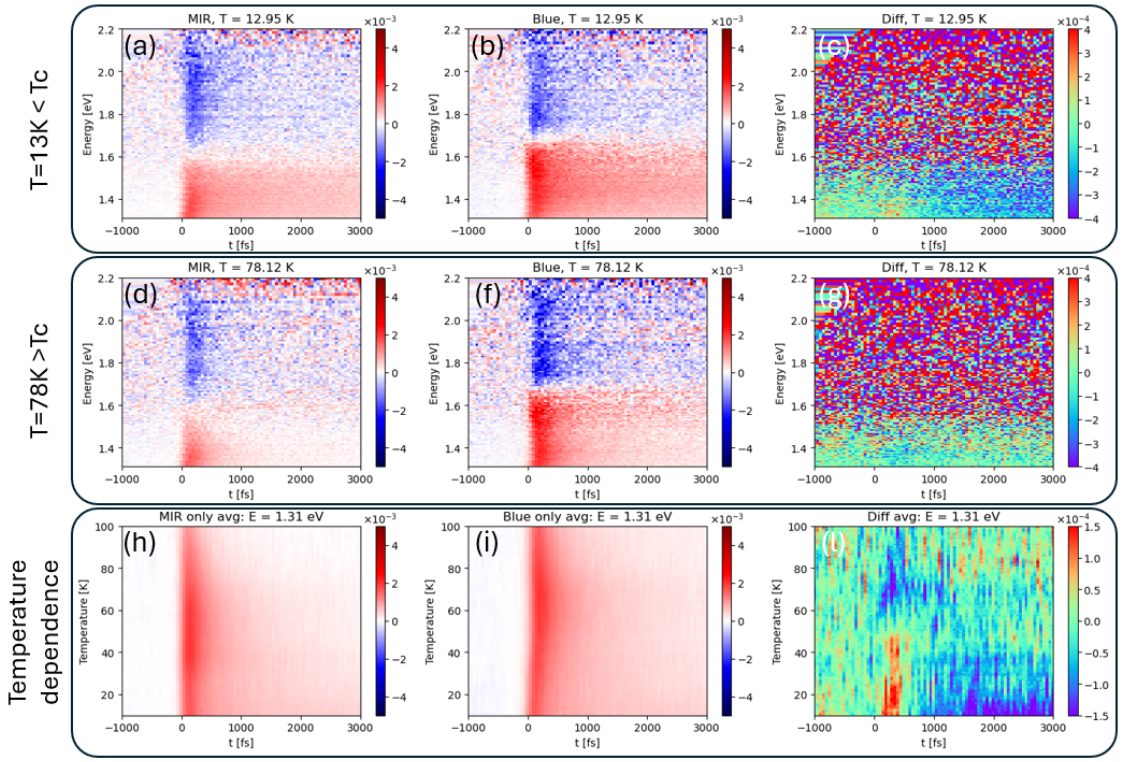

Figure 6.4: **Optical measurements performed with a three-pulse scheme on sample Ag0-Y60C5.** The first row shows maps acquired below the critical temperature $T_C = 55K$, while the second row corresponds to measurements above T_C. The left column (a,d,h) shows the response to the MIR pump only, the central column to the Blue pump only (b,f,i), and the right column displays the differential maps resulting from the combined action of both pumps at temporal overlap (c,g,l). The third row presents the thermal evolution of the probe signal at an energy of 1.31eV; only the differential map reveals the phase transition.

6.3 Temperature scan

In this section, we present the temperature scans of 4 out of the 6 samples studied. The Y60C5 samples with 10nm and 15nm of silver did not show any transition increasing the temperature, most likely due to the continuous degradation observed during the MWA measurements, discussed in the previous chapter.

We will compare the results obtained through optical measurements with the ones obtained via MWA measurements. In order to estimate the critical temperature from the differential maps presented before, we fitted the time-dependent differential signal at a given temperature d(T) as a linear combination of two pump-probe traces [8], one at low temperature (∼15K, d_{low}), the other at higher temperature (∼80K-90K, depending on the sample, d_{high}):

$$d(T) = a(T)d_{low} + b(T)d_{high}, \tag{6.3}$$

where $a(T)$ and $b(T)$ are the fitting parameters depending on temperature. The crossover point between the two curves will be interpreted as the critical temperature.

6.3.1 Sample Y60C5

Ag0-Y60C5

For the Ag0-Y60C5 sample, transport measurements estimated a central critical temperature of about 63K. The MWA measurements confirmed the transition range, setting it between approximately 50K and 64K, slightly shifted toward lower temperatures compared to the transport measurements. This difference can be explained by the fact that transport measurements probe only a portion of the sample, that is the specific path followed by the charge carriers, whereas MWA measurements probe the entire sample, thus considering an average contribution from defects and inhomogeneities as well.

The results of the fitting procedure and the comparison with the previous results are plotted in figure 6.5. The crossover point defines a critical temperature of 55.4K, in very good agreement with the MWA measurement, that sets T_C at 55.5K. Moreover, the transition region estimated from the MWA measurement (46-64K) matches well the region of the differential map where the positive signal vanishes, and is replaced by the negative one.

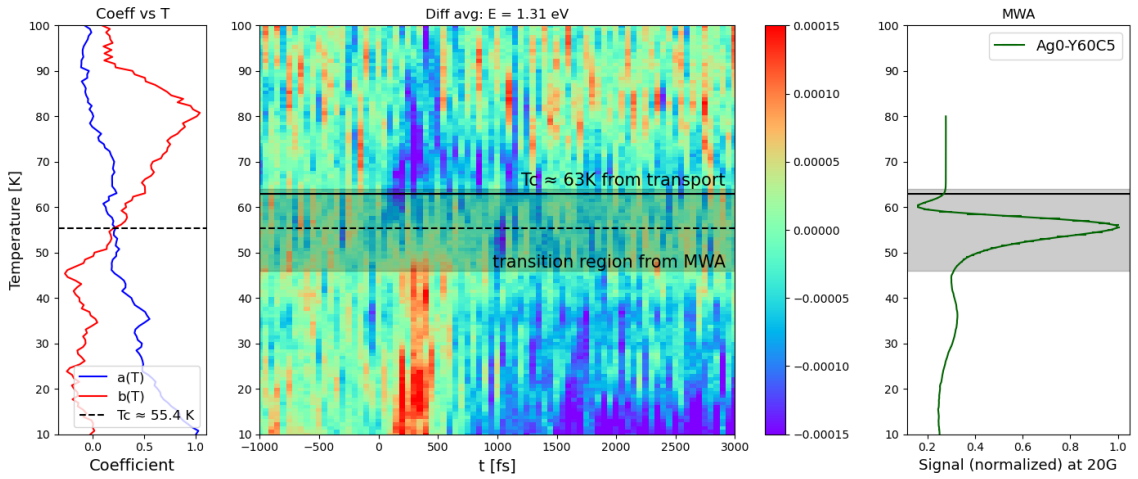

Figure 6.5: **Temperature scan compared with the one performed with MWA technique for sample Ag0-Y60C5.** On the left, the coefficients obtained from fitting are plotted; the critical temperature is estimated by identifying the crossover point between the two curves. On the right, the MWA measurement (see previous chapter) highlights the transition region. The central panel shows the temperature scan performed using the Pump-probe technique, with both the critical temperature from transport measurements and the transition region identified via MWA overlaid. The good agreement with MWA technique confirms that the Pump-probe method can also be reliably used to determine the critical temperature.

Ag5-Y60C5

Referring to the analysis performed on MWA measurement, the most promising sample was Ag15-Y60C5, as it was the one with the highest critical temperature, surprisingly higher with respect of the samples with thinner layer of silver. However, the only sample in which we could seen a transition in the differential map, was the sample with 5nm of silver, that showed the peak in the MWA signal at a very low temperature of 13K. We recall that the silver deposition was performed on the same sample that was later cut. In this way, any effects arising from differences in the deposition process of the YBCO layer can be disregarded, and the observed response can be attributed exclusively to the silver layer.

The differential signal of this sample is qualitatively different with respect to the signal of the uncapped sample, most likely due to a modified equilibrium dielectric function in the cavity [8]. As we can see in figure 6.6, the positive signal at low temperatures that was present in the open cavity is not visible in this sample, but a non-linear temperature-dependent signal is still present. By performing the analysis already described, the crossover between the $a(T)$ and $b(T)$ parameters occurs at 87K, suggesting that a superconducting behaviour is surviving in the cavity-like heterostructure at higher temperature with respect to the uncapped sample (see figure 6.7).

On the other hand, one may question if this signal can be interpreted as an indicator of the sample's superconducting behaviour, given the qualitative differences in the signal with respect to the one on the uncapped sample. As previously mentioned, this difference could be attributed to a modification of the dielectric function within the cavity. However, one

cannot ignore the possibility that this signal does not actually indicate the superconducting phase, but rather the pseudogap phase, as could also be the case for the negative signal observed in the sample without silver above 55K.

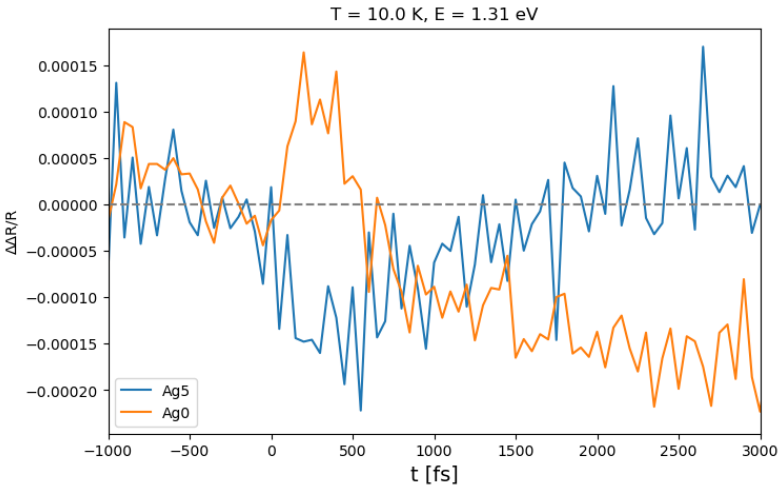

Figure 6.6: **Non-linear signal at 10K for sample Ag5- and Ag0-Y60C5.** At the energy under study, 1.31eV, the uncapped sample exhibits a short positive signal, that is later replaced by a negative signal is present. In the cavity-enclosed sample, only a longer negative signal is present.

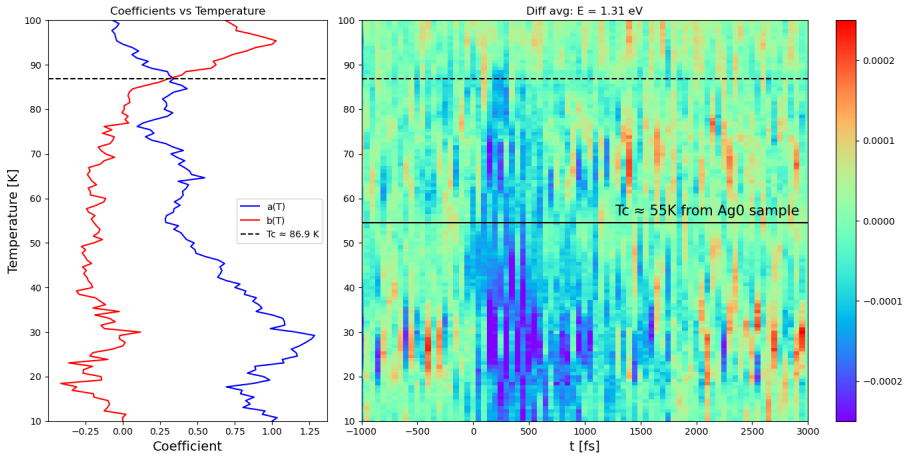

Figure 6.7: **Temperature scan of sample Ag5-Y60C5.** At E=1.31eV, only a negative signal is observed in the sample capped with silver, no positive component is visible. Applying the same fitting procedure, a transition temperature of approximately 87K was estimated, corresponding to the crossover point between the fitting curves. This temperature is significantly higher than that obtained for the uncapped sample, and also exceeds the value observed in MWA measurements.

6.3.2 Sample C25Y60C25

Similar results were observed for this set of samples: in the sample without silver, a sign change of the differential signal was observed at the transition temperature, whereas in the sample capped with silver, the signal is longer in time but does not show a clear transition.

Ag0-C25Y60C25

For the uncapped sample, the same analysis previously performed could be applied, in which the crossover between the fitting parameters indicated a critical temperature of 53K (figure 6.8). This value is consistent with the results from the MWA measurements, where the transition range was estimated by comparing data acquired after zero-field cooling and after cooling in a finite magnetic field. The temperature range over which the two signals begin to overlap, up to the temperature where the signal becomes constant, is interpreted as the superconducting transition region (for more details, see section 4.3).

The long positive signal that appears after the shorter negative one can be interpreted, in an analogues way to the previous sample, as characteristic of the pseudogap phase. We did not perform a temperature scan for higher temperatures so we cannot know exactly where it disappears, but as we can see in figure 6.9 at room temperature it is not present, suggesting that this signal is still an indicator of a non-linear phase of the sample, most likely of the pseudogap phase.

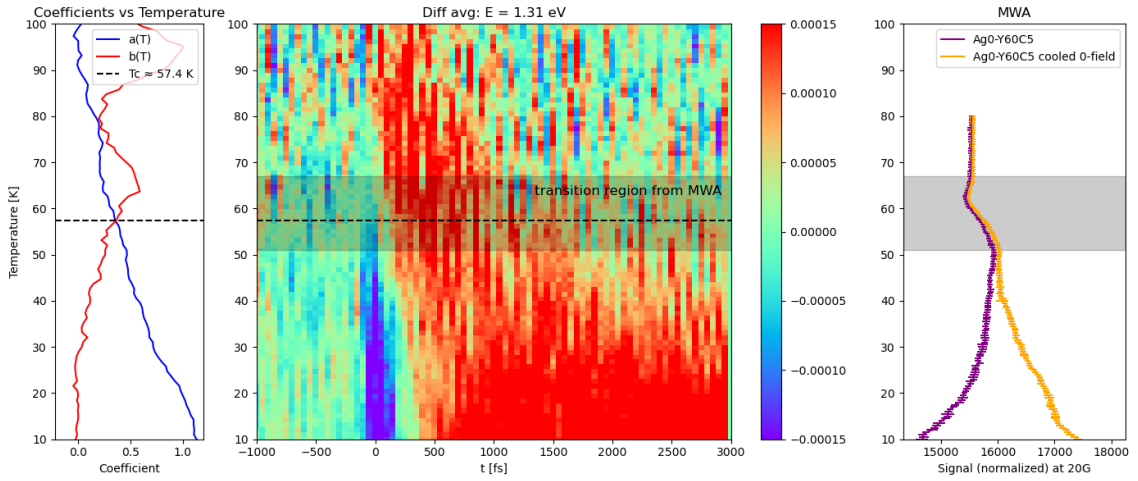

Figure 6.8: **Temperature scan compared with the measurement performed using the MWA technique of sample Ag0-C25Y60C25.** As previously shown, the left panel displays the fit coefficients, with the critical temperature identified as the crossover point. The central panel shows the temperature scan obtained using the pump&probe technique. In the right panel, we compare two MWA measurements: one performed at 20 G after a full magnetic field sweep (purple), and one acquired after a zero-field cooling (orange). The temperature range from where the two signals begin to overlap to the temperature in which the signal becomes constant is interpreted as the superconducting transition region.

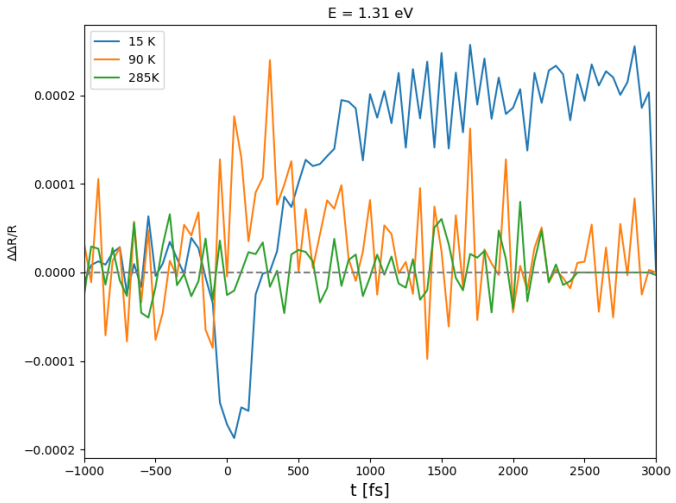

Figure 6.9: **Temperature dependence of the non-linear signal of Ag0-C25Y60C25 sample.** Horizontal cuts at 1.31eV: the fast negative signal at 15K can be interpreted as superconducting, the positive signal at 90K as characteristic of the pseudogap phase. At room temperature the non-linear signal disappears.

Ag5-C25Y60C25

For the last analysed sample, it was not possible to perform a fit to determine the transition temperature, as the negative signal is absent and the positive signal extends well beyond the studied temperature range. Indeed, as shown in the temperature scan in figure 6.10, this signal persists even above 130K. Observing the extracted cuts (figure 6.11), it is apparent that at low temperatures the negative signal is very weak, if not entirely absent, whereas at higher temperatures the two signals are almost identical. This behaviour suggests a possible suppression of the superconducting properties in the sample at low temperatures, leaving visible only the pseudogap phase, as indicated by the positive signal.

In summary, from the optical measurements we were able to estimate the critical temperature only for the "open cavity" samples. The value obtained is consistent with previous characterizations, confirming the suitability of three-pump spectroscopy for identifying the superconducting transition in cuprates.

In contrast, in the "closed cavity" samples, both symmetric and asymmetric, the superconducting phase appears to be almost completely suppressed. In these samples, it does not seem possible to identify any discontinuity in the linear response that could be associated with the critical temperature, leaving instead only a nonlinear signal that persists at higher temperatures, which can be related to the pseudogap phase. To further investigate the nature of this signal, it would be useful to extend the explored temperature range in order to determine the point at which it vanishes.

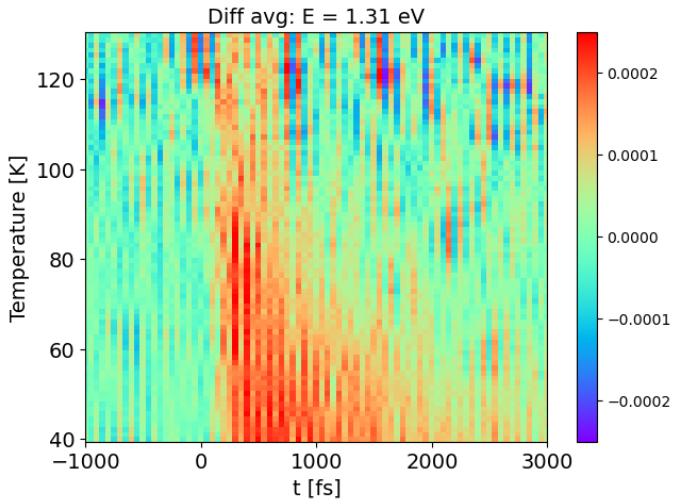

Figure 6.10: **Temperature scan in range 40-130K of sample Ag5-C25Y60C25.** Only a positive signal is observed up to 130K, at a higher temperature with respect to all other samples studied.

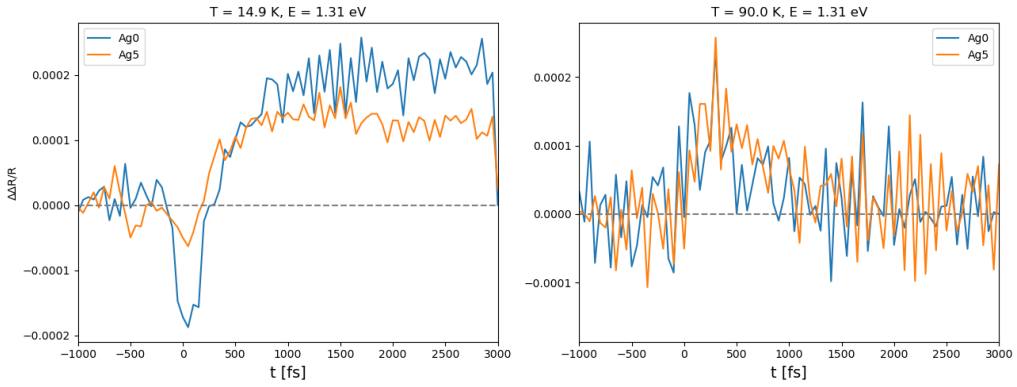

Figure 6.11: **Non-linear signal at 10K and 90K for sample Ag5- and Ag0-C25Y60C25.** Comparing uncapped sample (blue) and cavity-enclosed sample (orange), we can notice a difference in the signal at 1.31eV lower temperature: in the sample without silver the fast negative signal at the overlap with pump is a lot more intense with respect to the capped sample. Instead, at higher temperature the two signals match quite well.

Conclusions

The purpose of this thesis was to explore how to engineer a cavity designed to couple the charge-transfer (CT) transition of the YBCO cuprate with confined electromagnetic fields, and how these new heterostructures could influence the superconducting behaviour of YBCO. Starting from the theoretical design and the synthesis of these heterostructures and proceeding with different kinds of characterization, we studied the possibility of modifying the superconducting phase through strong light-matter coupling, both at equilibrium (through transport and microwave absorption measurements) and out of equilibrium (via time-resolved spectroscopy).

Pulsed Laser Deposition (PLD) enabled the growth of multilayer heterostructures designed to be resonant with the CT transition of YBCO. PLD allowed the fabrication of high-quality monocrystalline layers, as demonstrated by X-Ray Diffraction (XRD). Different cavity geometries were obtained by varying the thickness of YBCO, CeO_2, and the top silver layer. While the latter determined the cavity quality factor, it also had a strong influence on the superconducting behaviour of the structures.

Transport measurements confirmed superconductivity only in uncapped samples, i.e. those terminating with a YBCO layer. To investigate capped structures, microwave absorption (MWA) was employed and proved to be a powerful complementary technique. The results showed that capped samples also exhibit superconductivity, although with a reduction of the critical temperature. Silver in direct contact with YBCO broadened and shifted the transition, whereas in sample C25Y60C25, where an amorphous CeO_2 layer separates YBCO from silver, the transition was even more broadened and modified in shape. These behaviours might indicate proximity-induced or long-range cavity-related phenomena, although the systematic lowering of the critical temperature over time rather suggests extrinsic degradation processes. Altogether, these findings emphasized the crucial role of interface engineering: the quality of the interfaces proved fundamental for the reproducibility of the measurements and for achieving reliable control of the superconducting phase.

Time-resolved spectroscopy provided additional insight into the interaction between cavity modes and the CT transition of YBCO. Temperature-dependent measurements revealed modifications of the transient signal at temperatures comparable to those estimated from MWA in uncapped samples. In capped samples, an enhancement of the non-linear response was observed at higher temperatures, although it remains unclear whether this originates from the superconducting phase or from the pseudogap phase. Moreover, the superconducting transition could be tracked as a function of temperature only within a very narrow probe energy window centred at 1.3 eV. A plausible explanation is the redistribution of spectral weight toward energies lower than the CT band at 1.8 eV with increasing

doping. It is possible that, for the doping level of the samples analysed, this feature may be shifted to lower energies.

The results highlight several directions for future research. The degradation and suppression of superconductivity are most likely linked to the deposition of amorphous layers and to poor interface quality. Future work should therefore focus on optimizing the epitaxial growth of capping layers in order to preserve the stoichiometry of YBCO and improve the structural quality of the interfaces. Another open issue concerns the stability of the silver layer, which is inclined to oxidation. Alternative materials, such as gold, could be explored to ensure better chemical stability.

Further studies will also be required to disentangle intrinsic cavity-induced effects from extrinsic degradation processes, in order to establish whether cavity engineering can genuinely modify the superconducting state of YBCO.

Finally, extended optical investigations, both at equilibrium and out of equilibrium, with varying probe energies and controlled doping, could be performed to clarify the origin of the narrow spectral window and its possible connection to spectral weight redistribution across the CT band.

Appendix A

Electron Paramagnetic Resonance Spectroscopy

It is well known that molecules and atoms have discrete energy states, that differ in energy $\Delta E = h\nu$, where ν is the frequency of the electromagnetic radiation needed to have a transition between the two states. In spectroscopy usually the frequency is varied until absorption occurs at the frequency in correspondence with the energy difference between the two states. In Electron Paramagnetic Resonance (EPR) spectroscopy — also commonly referred to as Electron Spin Resonance (ESR) — the frequency is typically kept constant in the gigahertz range. To induce the transition between the two levels, a varying magnetic field is applied. In fact in the case of a simple paramagnet, the energy differences is due to the interaction of the spin of unpaired electrons in the sample with a magnetic field H. Single unpaired electrons have two allowed energy states: the one with lower energy when the magnetic moment μ of electrons is aligned with the magnetic field, the other with higher energy when μ is aligned antiparallel to H, as shown in figure A.1. This effect is called Zeeman effect. The difference in energy of these two states is $\Delta E = g\mu_B H$, where g is the g-factor ($\sim$2 for a free electron) and μ_B is the Bohr magneton. Therefore the energy required to have the transition, is given by

$$h\nu = g\mu_B H. \tag{A.1}$$

Absorption occurs when the applied field is $H = H_{res}$, that is when the magnetic field "tunes" the two spin states such that the difference in energy is equal to the energy of the applied radiation. The field H_{res} is called *resonance field*.

From the latter relation we can see that if the applied field is zero, the two states have the same energy and there is no energy difference that can be measured. Furthermore, this difference grows linearly with the magnetic field.

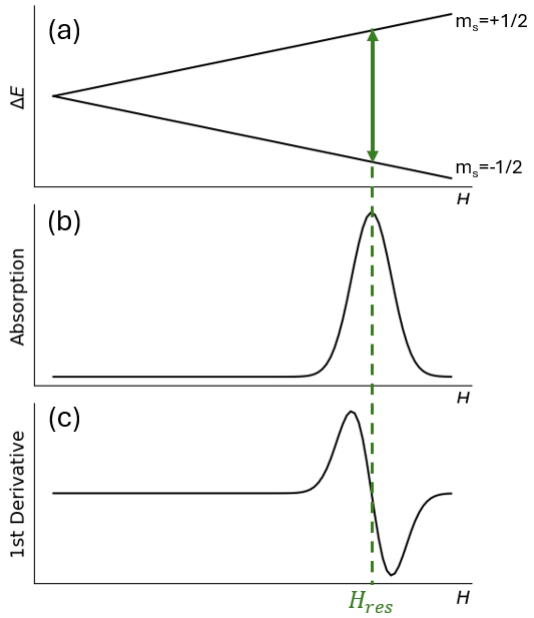

Figure A.1: **(a) Dependence of the spin state energies on the applied magnetic field.** H_{res} is the applied magnetic field such that there is absorption. Also absorption (b) and first derivative of absorption (c) are plotted.

A.1 Paramagnetic signals

As shown in figure A.2a, at a temperature of 5K distinct electron spin resonance (ESR) lines are observed at approximately 2550G, 3600G, and 4400G. These lines remain visible also at room temperature (figure A.2b). The key question concerns the origin of these resonances. Since the focus of our heterostructures is to control the superconducting transition of the YBCO layer, it is essential to ensure that no magnetic signals originate from this layer. The measurements clearly demonstrate that the observed ESR lines stem from the substrate. Figure A.2b presents full-sweep measurements for samples fabricated by sequentially adding layers starting from the bare LAO substrate: the ESR lines are consistently present, starting from the substrate alone. Thus, the addition of further layers may modify the lineshape but not their positions, confirming that their origin is not related to YBCO.

In an EPR experiment, the cavity is typically tuned such that only the absorption component is detected, leading to a symmetric derivative signal. However, in metals the EPR lineshape is generally asymmetric due to the admixture of absorption and dispersion contributions [49]. This asymmetry arises because electron diffusion relative to the surface occurs on a timescale longer than the spin-relaxation times [50]. The main effect of this process is to distort the signal lineshape. This mechanism may account for the absence of positive lobes in the spectra observed after deposition of the LNO metallic layer, an effect particularly evident at low temperature, as shown in figure A.2a.

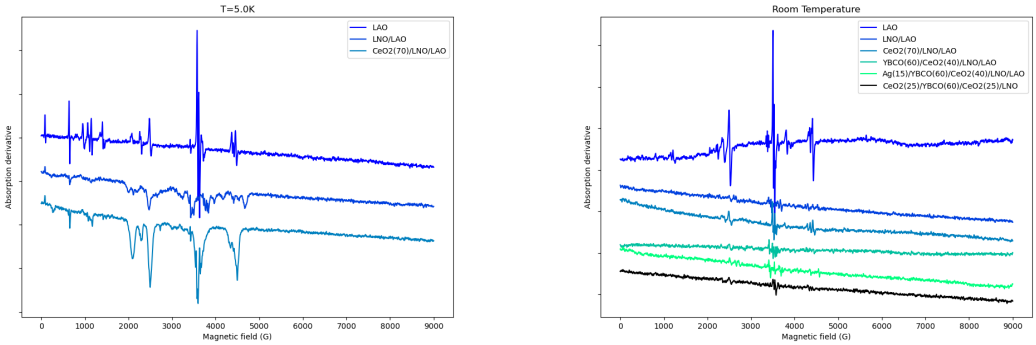

(a) (b)

Figure A.2: **Electron Spin Resonance lines at 5K and room temperature adding one layer after the other**: the paramagnetic signals originate from the LAO substrate. At 5K (a) ESR lines for the samples without YBCO layer, adding LNO the shape of these lines changes due to the metallic behaviour of this layer, adding also CeO_2 does not add other lines. At room temperature (b) also the samples with YBCO layer, and the one capped with amorphous CeO_2 or silver. (Data are shifted)

Appendix B

Dielectric function models

B.1 Drude-Lorentz model

Using the Lorentz-Drude model, we can write the dielectric function considering the contribution of N oscillators:

$$\varepsilon(\omega) = \varepsilon_\infty - \frac{f_0\omega_p}{\omega^2 + i\omega\gamma_0} + \sum_{j=1}^{N} \frac{f_j\,\omega_p}{\omega_{0j}^2 - \omega^2 - i\omega\gamma_j}, \tag{B.1}$$

where ε_∞ is the high frequency dielectric constant and the second term refers to free electrons. $\omega_p = \sqrt{\frac{Ne^2}{m}}$ is the plasma frequency, γ_j, ω_{0j} and f_j are the broadening, frequency and strength of the j-th oscillator, respectively.

The dielectric function is a complex quantity, therefore it can be written as the sum of the real and imaginary part:

$$\begin{aligned}\varepsilon(\omega) &= \varepsilon_1(\omega) + i\varepsilon_2(\omega) \\ &= \varepsilon_\infty + \sum_{j=0}^{N} \frac{(\omega_{0j}^2 - \omega^2) f_j\,\omega_p^2}{(\omega_{0j}^2 - \omega^2)^2 + \omega^2\gamma_j^2} + i\sum_{j=0}^{N} \frac{\omega\gamma_j f_j\,\omega_p^2}{(\omega_{0j}^2 - \omega^2)^2 + \omega^2\gamma_j^2}.\end{aligned} \tag{B.2}$$

The free electron term was embedded into the sum, making it starts from $j = 0$ and setting $\omega_{0,j=0} = 0$.

B.2 Tauc-Lorentz model

The Tauc-Lorentz model works well for amorphous materials and can be a good approximation for crystalline materials when the absorption is described by a single broad peak [25]. Considering only one oscillator the imaginary part of the dielectric function can be written as:

$$\varepsilon_2(E) = \begin{cases} \dfrac{AE_0\Gamma\,(E - E_g)^2}{E\left[(E^2 - E_0^2)^2 + \Gamma^2E^2\right]}, & E > E_g, \\ 0, & E \leq E_g. \end{cases} \tag{B.3}$$

where E_g is the bandgap of the material, A is the oscillator amplitude, E_0 is the energy of the Lorentz peak, and Γ is the broadening parameter. This model can also be generalized for a case of multiple oscillators.

The real part of the dielectric function can be calculated as the Kramers–Kronig transform [51]:

$$\varepsilon_1(E) = \varepsilon_\infty + \frac{2}{\pi}\,\mathcal{P}\int_{E_g}^{\infty} \frac{\xi\,\varepsilon_2(\xi)}{\xi^2 - E^2}\,d\xi, \tag{B.4}$$

where ε_∞ is the dielectric function at infinite energy and the $\mathcal{P}$ represents the Cauchy principal part of the integral

Bibliography

[1] M. Rini, R. I. Tobey, N. Dean, J. Itatani, Y. Tomioka, Y. Tokura, R. W. Schoenlein, and A. Cavalleri. Nonlinear phononics as an ultrafast route to lattice control. *Nature Physics*, 7:854–856, 2011.

[2] W. Hu, S. Kaiser, D. Nicoletti, C. R. Hunt, I. Gierz, M. C. Hoffmann, M. Le Tacon, T. Loew, B. Keimer, and A. Cavalleri. Optically enhanced coherent transport in $yba_2cu_3o_{6.5}$ by ultrafast redistribution of interlayer coupling. *Nature*, 516:71–73, 2014.

[3] F. Schlawin, D. M. Kennes, and M. A. Sentef. Cavity quantum materials. *Applied Physics Reviews*, 9(1):011312, 02 2022.

[4] Rohit Chikkaraddy, Bart De Nijs, Felix Benz, Steven J. Barrow, Oren A. Scherman, Edina Rosta, Angela Demetriadou, Peter Fox, Ortwin Hess, and Jeremy J. Baumberg. Single-molecule strong coupling at room temperature in plasmonic nanocavities. *Nature*, 535(7610):127–130, 2016.

[5] K. Santhosh, O. Bitton, L. Chuntonov, and G. Haran. Vacuum rabi splitting in a plasmonic cavity at the single quantum emitter limit. *Nature Communications*, 7, 2016.

[6] Francisco J. Garcia-Vidal, Cristiano Ciuti, and Thomas W. Ebbesen. Manipulating matter by strong coupling to vacuum fields. *Science*, 373(6551):eabd0336, 2021.

[7] S. Latini, D. Shin, S. A. Sato, U. De Giovannini, H. Hübener, and A. Rubio. Cavity control of ferroelectric phase transitions. *Phys. Rev. X*, 10:041027, 2020.

[8] Giacomo Jarc. *Control of collective phenomena in complex materials through cavity electrodynamics*. Phd thesis, University of Trieste, 2023.

[9] Alexey V. Kavokin, Jeremy J. Baumberg, Guillaume Malpuech, and Fabrice P. Laussy. *Microcavities*. Series on Semiconductor Science and Technology. Oxford University Press, Oxford, UK, 2nd edition, 2017.

[10] Kerry J. Vahala. Optical microcavities. *Nature*, 424:839–846, 2003. Published August 14, 2003.

[11] Mor M. Roses and Emanuele G. Dalla Torre. Dicke model. *PLOS ONE*, 15(9):1–8, 09 2020.

[12] Courtney A. DelPo, Bryan Kudisch, Kyu Hyung Park, Saeed-Uz-Zaman Khan, Francesca Fassioli, Daniele Fausti, Barry P. Rand, and Gregory D. Scholes. Polariton transitions in femtosecond transient absorption studies of ultrastrong light–molecule

coupling. *The Journal of Physical Chemistry Letters*, 11(7):2667–2674, 2020. PMID: 32186878.

[13] Stanley Pau, Gunnar Björk, Joseph Jacobson, Hui Cao, and Yoshihisa Yamamoto. Microcavity exciton-polariton splitting in the linear regime. *Phys. Rev. B*, 51:14437–14447, May 1995.

[14] Francisco J. Garcia-Vidal, Cristiano Ciuti, and Thomas W. Ebbesen. Manipulating matter by strong coupling to vacuum fields. *Science*, 373(6551):eabd0336, 2021.

[15] I-Te Lu, Dongbin Shin, Mark Kamper Svendsen, Simone Latini, Hannes Hübener, Michael Ruggenthaler, and Angel Rubio. Cavity engineering of solid-state materials without external driving. *Adv. Opt. Photon.*, 17(2):441–525, Jun 2025.

[16] I-Te Lu, Dongbin Shin, Mark Kamper Svendsen, Hannes Hübener, Umberto De Giovannini, Simone Latini, Michael Ruggenthaler, and Angel Rubio. Cavity-enhanced superconductivity in mgb₂ from first-principles quantum electrodynamics (qedft). *Proceedings of the National Academy of Sciences*, 121(50):e2415061121, 2024.

[17] M. A. Sentef, M. Ruggenthaler, and A. Rubio. Cavity quantum-electrodynamical polaritonically enhanced electron-phonon coupling and its influence on superconductivity. *Science Advances*, 4(11):eaau6969, 2018.

[18] Itai Keren, Tatiana A. Webb, Shuai Zhang, Jikai Xu, Dihao Sun, Brian S. Y. Kim, Dongbin Shin, Songtian S. Zhang, Junhe Zhang, Giancarlo Pereira, Juntao Yao, Takuya Okugawa, Marios H. Michael, James H. Edgar, Stuart Wolf, Matthew Julian, Rohit P. Prasankumar, Kazuya Miyagawa, Kazushi Kanoda, Genda Gu, Matthew Cothrine, David Mandrus, Michele Buzzi, Andrea Cavalleri, Cory R. Dean, Dante M. Kennes, Andrew J. Millis, Qiang Li, Michael A. Sentef, Angel Rubio, Abhay N. Pasupathy, and Dmitri N. Basov. Cavity-altered superconductivity, 2025.

[19] A. Thomas, E. Devaux, K. Nagarajan, T. Chervy, M. Seidel, G. Rogez, J. Robert, M. Drillon, T. T. Ruan, S. Schlittenhardt, M. Ruben, D. Hagenmüller, S. Schütz, J. Schachenmayer, C. Genet, G. Pupillo, and T. W. Ebbesen. Exploring superconductivity under strong coupling with the vacuum electromagnetic field. *The Journal of Chemical Physics*, 162(13):134701, 04 2025.

[20] Giacomo Jarc, Shahla Yasmin Mathengattil, Angela Montanaro, Francesca Giusti, Enrico Maria Rigoni, Rudi Sergo, Francesca Fassioli, Stephan Winnerl, Simone Dal Zilio, Dragan Mihailovic, et al. Cavity-mediated thermal control of metal-to-insulator transition in 1t-tas2. *Nature*, 622(7983):487–492, 2023.

[21] Angela Montanaro, Enrico Maria Rigoni, Francesca Giusti, Luisa Barba, Giuseppe Chita, Filippo Glerean, Giacomo Jarc, Shahla Y. Mathengattil, Fabio Boschini, Hiroshi Eisaki, Martin Greven, Andrea Damascelli, Claudio Giannetti, Dragan Mihailovic, Viktor Kabanov, and Daniele Fausti. Dynamics of nonthermal states in optimally doped $Bi_2Sr_2Ca_{0.92}y_{0.08}Cu_2o_{8+\delta}$ revealed by midinfrared three-pulse spectroscopy. *Phys. Rev. B*, 110:125102, Sep 2024.

[22] S. L. Cooper, D. Reznik, A. Kotz, M. A. Karlow, R. Liu, M. V. Klein, W. C. Lee, J. Giapintzakis, D. M. Ginsberg, B. W. Veal, and A. P. Paulikas. Optical studies of

the a-, b-, and c-axis charge dynamics in $yba_2cu_3o_{6+x}$. *Phys. Rev. B*, 47:8233–8248, Apr 1993.

[23] Giacomo Jarc, Shahla Y. Mathengattil, Francesca Giusti, Maurizio Barnaba, Abhishek Singh, Angela Montanaro, Filippo Glerean, Enrico M. Rigoni, Simone Dal Zilio, Stephan Winnerl, and Daniele Fausti. Tunable cryogenic terahertz cavity for strong light–matter coupling in complex materials. *Review of Scientific Instruments*, 93(3):033102, 2022.

[24] M. Claudia Troparevsky, Adrian S. Sabau, Andrew R. Lupini, and Zhenyu Zhang. Transfer-matrix formalism for the calculation of optical response in multilayer systems: from coherent to incoherent interference. *Opt. Express*, 18(24):24715–24721, Nov 2010.

[25] Cayla Marie Nelson, Maria Spies, Lina S. Abdallah, Stefan Zollner, Yun Xu, and Hongmei Luo. Dielectric function of laalo3 from 0.8 to 6 ev between 77 and 700 k. *Journal of Vacuum Science & Technology A*, 30(6):061404, October 2012.

[26] Aleksandar D. Rakić, Aleksandra B. Djurišić, Jovan M. Elazar, and Marian L. Majewski. Optical properties of metallic films for vertical-cavity optoelectronic devices. *Appl. Opt.*, 37(22):5271–5283, Aug 1998.

[27] J. J. Zhu, W. W. Li, Y. W. Li, Y. D. Shen, Z. G. Hu, and J. H. Chu. Effects of applied electrical field on electronic structures in lanio3 conductive metallic oxide film: An optical spectroscopic study. *Applied Physics Letters*, 97(21):211904, 11 2010.

[28] S. Vangelista, R. Piagge, S. Ek, T. Sarnet, G. Ghidini, C. Martella, and A. Lamperti. Structural, chemical and optical properties of cerium dioxide film prepared by atomic layer deposition on tin and si substrates. *Thin Solid Films*, 636:78–84, 2017.

[29] Robert Eason, editor. *Pulsed Laser Deposition of Thin Films: Applications-Led Growth of Functional Materials*. Wiley-Interscience, Hoboken, NJ, 2007.

[30] P. R. Willmott and J. R. Huber. Pulsed laser vaporization and deposition. *Rev. Mod. Phys.*, 72:315–328, Jan 2000.

[31] J. Schou. Physical aspects of the pulsed laser deposition technique: The stoichiometric transfer of material from target to film. *Applied Surface Science*, 255(10):5191–5198, 2009. Laser and Plasma in Micro- and Nano-Scale Materials Processing and Diagnostics.

[32] Rajiv K. Singh and J. Narayan. Pulsed-laser evaporation technique for deposition of thin films: Physics and theoretical model. *Phys. Rev. B*, 41:8843–8859, May 1990.

[33] Sandeep Kumar Chaluvadi, Shyni Punathum Chalil, Federico Mazzola, Simone Dolabella, Piu Rajak, Marcello Ferrara, Regina Ciancio, Jun Fujii, Giancarlo Panaccione, Giorgio Rossi, et al. Nd: Yag infrared laser as a viable alternative to excimer laser: Ybco case study. *Scientific Reports*, 13(1):3882, 2023.

[34] H. A. Mook, M. Yethiraj, G. Aeppli, T. E. Mason, and T. Armstrong. Polarized neutron determination of the magnetic excitations in $yba_2cu_3o_7$. *Phys. Rev. Lett.*, 70:3490–3493, May 1993.

[35] H. Zhai and Wei-Kan Chu. Effect of interfacial strain on critical temperature of yba2cu3o7 thin films. *Applied Physics Letters*, 76:3469–3471, 06 2000.

[36] Jens Als-Nielsen and Des McMorrow. *Elements of Modern X-ray Physics*. Wiley, Hoboken, NJ, 2 edition, 2011.

[37] Zhengxiang Ma, R. C. Taber, L. W. Lombardo, A. Kapitulnik, M. R. Beasley, P. Merchant, C. B. Eom, S. Y. Hou, and Julia M. Phillips. Microwave penetration depth measurements on $bi_2sr_2cacu_2o_8$ single crystals and $yba_2cu_3o_{7-\delta}$ thin films. *Phys. Rev. Lett.*, 71:781–784, Aug 1993.

[38] W. Braunisch, N. Knauf, V. Kataev, S. Neuhausen, A. Grütz, A. Kock, B. Roden, D. Khomskii, and D. Wohlleben. Paramagnetic meissner effect in bi high-temperature superconductors. *Phys. Rev. Lett.*, 68:1908–1911, Mar 1992.

[39] K. W. Blazey, K. A. Müller, J. G. Bednorz, W. Berlinger, G. Amoretti, E. Buluggiu, A. Vera, and F. C. Matacotta. Low-field microwave absorption in the superconducting copper oxides. *Phys. Rev. B*, 36:7241–7243, Nov 1987.

[40] Gareth R. Eaton, Sandra S. Eaton, David P. Barr, and Ralph T. Weber. *Quantitative EPR*. Springer, Wien, New York, 2010.

[41] G. Blatter, M. V. Feigel'man, V. B. Geshkenbein, A. I. Larkin, and V. M. Vinokur. Vortices in high-temperature superconductors. *Rev. Mod. Phys.*, 66:1125–1388, Oct 1994.

[42] R. Zalecki, Marek Woch, M. Chrobak, and A. Kołodziejczyk. Penetration depth of magnetic field into yba 2 cu 3 o x film on polycrystalline ag substrate. *Acta Physica Polonica A*, 127:272–274, 02 2015.

[43] D. Agassi, D. K. Christen, and S. J. Pennycook. Thickness-dependent pinning in a superconductor thin film. *Journal of Applied Physics*, 101(2):023916, 01 2007.

[44] T. Shaposhnikova, Yu. Talanov, and Yu. Vashakidze. Origin of the irreversible microwave absorption versus the state of vortex matter in bi2sr2cacu2ox single crystals. *Physica C: Superconductivity*, 385(3):383–392, 2003.

[45] O. Görür, T. Küçükömeroğlu, C. Terzioğlu, A. Varilci, and M. Altunbaş. The effect of ag diffusion on properties of yba2cu3o7x thin films produced by electron beam deposition techniques. *Physica C: Superconductivity*, 418(1):35–42, 2005.

[46] A. V. Boris, N. N. Kovaleva, O. V. Dolgov, T. Holden, C. T. Lin, B. Keimer, and C. Bernhard. In-plane spectral weight shift of charge carriers in yba₂cu₃o_{6.9}. *Science*, 304(5671):708–710, 2004.

[47] See supplemental material at `http://link.aps.org/supplemental/10.1103/PhysRevB.110.125102`. *Physical Review B*, 110(12):125102, 2024.

[48] Angela Montanaro, Francesca Giusti, Matija Colja, Gabriele Brajnik, Alexandre M. A. Marciniak, Rudi Sergo, Dario De Angelis, Filippo Glerean, Giorgia Sparapassi, Giacomo Jarc, Sergio Carrato, Giuseppe Cautero, and Daniele Fausti. Visible pump–mid

infrared pump–broadband probe: Development and characterization of a three-pulse setup for single-shot ultrafast spectroscopy at 50 khz. *Review of Scientific Instruments*, 91(7):073106, 07 2020.

[49] John A. Weil, James R. Bolton, and John E. Wertz. *Electron Paramagnetic Resonance: Elementary Theory and Practical Applications*. Wiley, New York, 2 edition, 1994.

[50] Freeman J. Dyson. Electron spin resonance absorption in metals. ii. theory of electron diffusion and the skin effect. *Phys. Rev.*, 98:349–359, Apr 1955.

[51] D.V. Likhachev, N. Malkova, and L. Poslavsky. Modified tauc–lorentz dispersion model leading to a more accurate representation of absorption features below the bandgap. *Thin Solid Films*, 589:844–851, 2015.

Ringraziamenti

During this project, I had the great opportunity to interact with many people, from each of whom I learned a lot. Thanks to **Sandeep**, **Shyni**, **Luca**, and **Simone** for guiding me during the synthesis of the samples. My gratitude also goes to **Alexey** and **Dr. Kataev** for their supervision and guidance throughout my stay in Dresden.

None of this would have been possible without Daniele, so, switching to Italian...

Grazie **Daniele**, per avermi coinvolto in questo progetto, per la fiducia che hai riposto in me e per avermi accolto in questo meraviglioso gruppo. Grazie anche per le chiacchierate stimolanti, sulla fisica e non solo, che sono state per me fonte di ispirazione.

Grazie **Angela**, per avermi seguita con costanza (sì l'ho detto), per due tesi su due, spero tu non ti sia stufata di me. Grazie per tutti i consigli e per la pazienza che hai sempre avuto con me, il tuo esempio mi è di ispirazione. E grazie anche a **Giacomo**, **Enrico**, **Shahla**, **Nitesh**, **Antonio**, **Giovanni** e **Gabriele**, un gruppo migliore di così penso sia impossibile da trovare.

Grazie **Eleonora**, **Rachele**, **Beatrice** e **Andrea**, amici da una vita, sempre presenti, mai nello stesso posto sia mai. Con voi ho condiviso tanti momenti importanti, profondi, divertenti, l'affetto che provo per voi non ha bisogno di essere spiegato a parole.

Grazie **Chiara**, lo sai, non sono una campionessa nel dimostrare affetto, e anche adesso non so trovare le parole per dirti quanto ti voglio bene. Sei testimone di tutto quello che mi passa per la testa e mi accade, sei una presenza fondamentale nella mia vita, grazie.

Grazie **Christian**, per tutte le arrampicate, per avermi sempre spronata, per tutti i "credici" urlati da sotto parete (e anche in aula studio) e per tutti i "no take Tuesday" prontamente acclamati ma mai veramente applicati. Insieme a **Fabrizio**, grazie per avermi sempre sostenuta (facendomi notare che non capisco mai niente, in particolare le battute), grazie per avermi fatto scoprire canzoni che anche se non avessi mai scoperto sarei stata benissimo. Aggiungiamo a questo duo anche **Andrea**, grazie per tutte le serate D&D, se continuiamo con questo ritmo tra vent'anni forse avremo finito la campagna. Grazie (alla) **Andre**, grazie per le serate biscotti, per i weekend passati a ~~stud~~ chiacchierare, per le serate pizza e serie tv, grazie per essere sempre pronta a cantare una canzone Disney con me. Infine, per concludere con voi degli *appunti anonimi* (ps. non ho ancora capito perché il gruppo si chiama così), grazie **Filippo**, grazie per averci (quasi) sempre tirato pacco per le sessioni di arrampicata e per i commenti squisitamente pungenti che ci regali sempre. GRAZIE a tutti voi, avete reso speciali questi ultimi anni.

Grazie **Francesca** ed **Elisa**, siete due amiche dalla presenza sempre gentile. Grazie per gli esami preparati insieme e per i momenti più spensierati, dalle passeggiate alle congelate prese a Barcola.

Grazie a tutti i fedeli dell'aula *amici di Ciro*, sempre presenti per una pausa dallo studio e per una partita a tresette.

Grazie a **mamma** e **papà**, per avermi sempre sostenuto nel percorso universitario, anche adesso che mi porta più lontano da casa. Grazie per avermi sostenuto in tutte le mie passioni, dalla musica quando ero più piccola, a quelle più recenti, anche se non prevedono di rimanere sempre con i piedi ancorati a terra (lo so che avreste preferito che rimanessi sulla chitarra). Grazie a mia sorella e mio fratello, **Maria** e **Pietro**, in voi posso trovare un punto di riferimento per quando ho bisogno di aiuto, come anche un memento del "vivitela con più spensieratezza". Con voi condivido passioni differenti, ma l'affetto, grande, che provo per voi è uguale.

Questi ultimi due anni sono stati di gran lunga i più belli, non facili, non sempre sereni, a volte difficili, ma soddisfacenti della mia vita, sicuramente rimarranno impressi nei miei pensieri. Quindi grazie a tutte le persone che ne hanno fatto parte e che mi hanno accompagnata, spero di essere stata per tutti e tutte voi, anche solo in minima parte, quello che voi siete stati per me.

Con affetto,
Costanza